Karl-Franzens-Universität Graz
Institut für Physik

QCD-like theories on the lattice and their applications

Ouraman Hajizadeh

Dissertation zur Erlangung des
Doktorgrades der Naturwissenschaften

Betreut durch Prof. Dr. Axel Maas

Graz, October 2018

Abstract

The lattice study of QCD at finite density, is hampered by the infamous sign problem. The problem is even more severe in the thermodynamic regime, which is relevant for neutron stars as laboratories of the strong interactions. We circumvent this problem by studying QCD-like theories, which are accessible on the lattice at finite density. We address the questions of strong interactions at finite density in three different projects.

Using the baryon number density of quarks resulting from a lattice study of G_2-QCD at finite density, we calculate the mass-radius relation of a hypothetical neutron star, made from G_2-QCD neutrons. The results are exploratory, though insightful.

We investigate the behavior of the gauge sector of QC_2D on the lattice at finite density, where we observe an almost independent behavior with respect to the density in ghost and gluon correlation functions. This will bring remarkable simplifications to functional methods at finite density. This can lead to a first principle determination of the equation of state of neutron stars, if it could be carried over to real QCD.

We obtain the equation of state of $SU(2)$ Yang-Mills theory from the finite temperature gluon propagator. To do so we use a fit anstaz for the gluon propagator at finite temperature and fit the ansatz to the lattice data. A further development of this technique, could provide us with the equation of state of neutron stars in an effiecient way.

Kurzfassung

QCD-Gittersimulationen sind durch das Vorzeichenproblem stark eingeschränkt. Dieses Problem ist in den thermodynamischen Regionen, die für einen Neutronenstern als Versuchsobjekt der starken Wechselwirkung relevant sind, besonders ausgeprägt. Wir umgehen dieses Problem, indem wir QCD-ähnliche Theorien studieren, welche für Gittersimulationen zugänglich sind. Wir behandelnd Fragen zur starken Wechselwirkung in drei verschiedenen Projekten.

Wir berechnen die Massen-Radius Relation eines hypothetischen Neutronensterns aus G_2-QCD Neutronen unter Verwendung der Baryonzahldichte von Quarks aus einer Gittersimulation von G_2-QCD bei endlicher Dichte. Die Resultate sind explorativ, aber aufschlussreich.

Wir untersuchen das Verhalten des Eichsektors von QC_2D am Gitter bei endlichen Dichten, wobei wir ein Verhalten der Geist- und Gluonkorrelationsfunktionen erhalten, welches beinahe unabhängig von der Teilchendichte ist. Dieses Ergebnis führt zu starken Vereinfachungen von funktionalen Methoden bei endlichen Dichten, was eine fundamentale Berechnung der Zustandsgleichung eines Neutronensterns erlaubt, falls das Ergebnis auf echte QCD erweitert werden kann.

Wir erhalten die Zustandsgleichung einer $SU(2)$ Yang-Mills Theorie aus dem Gluonpropagator bei endlichen Temperaturen. Hierbei verwenden wir einen Ansatz für den Gluonpropagator und fitten diesen Ansatz an Gitterdaten. Eine Weiterentwicklung dieser Methode könnte uns eine effiziente Berechnung der Zustandsgleichung von Neutronensternen erlauben.

Contents

Chapter 1

Introduction

Neutron stars are the fate of most of heavy stars with masses above $8M_\odot$, through a supernovae explosion. Their equation of structure, mass-radius relation, denoted by $M(R)$ is determined by their equation of state as we will see in Chapter 6. They are composed of extremely dense nuclear matter, which is a result of gravitational contraction in the absence of thermal pressure. The determination of $M(R)$ can be insightful to the properties of the strongly interacting matter at high densities, thus neutron stars are known as the laboratory of the strong interaction and are important sources of information about large-scale effects of non-Abelian gauge theories especially at high densities. At high densities occurring inside neutron stars, the electron Fermi surface is so high that is easily perturbed and the inverse β decay, namely the capture of the electrons by the protons, is energetically favored. Thus the chemical composition of a neutron star is dominated by neutrons, hence the name. On the other hand, the quantum effects become more important at high densities, e.g. the overlap of the wave functions of the neutrons becomes stronger. If the neutron is a composite objects then its structure becomes important in this thermodynamic regime. The degrees of freedom that construct this structure are quarks and gluons and the quantum field theory governing the interactions between them is *quantum chromodynamics* QCD. In the following we provide evidences of the existence of this structure, relying mainly on arguments from [1, 2].

We review the arguments and experimental indications of the existence of quarks and the mediators of the strong interaction between them, the gluons. The argument is not necessarily concerned with the historical order of the discoveries.

The existence of quarks as the constituents of nucleons was indicated by the phenomenon of Bjorken scaling, which was the observation of the independence of the scattering amplitude from the energy transfered in inelastic scattering of leptons by nucleons. At high enough energies, the scattering reveals a similar structure to that of the elastic one from the scattering off three centers. However, this independence is not exact and signals only the existence of the three valence quarks, ignoring the dynamical ones. The electrical neutrality of the neutron in contrast to the proton suggests the existence of more than one type of quarks as the constituents of these nucleons. The idea of a quark carrying fractional electric charge and baryon number was first proposed by Gell-

Mann[1] and Zweig[2]. Inspired by this idea, by combining the requirement of getting the correct electrical charges for the nucleons and the minimal choice of two types of quarks up "u" and down "d" carrying the electric charges $Q_u = 2/3$ and $Q_d = -1/3$, respectively, we can construct the nucleons in the following way: The neutron is represented by "udd" and the proton by "uud" that gives the proton the electric charge $+1$ and for the neutron yields zero charge. The masses of the proton and the neutron are very close about 938.27 Mev and 939.57 Mev, respectively. This approximate equality suggests an approximate symmetry, the so-called *isospin* symmetry that states that the proton and the neutron are two states of a doublet, and QCD processes respect this symmetry approximately. In the language of quarks, an isospin transformation is equivalent to $u \leftrightarrow d$ in a similar way as the exchange of spin up $\uparrow$ and down $\downarrow$ in a $\mathbb{Z}_2$ spin model. The symmetry group of isospin is the global $SU(2)$ symmetry. The general form of this symmetry is called *flavor* symmetry tha includes more than two states, which are called flavors. For N_f flavors with equal mass we have an $SU(N_f)$ symmetry.

The fermionic nature of nucleons requires quarks to be fermions as well. The discovery of the $\Delta^{++}_{3/2}$ particle which is composed of three up quarks and thus symmetric in all its known quantum numbers, though being a fermion, leads to the proposal of a new fundamental degree of freedom to be called "color", by O.W. Greenberg, so that this new particle is anti-symmetric in color space and thus as a bound state of fermions anti-symmetric in the exchange of all the indices. The fact that all the observed baryons are color singlets, suggests $SU(3)$ as the smallest unitary group that can give a color singlet object composed out of three quarks, each lives in a fundamental representation of this group. The choice of 3 values for the color charge is also supported by the experimental measurement of the ratio $\sigma(e^+e^- \to hadrons)/\sigma(e^+e^- \to \mu^+\mu^-)$, where a factor 3 originated in this choice brings the theory in agreement with the experiment. Another experimental evidence is the decay rate for $\pi_0 \to \gamma\gamma$, the 3-valued color charge enters as the square of the number of colors and provides a factor of 9 in the calculation of the decay rate that validates the theory compared to the experiment. The momentum distribution of the proton in the Bjorken experiment, indicates the existence of another kind of *partons*[3], that do not contribute in the scattering process but carry some part of the momentum of the proton, they are thus charge neutral. However, there must be a mechanism of momentum transfer to these particles. Therefore we may consider another type of interaction, different from the well known electrodynamics that is mediated by these new partons. Their role is similar to the role of the photon in QED, and they are called gluon "g". Since they are electrically neutral, in the process of momentum transfer, the conservation of the electric charge demands an oppositely charged particle to be involved in the interaction. We thus, may expect that a quark and an antiquark are involved in a point-like interaction. The quark is transformed in the fundamental representation of $SU(3)$ and the antiquark in the anti-fundamental representation of $SU(3)$, thus gluon must transform in the non-trivial representation of $\bar{\mathbf{3}} \otimes \mathbf{3}$, which is 8 dimensional to make a color singlet quark-gluon vertex. This is also understood in analogy with QED, where the electric charge is the conserved quantity of the global $U(1)$ transformation and the electrodynamic interaction via photons guarantees the local $U(1)$ invariance. Accordingly, a local $SU(3)$ symmetry is preserved by the exchange of gluons.

The fact that the gluon carries color (formally means that QCD is a non-Abelian gauge theory)

---

[1] Originally to describe electromagnetic and weak currents in terms of the quark fields.

[2] Emphasizing on the constituent aspect of quarks.

[3] A term suggested by Feynman referring to the constituents of the nucleon.

leads to some of the characteristic features of QCD, like *asymptotic freedom, confinement, ...* [4]. Because they carry color charge they can interact with each other this leads to the anti-screening of the color charge, which results in a stronger effective charge at large distances. Here we present a heuristic argument to explain this behavior. We consider the tree-level momentum dependence of the gluon propagator which is the same as for photons and decays like $1/p^2$ with momentum p. The fermionic loops all contribute with a negative sign in both QED and QCD calculations, thus at high energies their contribution is suppressed and the effect of the interaction becomes stronger as we know from QED. A similar effect from quarks is derived in QCD calculations, but this can be suppressed by the positive contribution from gluon loops so that at high enough energies the theory becomes free. We can see this effect by analyzing the polarization of the vacuum in terms of the color charge. An electric charge polarizes the vacuum around itself so that the virtual particle with opposite charge are attracted to and the one with like charge are repelled from this charge. Thus the effect of the test charge is becoming weaker at larger distances, this is called screening effect. In QCD, however the gluonic loop does not screen the color charge, instead, they transfer it. Therefore at long distances the effect of vacumm polarization is more important and the color force becomes stronger, in closer distances, this leads to a comparatively weaker interaction. This phenomenon is known as asymptotic freedom, which was discovered by F. Wilczek and D. Gross for QCD [3]. It had already been discovered by I. B. Khriplovich [4] and G. 't Hooft [5] for pure Yang-Mills theories.

The phenomenon of confinement is another feature of low energy QCD. It is usually referred to the fact that only color singlet particles have been observed, i.e. although the particles in the spectrum of QCD carry different spins and electric charges, they are all color singlet. Another description of the problem is that, why we can not "ionize" a nucleon to get an isolated quark like we can ionize an atom. The following argument from [6] is an attempt to illustrate some aspects of this phenomenon.

The self interaction of the gluons, prevents them from spreading out in space so that they become confined in so-called flux tubes, whose energy increases with increasing of the distance r, so that its contribution in the energy is given by $V(r) \sim \sigma r$, where σ is a constant to be called *string tension*. The hadron spectrum also provides phenomenological evidences for the linear rising potential [7]. The plot of spin J as a function of the squared mass m^2 form nearly parallel lines known as "linear Regge trajectories". This observation can be explained by a model of a mesonic system that considers a meson as a one dimensional object of the size $2R$ with mass/energy density σ. Quark and anti-quark are sitting on its ends which rotate with the speed of light $c \equiv 1$ ($v(R) = R\omega = c$, ω is the angular velocity, $v(r)$ is the velocity at distance r from the center) thus the angular momentum is given by

$$\begin{aligned} J &= 2\int_0^R \frac{\sigma r v(r)}{\sqrt{1-v^2(r)}}dr \\ &= \frac{2}{R}\int_0^R \frac{\sigma r^2}{\sqrt{1-\frac{r^2}{R^2}}}dr \\ &= \frac{\pi}{2}\sigma R^2 \end{aligned} \tag{1.1}$$

---

[4] Although, not all the theories, showing these effects are non-Abelian.

It can be shown as well, that the mass of this mesonic system is given by

$$m = \pi \sigma R \tag{1.2}$$

Replacing R with $\frac{m}{\pi\sigma}$ in the last relation for J in (1.1) we obtain

$$J = \frac{m^2}{2\pi\sigma} \tag{1.3}$$

The last relation reproduce the observation of "Regge trajectories" and is another indication of the importance of the linear rising potential. For infinitely heavy quarks, the potential rises infinitely with the distance, thus the string never breaks to its constituents. For quarks with finite mass the potential does not increase infinitely; at a certain distance where the energy is high enough to afford the creation of a quark-antiquark pair, a new pair is produced that forms a bound state with the older ones so that no quark is set free from the pair but the potential stops increasing and is flattened out. This phenomena is known as string breaking. Therefore, the quarks and antiquarks stay confined, eventhough the "string" that keeps them together may break.

Dynamical chiral symmetry breaking is another important aspect of QCD vacuum, that has not yet been fully understood. We review this effect in the following: Mesons belong to the singlet representation of $\mathbf{3} \otimes \bar{\mathbf{3}}$ in color space and with two flavors to the product space $SU(2) \times SU(2)$, which is decomposed to a singlet and a triplet representations in flavor space. The sigma meson [5] belongs to the singlet and pions to the triplet representations. The mass of the sigma is close to 600 Mev, while the pions are much lighter with nearly equal masses around 134 Mev . The significantly lower mass of pions compared to the masses of the proton and the neutron as well as to the mass of the sigma, rises a question about the mechanism, through which quarks contribute to the mass of hadrons. The naive expectation would be $m_{u,d} \approx \frac{m_{n,p}}{3}$, thus a meson consisting of a quark $q = \begin{pmatrix} u \\ d \end{pmatrix}$ and antiquark $\bar{q} = \begin{pmatrix} \bar{u} \\ \bar{d} \end{pmatrix}$, should have a mass around $\frac{2m_{n,p}}{3}$, but this is not the case for pions. How can we describe this discrepancy? It seems that it is not only the number of quarks but also how they are bound together in the hadrons that play a role in this matter. The difference between the masses of the sigma and the pions is an indication of a symmetry breaking, that is illuminated in the following. Mesons live in $SU(2) \times SU(2) \equiv O(4)$ space. The QCD interactions at tree-level and the Dirac Lagrangian respects this symmetry. This means the equivalence of all the 4 dimensions for the theory at the level of the Lagrangian, while bound states break this symmetry to $SU(2) \equiv O(3)$. Which means, that one of the dimensions is different from the other three. This is an example of a dynamical symmetry breaking, and is signaled by the large mass of the sigma meson, compared to the masses of the pions. The precise form of this symmetry that is preserved by the QCD Lagrangian with two massless quarks, is $SU_V(2) \times SU_A(2)$, which is called *chiral symmetry*. The symmetry is broken by the so-called *chiral condensate* which is the expectation value of a Dirac bilinear operator, with quantum numbers of a meson. The symmetry broken space, corresponds to the manifold of the *Goldstone bosons*. They are massless modes orthogonal to the direction of the condensate in the space of broken symmetry. Thus the number of generators of this space, is equal to the number of Goldstone bosons of the theory. In the

---

[5] Its lifetime is too short. Which quasiclassically means, the quarks are not able to orbit each other once fully before it decays. Thus it may be considered as a resonance and not a bound state. Although with a strict definition of bound states, even pions and nucleons are only in pure QCD bound states and not in standard model.

present case, the space of broken symmetry is the $SU_A(2)$ space, with three generators and thus three Goldstone bosons. The vacuum vector along any direction of the initial symmetry, may not respect a subgroup of this symmetry group, in the sense that it changes by rotating in this subgroup, this is a description of the dynamical symmetry breaking, to any independent direction in this subgroup, a massless mode is associate to be called the Nambu-Goldestone boson, thus the number of the generators of the broken symmetry is the number of Goldstone modes. The chiral symmetry with nonzero current masses of the quarks is explicitly broken. In case this mass is small enough, the symmetry is approximately preserved at the level of the Lagrangian and the would-be Goldstone bosons will be massive although still much lighter than the other mass scales. Understanding this phenomenon in QCD from the first principle has been a challenge for long time and is related to the other non-perturbative phenomena, like confinement and formation of bound states.

The formation of bound states of quarks is expected to be a low energy phenomenon, since at large distances the color force, keeps the quarks bound together, forming e.g. mesons. This is then the region of energy that requires non-perturbative methods to be fully understood. Evidently it is the interaction that binds the quarks together, but how exactly these interactions generate the mass of the hadrons with the mentioned varieties, is a dynamical question and has been tackled by various non-perturbative methods like lattice gauge theory, functional methods including Dyson-Schwinger Equations (DSE) and Functional Renormalization Group (FRG), and model studies.

Many of the interesting phenomena involving strong interactions happen in the presence of matter, like the phase transitions in the early universe as well as inside the stars and more importantly inside neutron stars. There are also experiments going on at finite density and temperature at the LHC (Large Hadron collider). Dynamical chiral symmetry breaking and confinement are low energy effects of the QCD vacuum. We may ask if these phenomena are observed in the presence of matter. Intuitively we do not expect an abrupt change, slightly above zero temperature and density, as long as no other physical scale is reached. Thus it is reasonable to assume a confined and chiral symmetry broken phase at low temperatures and densities. This is confirmed by various studies. At higher temperatures the contribution of high energy modes become larger and thus we expect chiral symmetry restoration and *deconfinement*. The "deconfined" region refers to a regime, where the main degrees of freedom are quarks and gluons, at low densities it is also called *Quark-Gluon-Plasma*. It may be that some of the thermodynamic properties of this phase could be described by the fundamental degrees of freedom of QCD. However this does not mean that quarks and gluons as free particles are observed. This phase may be strongly interacting, despite the first expectations. The finite density regime is much richer and also computationally more demanding. A "deconfined" phase is also expected at high densities, where the overlap of the wave functions of the nucleons is significant and thus quarks may become main degrees of freedom. It may also lead to different pairing patterns of quarks and therefore phenomena like color superconductivity are predicted. Combining the results from first principle lattice calculations, model studies, perturbative calculations in asymptotic regimes and empirical nuclear physics leads to a conjectured phase diagram presented in Figure 1.1

The final goal is of course to explore the whole phase diagram, based on first principle calculations. It is becoming demanding, where non-perturbative effects are concerned. Lattice gauge theory is the most commonly employed non-perturbative method. However, the finite density regime, especially the regime where $\mu \gg T$ is not accessible to this method. Since lattice QCD

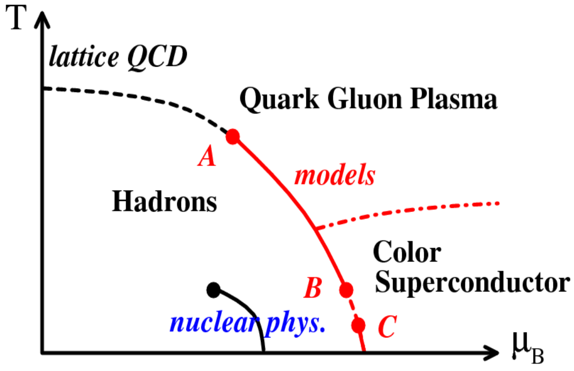

Figure 1.1: QCD phase diagram from [8].

at finite density suffers from the sign problem, namely its weight function is not guaranteed to be positive definite and thus it can not be used as a probability weight in lattice simulations. We explain this problem in more details in Chapter 3. However, there are other gauge theories which are similar to $SU(3)$ in various aspects, and yet are accessible on the lattice at finite density. In the next chapter we introduce the main properties of SU(2)-QCD and G_2-QCD. We show that even at finite density they have a real weight function and thus they are accessible to lattice studies. We also review their phase diagram to explore the similarities and the differences to the case of real (SU(3)) QCD. In addition, the realization of chiral symmetry and its breaking patterns for these groups are discussed. In Chapter 3, we review the lattice method for studying gauge theories and QCD.

As already mentioned, SU(2)-QCD also denoted by QC_2D, can be studied on the lattice even at finite density, it is the smallest non-Abelian gauge group with fermions thus its study at finite density can reveal general features of non-Abelian gauge theories and their correlation functions in this thermodynamic regime. Thus we will study ghost and gluon correlation functions of QC_2D at finite density in Chapter 4, this kind of studies can serve as a bench mark for other non-perturbative methods, as well.

Thermodynamic quantities of a system are given by the derivatives of the partition function. We can also show that a partition function can be written in terms of the n-point functions of the system. In chapter 5 we will use the data from the lattice study of $SU(2)$ Yang-Mills theory to examine the validity of a fit ansatz for the gluon propagator. The ansatz is based on an insight from a one-loop calculation of propagators at finite temperature in line with similar studies in condensed matter theory. We then will see how to use the result of the fit to calculate the pressure of the system. If this ansatz or a slightly modified version of it proves to be reliable, it will offer a much more efficient way to calculate the equation of state, for the whole thermodynamic regime.

Finally one of the main motivations to study QCD at finite density is to understand the structure of neutron stars. In the absence of lattice data for QCD at finite density, we will apply the results of lattice simulation of G_2-QCD in this thermodynamic regime to construct a hypothetical neutron star in Chapter 6, to be called G_2QCD-neutron star. In this study we will learn about large scale effects of non-Abelian gauge theories and also what is needed from a lattice study to produce a working equation of state for the G_2-QCD neutron star.

In Chapter 7, we summarize the three projects that are presented in this thesis and we suggest the possible ways to proceed.

Chapter 2

QCD-like theories

2.1 Motivation

As already mentioned in the introduction, $SU(3)$ is the gauge group governing strong interactions in nature. It is of great interest to understand the properties of these interactions in the medium to be able to explain interesting phenomena, especially in neutron stars, where the desnity is so high that quarks may become the relevant degrees of freedom and temperature is so low that the application of the non-perturbative methods seems to be even more necessary.

Unfortunately, at finite density, lattice QCD as one of the most reliable non-perturbative methods, suffers from the infamous sign problem. One way to circumvent this problem is to study QCD-like theories that are accessible on the lattice at finite density and share basic features with real QCD. Studying these theories at finite density on the lattice could serve as a bench mark for other non-perturbative methods. E.g. one may argue that the QCD phase diagram shows a specific behavior, based on the structure of the gauge group and functional method or model analysis. If similar arguments are applied to a QCD-like theory, predicting a particular behavior e.g. at finite density, then the confirmation of those predictions by lattice methods could hint on the viability of them for real QCD at finite density.

From a more general point of view, the study of QCD-like theories at finite density, brings us some new insight to the behavior of non-Abelian gauge theories at finite densities in general. For instance the lattice study of the so-called deconfinement transition for different QCD-like theories at finite density could reveal general features of this transition which are not restricted to the special case of QCD with three fundamental quarks. We can also learn about the generic properties of non-Abelian gauge theories by studying QCD-like theories in the vacuum or at finite temperature. Comparison of the results of quenched and unquenched regimes also tells us about the role of dynamical quarks in the phase diagram of each of these theories that may guide us toward the general features of non-Abelian gauge theories with different matter representations.

The choice of a QCD-like theory to be studied, depends on the required information and the efficiency of the simulations. As long as general properties of the Yang-Mills theories are concerned, $SU(2)$ is the most efficient choice, it is also accessible (with an even number of flavors) to

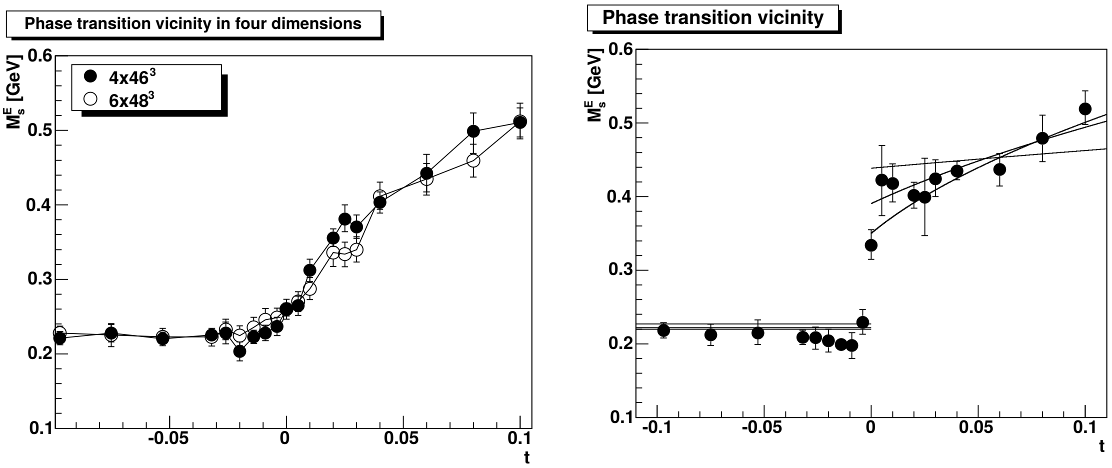

Figure 2.1: Electric screening mass for $SU(2)$ Yang-Mills (left panel) and $SU(3)$ Yang-Mills (right panel). Full and empty circles in the left panel, correspond to 4×46^3 and 6×48^3. The data in the right panel has been produced on 4×34^3 lattices. The vertical axis shows the screening mass, the horizontal one, shows the reduced temperature: $t = \frac{T}{T_c} - 1$. The plots have been taken from [9].

lattice simulations at finite density. Another gauge group relevant for the present study is G_2. It is a subgroup of $SO(7)$ and thus real in all of its representations. The crucial feature of G_2 for our purposes is the existence of a neutron-like state in its spectrum, which is composed of three fundamental quarks, in line with real QCD. This property is not present in $SU(2)$.

The main purpose of this chapter is to provide evidences that support the idea of the applicability of QCD-like theories. In the next section, we will present the results of the study of these theories in different thermodynamic regimes and point out the similarity and differences to the case of real QCD. The rest of the chapter will focus on those features that are inferred from the structure of these gauge groups and make it possible to study these theories at finite density on the lattice. The consequences of these properties with regard to chiral symmetry and its breaking patterns will be studied as well.

2.2 Phase transitions in QCD and QCD-like theories

Among the most essential and at the same time elusive features of QCD are confinement and chiral symmetry breaking at low energies. They become even more interesting when we notice that the temperature regions of the corresponding crossovers are very close to each other [10]. In contrast to QCD with adjoint quarks where the corresponding temperatures differ by a factor of almost eight [11]. The quenched approximation, in the chiral limit exhibits the coincidence of the chiral symmetry restoration and the deconfinement phase transition [12]. The same studies for $SU(2)$ also show similar behavior except for the order of the phase transition which can be related to the center symmetry[1]. The center of $SU(N)$ is the group $\mathbb{Z}_N$. The Polyakov loop is the order parameter of center symmetry for Yang-Mills theories. Its formal definition is given in the next chapter in Section 3.2.1. Here we just mention that its nonzero value signals the transition to the

---

[1] Center of a group is the set of all the elements of the group that commute with all the other elements.

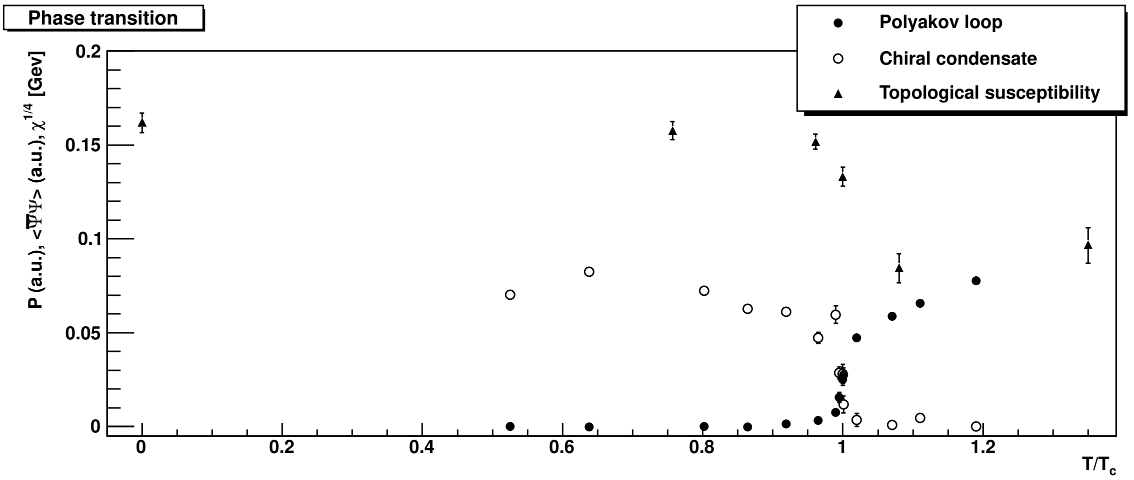

Figure 2.2: Chiral and deconfinement transition for G_2 Yang-Mills. The full circles show the polyakov loop, the empty circles show the chiral condensate and the triangles show the topological susceptibility, from [14, 15].

deconfined phase. The phase transition in the $\mathbb{Z}_2$ spin model is continuous and in the $\mathbb{Z}_3$ spin model is first order, we thus expect that the deconfinement transition in $SU(2)$ and $SU(3)$ are respectively second and first order. This is confirmed by the study of the screening mass of the gluon propagator for these theories at finite temperature [13, 9]. It is shown in Figure 2.1.

In contrast to the $SU(N)$ groups, G_2 does not have a non-trivial center, and the Polyakov loop $\langle L(T) \rangle$ has a nonzero value for all temperatures like full QCD. In this case the phase transition is signaled, where the slope of $\langle L(T) \rangle$ becomes infinite, which coincides with the temperature of the chiral symmetry restoration, shown in Figure 2.2. This observation encouraged further studies of G$_2$-QCD, in particular with applications to real QCD at finite density. However the possibility of a "deconfinement transition" in the absence of a non-trivial center, challenges the conventional understanding of deconfinement. Thus its study can also broaden our theoretical understanding of non-Abelian gauge theories and their phase transitions.

Also the main properties of the QCD phase diagram are seen in the G$_2$-QCD phase diagram, Figure 2.4. At low temperatures and densities we have the confined phase and at higher temperatures a deconfined region. For chemical potentials close to the mass of diquarks, the diquark condensate is predicted, although no signal of it has been seen on the lattice. Also the dominant degrees of freedom in the $\mu \approx m_n$ region, are neutrons. For higher densities the data is not sufficient for a reliable statement.

We now present some important results from the study of the phase diagram of QC$_2$D on the lattice in Figure 2.3. The important feature of the phase diagram is a hadronic confined phase at low temperatures and densities and quark-gluon-plasma at high temperatures and low densities. This is in line with ordinary QCD and thus supports the idea of the applicability of lattice studies of QC$_2$D to the case of real QCD, which is especially important at finite density. It also indicates a phase transition to the quarkyonic phase at medium densities and low temperatures which is in agreement with large N$_c$ arguments for $SU(N_c)$ gauge theories [18].

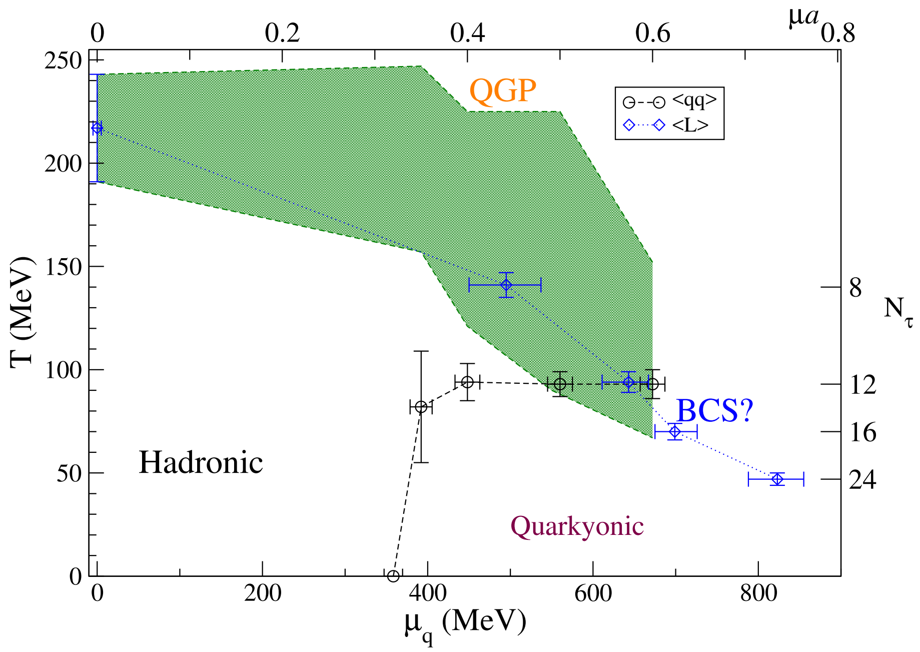

Figure 2.3: QC$_2$D phase diagram The black circles shows transition to the superfluid phase; the green band denotes the deconfinement crossover. The blue diamonds are the estimates for the deconfinement line from [16]

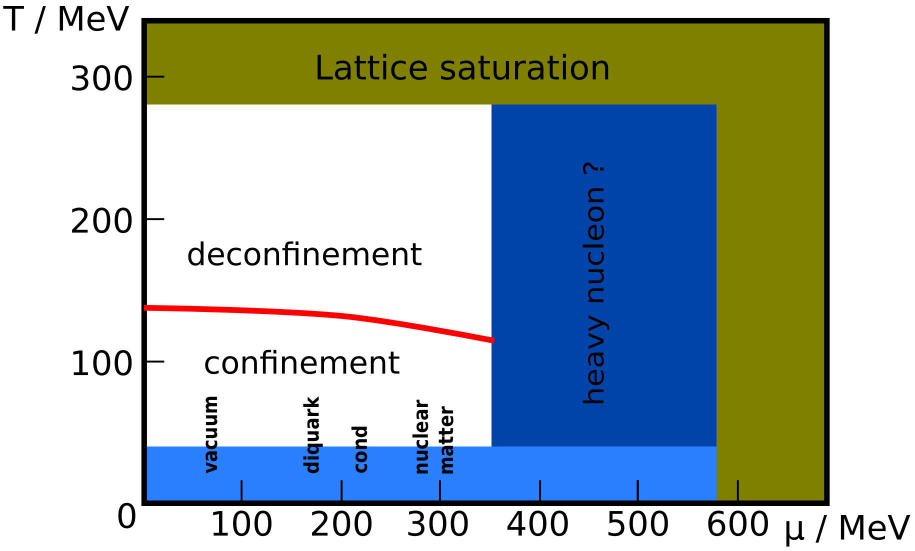

Figure 2.4: A sketch of the G$_2$-QCD phase diagram

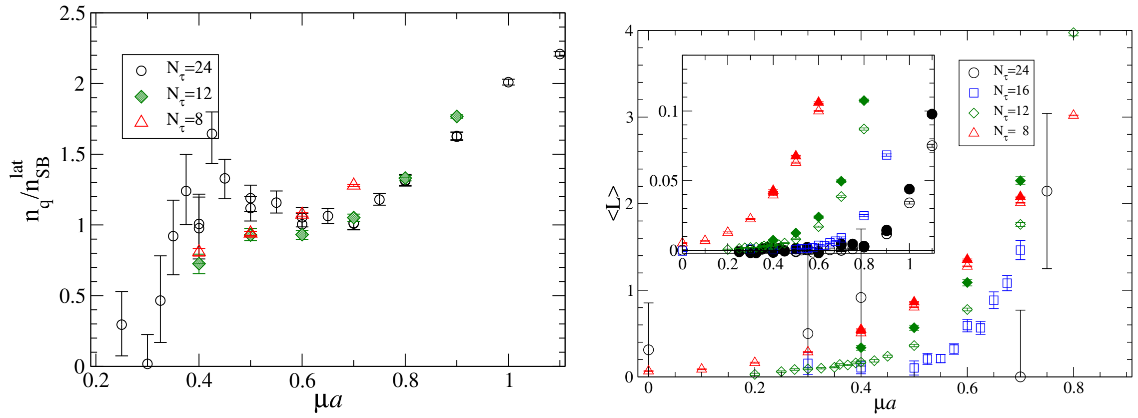

Figure 2.5: Quark number density vs chemical potential for QC$_2$D (left panel), the Polyakov loop vs chemical potential for various temperatures (right panel) from [17]

The result of the study of the Polyakov loop and the baryon number density scaled by the Stefan-Boltzman distribution is presented in Figure 2.5. The baryon density rises at the Silver-Blaze point above the quark mass and it behaves similar to the free Fermi gas for the intermediate chemical potentials. It increases again above the point of the ”deconfinement transition” as indicated by the plot of the Polyakov loop in the right panel. Thus the baryon density deviates from the one of weakly interacting matter, above the ”deconfinement” transition. This poses another challenge to the conventional understanding of the ”deconfined” phase as a weakly interacting regime in particular at finite density. With these examples we showed that QC$_2$D and G$_2$-QCD share essential features with QCD and also the differences of these theories can bring us more general insight to the behavior of non-Abelian gauge theories especially in the presence of matter.

After presenting some important results from the lattice study of G_2 and $SU(2)$ at finite density, it would be interesting to know what is the essential feature of these groups that makes these studies feasible. This is the subject of the next section.

2.3 The Dirac determinant

In this section we study the properties of the Dirac determinant under complex-conjugation, for the gauge groups G_2, $SU(2)$. As already mentioned, these properties are important regarding the applicability of lattice methods at finite density. They also determine the patterns of chiral symmetry breaking.

In this section, following [19], we first show the conditions that guarantee the reality and positivity of the Dirac determinant. Thereafter, we will see how the above mentioned Lie groups satisfy these conditions.

Suppose a unitary operator T exists, such that

$$[KT, D] = 0, \tag{2.1}$$

where K is the complex conjugation operator and D the Dirac operator, with λ and $|\psi\rangle$ as its eigenvalue and eigenvector given in the following relation

$$D|\psi\rangle = \lambda|\psi\rangle. \tag{2.2}$$

Combining equations (2.1) and (2.2), we obtain

$$D\,KT|\psi\rangle = KT\,D|\psi\rangle = KT\,\lambda|\psi\rangle = \lambda^*\,KT|\psi\rangle \tag{2.3}$$

Eigenvalues come in complex conjugate pairs, therefore we have

$$D|\psi\rangle = \lambda|\psi\rangle \text{ and } D|\tilde{\psi}\rangle = \lambda^*|\tilde{\psi}\rangle \quad |\tilde{\psi}\rangle = KT|\psi\rangle \tag{2.4}$$

Which states that if λ is an eigenvalue of D then λ^* is also an eigenvalue of D. Thus det(D) is real.

$$\det(D) = \prod_i \lambda_i = \prod_i \lambda_i^* = \det(D)^* \tag{2.5}$$

The above relation is only correct, if $|\psi\rangle$ and $|\tilde{\psi}\rangle$ are linearly independent. This requires T to satisfy an additional relation $(KT)^2 = -1$. In the follwing we will see how this condition excludes the possibility of linear dependence of $|\psi\rangle$ on $|\tilde{\psi}\rangle$.

Using unitarity of T we have,

$$\langle\psi|\tilde{\psi}\rangle = \langle\psi|KT\,\psi\rangle = \langle T\,\psi|TKT\,\psi\rangle. \tag{2.6}$$

Applying K to both sides of (2.6) ($\langle a|b\rangle = \langle K\,b|K\,a\rangle$) and using the condition $(KT)^2 = -1$ we obtain

$$\langle KTKT\,\psi|KT\psi\rangle = \langle (KT)^2\,\psi|KT\psi\rangle = -\langle\psi|KT\psi\rangle = -\langle\psi|\tilde{\psi}\rangle, \tag{2.7}$$

and thus

$$\langle\psi|\tilde{\psi}\rangle = -\langle\psi|\tilde{\psi}\rangle = 0. \tag{2.8}$$

The last equation states that ψ and $\tilde{\psi}$ are orthogonal and therefore the determinant is real and positive.

In the following, we will try to find the corresponding unitary transformations T for the two gauge groups of our interest. First we will see what is the consequence of equation (2.1) for an element of the gauge group. We will then see what should be the action of T on the Dirac matrices. We use the following form of the Dirac operator

$$D = (\partial_\mu + igt^a A^a_\mu)\gamma_\mu. \tag{2.9}$$

The form of the condition, given in equation (2.1) which is used in the following is

$$[KT, D] = 0 \to T^*D^* - DT^* = 0 \Rightarrow \quad TDT^{-1} = D^*. \tag{2.10}$$

Which requires the following relations for the pure kinetic term and for the gauge coupling term respectively

$$T\gamma_\mu T^\dagger = \gamma_\mu^*, \tag{2.11}$$
$$igTA_\mu^a t^a \gamma_\mu T^{-1} = -ig(t^a A^a)^* \gamma_\mu^*. \tag{2.12}$$

It is worth mentioning that the introduction of the chemical potential term $\mu\gamma_4$ does not affect the argument and condition (2.11) also takes care of this term. Inserting $T^{-1}T$ in the gauge part reduces it to

$$igTA_\mu^a t^a T^{-1} = -ig(A_\mu^a t^a)^*, \quad T\gamma_\mu T^\dagger = \gamma_\mu^*. \tag{2.13}$$

In the next step we try to find the operator T for the group G_2. The main property of G_2 that is used to show that its Dirac determinant is real, is the reality of all of its representations, which is defined as

$$TUT^{-1} = U^*, \tag{2.14}$$

where T is a similarity transformation. First we see, what is implied by (2.14) for the generators t^a of the algebra, which are given in terms of the group element by

$$U_\mu = exp(igA_\mu^a t^a). \tag{2.15}$$

The following relation gives the condition on the generators, as a result of the reality of a group element of G_2, where we drop the Lorentz index.

$$TUT^{-1} = U^* \to TA^a t^a T^{-1} = -(A^a t^a)^*. \tag{2.16}$$

We see that the condition in the first equation in (2.13) is satisfied by the reality of the gauge group in equation (2.16). Therefore, for G_2, the reality of the Dirac determinant is guaranteed by a unitary operator satisfying the equation (2.11) [2] and $(KT)^2 = -1$. In the following, we are going to show that $T = C\gamma_5$ satisfies both conditions in equations (2.11) and (2.17)

$$(KT)^2 = -1 \ \to T^*T = -1. \tag{2.17}$$

First we verify the relation in (2.11) for this proposal of T, while unitarity demands $T^\dagger = T^{-1}$. We replace T by $C\gamma_5$ in 2.11

$$T\gamma_\mu T^{-1} = C\gamma_5\gamma_\mu\gamma_5 C^{-1}. \tag{2.18}$$

Using the properties of the charge conjugation operator C and the gamma matrices, given in the following

$$C = C^{-1} = C^\dagger = -C^T, \ \ C\gamma_\mu C^{-1} = -\gamma_\mu^T, \tag{2.19}$$
$$\gamma_5 = \Pi_{i=1}^{i=4}\gamma_i, \ \ \{\gamma_5, \gamma_\mu\} = 0, \ \ \gamma_5^2 = 1, \tag{2.20}$$

then for $T = C\gamma_5$, we end up with

$$T\gamma_\mu T^{-1} = \gamma_\mu^T = \gamma_\mu^*, \tag{2.21}$$

---

[2] Since the argument leading to (2.11) and (2.12) is reversible

as required in (2.11). Condition (2.17) requires $C\gamma_5 C^* \gamma_5^* = -1$ which is verified using $\gamma_\mu^T = \gamma_\mu^*$

$$C\gamma_5 C^* \Pi_{\mu=1}^{\mu=4} \gamma_\mu^* = C\gamma_5 C^* \Pi_{\mu=1}^{\mu=4} \gamma_\mu^T. \tag{2.22}$$

From (2.19) we have

$$C^* = -C^{-1} \rightarrow CC^* = -1, \tag{2.23}$$

$$\gamma_\mu^T = C\gamma_\mu C^*. \tag{2.24}$$

Inserting (2.24) in (2.22) and using $\gamma_5^2 = 1$ and (2.23) we end up with

$$C\gamma_5 C^* \gamma_5^* = (-1)^3 C\gamma_5 C^* C\gamma_5 C^* = C\gamma_5^2 C^* = -1. \tag{2.25}$$

Thus we could show that there exists a unitary operator T that guarantees the reality and positivity of the Dirac determinant for the gauge group G_2 by satisfying (2.1) and $(KT)^2 = -1$

To find the corresponding operator T for $SU(2)$, satisfying the gauge part of (2.13), we use the Pauli algebra. From (2.13) we have

$$Tt^a T^\dagger = -(t^a)^*. \tag{2.26}$$

Comparing the Pauli-algebra given in (2.27) with equation (2.26),

$$\sigma_2 \sigma_i \sigma_2 = -\sigma_i^* \tag{2.27}$$

suggests the following form for T

$$T = \sigma_2 \tilde{T}. \tag{2.28}$$

Which implies, that T must contain a color factor σ_2 and $\tilde{T}$ carries the Dirac structure and is responsible for satisfying (2.11). As we already know it from the previous part, $\tilde{T} = C\gamma_5$ does the job. However, this choice will lead to

$$\tilde{T}\tilde{T}^* = -1 \rightarrow T^* T = 1 \tag{2.29}$$

The result of (2.29) tells us, that it is no longer guaranteed to have a positive determinant by this choice of T. It is worth mentioning that this last result is not compatible with $(KT)^2 = -1$ meaning for a real eigenvalue corresponding to $|\psi\rangle$ (the eigenvector of D) $KT|\psi\rangle$ may be dependent on $|\psi\rangle$ and therefore the positivity of the determinant can not be inferred.

The only question left to be answered is that if there exists any $\tilde{T}$ other than $\tilde{T} = C\gamma_5$, satisfying (2.11), while $\tilde{T}\tilde{T}^* \neq -1$. In the following we are going to exclude this possibility. Suppose the unitary operators U and $\tilde{U}$ both satisfy (2.11).

$$U\gamma_\mu U^\dagger = \gamma_\mu^T, \quad \tilde{U}\gamma_\mu \tilde{U}^\dagger = \gamma_\mu^T \tag{2.30}$$

$$U\gamma_\mu U^\dagger = \tilde{U}\gamma_\mu \tilde{U}^\dagger \tag{2.31}$$

Multiplying both sides of (2.31) by $\tilde{U}^\dagger$ from the left, and by U from the right, we get

$$\tilde{U}^\dagger U\gamma_\mu = \gamma_\mu \tilde{U}^\dagger U \to [\tilde{U}^\dagger U, \gamma_\mu] = 0. \tag{2.32}$$

According to Schur's lemma $\tilde{U}^\dagger U$ must be proportional to unity. Using this fact and unitarity of U and $\tilde{U}$ we have

$$\tilde{U}^\dagger U = c\mathbb{1} \to \tilde{U}^\dagger = cU^\dagger \tag{2.33}$$

$$\tilde{U}\tilde{U}^\dagger = c^* cUU^\dagger \to |c|^2 = 1 \tag{2.34}$$

from (2.33) and (2.34) we also have

$$\tilde{U} = c^* U \to \tilde{U}\tilde{U}^* = UU^* \tag{2.35}$$

Thus given that $U = C\gamma_5$ satisfies (2.13) any other operator $\tilde{U}$ satisfying that relation will give $\tilde{U}\tilde{U}^* = -1$. As a result for any operator U in (2.30) and T in (2.26) we have:

$$T = \sigma_2 U \to TT^* = 1 \tag{2.36}$$

Equation (2.36) tells us, that the Dirac determinant might be negative for $SU(2)$ in the fundamental representation. We will discuss the relevance of the Dirac determinant for the probability weight in lattice simulations in more detail in the next chapter.

2.4 Chiral symmetry

The non-degenerate masses of parity partners in the spectrum of QCD, namely the difference of 600 Mev between the masses of N and N^* is an indication of chiral symmetry breaking [6]. Since the chiral transformation of the constituent quark is translated to a parity transformation of baryons. On the other hand, the small mass of the pion can be explained by the chiral symmetry breaking mechanism, as well. Since chiral symmetry breaking is one of the main common features of QCD-like theories and QCD at low energies, in this section we study chiral symmetry for theories with different gauge groups and investigate their chiral symmetry breaking patterns.

Spontaneous chiral symmetry breaking is a dynamical effect and therefore could be only discussed when the action and the measure of the path integral are invariant under the chiral transformation, which is not the case in the presence of the axial anomaly[3] and the current quark mass. It is shown that the variation of the fermion integration measure under the chiral transformation, denoted by ΔD, is proportional to $tr[M]$ [6]. Where M denotes the flavor matrix of the transformation. If M is one of the generators of $SU(N_f)$ and $N_f > 1$ then its trace will vanish and thus the invariance of the measure is maintained. Therefore a non-trivial $SU(N_f)$ symmetry of the action is necessary to make the dynamical chiral symmetry breaking possible. In the following, we will see how the properties of the gauge groups G_2 and $SU(2)$ can lead to a non-trivial $SU(2)$ global symmetry with originally one flavor. In other word, we find the minimum number of flavors for each gauge group that makes the spontaneous chiral symmetry breaking possible.

---

[3] It refers to the non-invariance of the measure under the chiral transformation.

2.4.1 $SU(2)$

We follow the argument in [20] to study the chiral symmetry of the Dirac Lagrangian with $SU(2)$ guage group. First we rewrite the massless Dirac Lagrangian for the general gauge group in terms of ψ_R and ψ_L, that are given in (2.37)

$$\psi_R = \frac{1+\gamma_5}{2} \qquad \psi_L = \frac{1-\gamma_5}{2} \tag{2.37}$$

The Dirac Lagrangian reads

$$L = \overline{\psi}\gamma_\nu D_\nu \psi = i\psi_L^\dagger \sigma_\nu D_\nu \psi_L - i\psi_R^\dagger \sigma_\nu^\dagger D_\nu \psi_R, \tag{2.38}$$

where γ_ν are hermitian gamma matrices. D_ν denotes color covariant derivative and $\sigma_\nu \equiv (-i, \sigma_k)$. The above Lagrangian respects $U(N_f) \times U(N_f)$ symmetry where N_f stands for the number of flavors. The chiral symmetry breaking pattern of this case is presented in [6], we also mentioned it for QCD in the introduction. In the next section we study this pattern for $SU(2)$ and G_2. Here we want to see how the apparent $U(N_f) \times U(N_f)$ symmetry will be enlarged to a higher dimensional chiral symmetry so that the trivial flavor structure could still allow for a dynamical chiral symmetry breaking. To do so we define a new field $\tilde{\psi}_R = \sigma_2 \tau_2 \psi_R^*$ that transforms like ψ_L. Rewriting the Lagrangian (2.38) in terms of the new field and using the pseudo-reality of two-color QCD, we have:

$$L = i\psi_L^\dagger \sigma_\nu D_\nu \psi_L + i\tilde{\psi}_R^\dagger \sigma_\nu D_\nu \tilde{\psi}_R = i\Psi^\dagger \sigma_\nu D_\nu \Psi \tag{2.39}$$

$$\Psi = \begin{pmatrix} \psi_L \\ \tilde{\psi}_R \end{pmatrix} \tag{2.40}$$

To derive the relation (2.39) we use the psudo-reality property of the Pauli matrices in the following forms $-\sigma_2 \sigma_\nu^\dagger \sigma_2 = \sigma_\nu^T$ and $\tau_2 \tau_k \tau_2 = -\tau_k^T$, which are equivalent since Pauli matrices are Hermitian. (τ_k) represents the generators of the color group. The important property of equation (2.39) is that it is invariant under $\psi_L \leftrightarrow \tilde{\psi}_R$ so there is an additional $U(2)$ symmetry and these two components act as two different flavors. Therefore the Lagrangian has the enlarged symmetry of $U(2N_f)$. Because of the axial anomaly for the quantized massless theory this symmetry will break to $SU(2N_f)$ (up to discrete symmetries). This shows, that for two-color QCD even with one flavor there is a $SU(2)$ symmetry and therefore the measure will be invariant under its transformations, making spontaneous chiral symmetry breaking possible.

2.4.2 G_2

The reality of G_2 also leads to an enlarged flavor representation that we are going to discuss in this section. Here we follow the argument from [21]. First we show that the Dirac Lagrangian with the gauge group G_2 is up to a total derivative, charge conjugation invariant. Namely:

$$L[\psi^c, A, m] = L[\psi, A, m], \tag{2.41}$$

where $A = A^a t^a$ and t^a represents elements of the corresponding Lie algebra g_2, $a = 1, .., 14$. To do so, first we see how the left side of (2.41) transforms under charge conjugation with the following definitions of the charge conjugation transformation of a Dirac spinor: $\psi^c = C\overline{\psi}^T$ and $\overline{\psi^c} = -\psi^T C^{-1}$. Writing down explicitly the left side of (2.41), we have:

$$L[\psi^c, A] = \overline{\psi^c} i\gamma_\mu(\partial_\mu - gA^a t^a)\psi^c \tag{2.42}$$

$$L[\psi^c, A] = -i\psi^T C^{-1}\gamma_\mu \partial_\mu C\overline{\psi}^T + ig\psi^T C^{-1}\gamma_\mu t^a A^a_\mu C\overline{\psi}^T, \tag{2.43}$$

where C represents the charge conjugation operator, introduced in Section 2.3 with the properties $C\gamma_\mu C^{-1} = -\gamma_\mu^T$ and $C = C^{-1}$. Using these properties, we can write the kinetic term L_k as:

$$L_k[\psi^c] = i\partial_\mu(\psi^T \gamma_\mu^T \overline{\psi}^T) - i(\partial_\mu \psi^T)\gamma_\mu^T \overline{\psi}^T \tag{2.44}$$

$$L_k[\psi^c] = B + i\overline{\psi}\gamma_\mu \partial_\mu \psi \tag{2.45}$$

The first term in equation (2.44) is a total derivative, thus it does not contribute to the action. Given $L_k = L_k^T$ (as for any scalar quantity), introducing a minus sign due to the exchange of the fermionic fields and dropping the total derivative term B, we have

$$L_k[\psi^c] = L_k[\psi]. \tag{2.46}$$

It remains to show the corresponding equality for the gauge part of the Lagrangian in (2.43) denoted by $L_g[\psi^c]$, which is given by (2.47), following similar arguments, applied to the kinetic part

$$L_g[\psi^c] = ig\overline{\psi}\gamma_\mu A^a (t^a)^T \psi. \tag{2.47}$$

In order to have $L_g[\psi^c] = L_g[\psi]$ the generators of the group t^a must satisfy the relation $-t^a = (t^a)^T$, which holds for the generators of g_2, because of the reality of all the representations of the group. So far we showed the symmetry under $\psi \leftrightarrow \psi^c$ (2.41), we use this symmetry to formulate the Lagrangian with the enlarged flavor representation of the spinors. First we rewrite $L[\psi, A]$ in the following way:

$$L[\psi, A] = (\frac{\overline{\psi} + \overline{\psi^c}}{2})D(\frac{\psi + \psi^c}{2}) + (\frac{\overline{\psi} - \overline{\psi^c}}{2})D(\frac{\psi - \psi^c}{2}) \tag{2.48}$$

$$D = i\gamma_\mu(\partial_\mu - gA^a t^a). \tag{2.49}$$

We then define χ and η as follows:

$$\chi \equiv \frac{\psi + \psi^c}{2}, \quad \eta \equiv \frac{\psi - \psi^c}{2i} \tag{2.50}$$

thus $\chi^c = \chi, \quad \eta^c = \eta$. Therefor equation (2.48) can be written as

$$\overline{\psi}D\psi = \overline{\chi}D\chi + \overline{\eta}D\eta. \tag{2.51}$$

The last formulation tells us that for each N_f dimensional Dirac spinor, there exists a $2N_f$ dimensional Majorana spinor $\lambda = \lambda^c, \lambda = (\chi_1, .., \chi_{N_f}, \eta_1, .., \eta_{N_f})$. Thus even with one flavor for the group G_2, there is a non-trivial $SU(2)$ symmetry that allows dynamical chiral symmetry breaking.

2.5 Chiral symmetry breaking patterns and Goldstones

Here we want to find out the patterns of chiral symmetry breaking for G_2 and $SU(2)$ gauge groups, following arguments from [22, 20]. More specifically we want to specify the remnant of the symmetry which is still preserved by the chiral condensate. We will show in the following that the chiral condensate of the theory with the gauge groups G_2 and $SU(2)$ respectively respect $O(2N_f)$ and $SP(2N_f)$ symmetry. We define these transformation in the following.

A $2N$-vector ϕ belonging to the fundamental representation of $SU(2N)$ can be written, as $\phi = (\phi_1, \phi_2)$, using two N-vectors ϕ_1 and ϕ_2. The set of transformations that preserve the following quadratic form of two vectors ϕ and χ, invariant, is the subgroup $O(2N)$ of $SU(2N)$.

$$\phi_1\chi_1 + \chi_2\phi_2. \tag{2.52}$$

The subgroup $SP(2N)$ is the set of transformations that keeps the following form invariant

$$\phi_1\chi_2 - \chi_1\phi_2. \tag{2.53}$$

The quadratic forms in (2.52) and (2.53) suggest a symmetric and an antisymmetric metric for the scalar product in $O(2N)$ and $SP(2N)$ spaces.

A general form of a bilinear of quark and anti-quark, is presented by

$$\epsilon_{\alpha\beta}\psi^{\alpha}_{ia}\psi^{\beta}_{jb}I^{ij,\,ab} \tag{2.54}$$

Where α and β are Dirac indices and $\epsilon^{\alpha\beta}$ takes care of antisymetrization in Dirac space. The pairs of color and flavor indices are respectively denoted by i,j and a, b. As we discussed previously the flavor symmetry of G_2 and $SU(2)$ gauge theories is extended to $SU(2N_f)$, thus their quarks are essentially $2N_f$-vecotrs.

The reality of the fundamental representation of G_2 and thus the equivalence of quarks and anti-quarks, then requires the color structure to be symmetric. The full antisymmetry of the fermionic quadratic form then demands $I^{ij,\,ab}$ to be symmetric also in flavor space , preserving (2.52) invariant. Therefore the symmetry that is still preserved by the chiral condensate is $O(2N_f)$.

Quarks in 2-color QCD (QC$_2$D), live in a psudo-real representation that is equivalent to having an anti-symmetric color structure , which requires an antisymmetric "metric", with respect to the exchange of N_f-vectors. Therefore $SP(2N_f)$ is the preserved symmetry by the chiral condensate in this case.

The Goldstone manifold is thus given by the group $SU(2N_f)/O(2N_f)$, with $2N_f^2 + N_f - 1$ number of Goldstone modes for dynamical symmetry breaking in G$_2$-QCD. The corresponding manifold for QC$_2$D is $SU(2N_f)/SP(2N_f)$ and thus $2N_f^2 - N_f - 1$ Goldstone bosons are present in the spectrum of the massless theory.

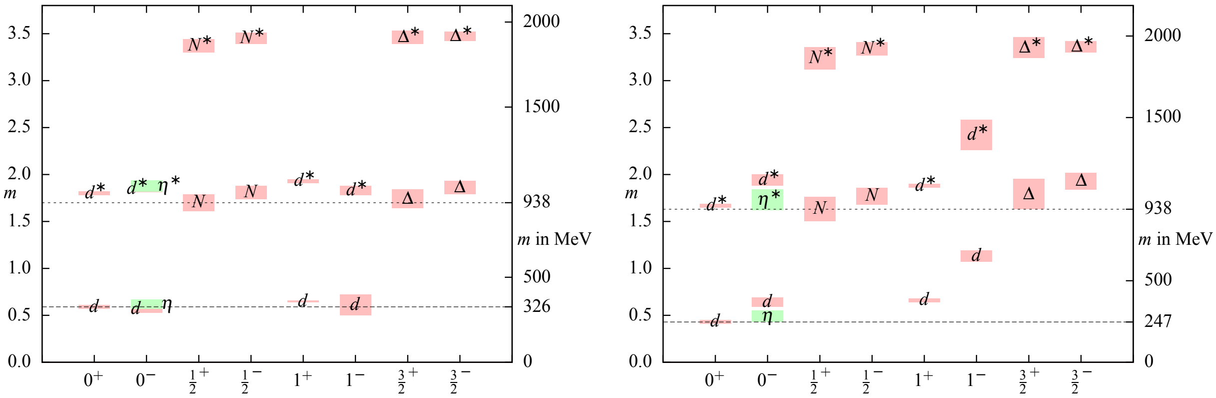

Figure 2.6: Mass spectrum of the light, $m_d(0^+) = 247$ Mev, (right) and heavy, $m_d(0^+) = 326$ Mev (left), ensembles for G$_2$-QCD from [21].

2.6 G_2 group properties

In this section, we review some of the properties of G$_2$-QCD that can be inferred from the structure of the group and is relevant for our study. We will refer to these properties later on, when we discuss the composition of a G$_2$-QCD neutron star and its stability condition in Chapter 6. As we mentioned G_2 is a subgroup of $SO(7)$[23, 21] and it has a 7 dimensional fundamental representation. Its generators obey 7 independent constraints thus the number of generators is reduced from 21 to 14. Therefore G_2 has 7 quarks and 14 gluons. The color singlet state that are expected to be observed in the spectrum are given in the following

$$\mathbf{7} \otimes \mathbf{7} = \mathbf{1} \oplus \mathbf{7} \oplus \mathbf{14} \oplus \ldots \tag{2.55}$$

$$\mathbf{7} \otimes \mathbf{7} \otimes \mathbf{7} = \mathbf{1} \oplus 4.\mathbf{7} \oplus 2.\mathbf{14} \oplus \ldots \tag{2.56}$$

$$\mathbf{14} \otimes \mathbf{14} \otimes \mathbf{14} = \mathbf{1} \oplus \mathbf{7} \oplus \ldots \tag{2.57}$$

$$\mathbf{14} \otimes \mathbf{14} = \mathbf{1} \oplus \mathbf{14} \oplus \ldots \tag{2.58}$$

$$\mathbf{7} \otimes \mathbf{14} \otimes \mathbf{14} \otimes \mathbf{14} = \mathbf{1} \oplus \ldots \tag{2.59}$$

The relation (2.56), implies the possibility of a neutron-like bound state in G$_2$-QCD. The color-singlet diquarks and gluballs are the consequences of relations (2.55) and (2.57). The screening of a quark by three gluons forming a hybrid bound-state, read from (2.57), is in line with string breaking of G_2 Yang-Mills, which implies that finite energy is needed to have a free valence quark.

Figure 2.6, shows that both diquarks and neutrons are present in the spectrum of G$_2$-QCD. Since the current mass of quarks is non-zero, the explicit breaking of the chiral symmetry manifest itself in the spectrum of the light ensemble. We also observe the massive neutron compared to the goldstones which is similar to the spectrum of real QCD. The calculation of the mass of the hybrid (qggg), is at the moment very demanding, thus we do not see it in the present spectrum.

Chapter 3

Lattice QCD

Lattice QCD or more generally lattice field theory is the formulation of a quantum field theory on a discrete space-time. It is generally formulated on Euclidean space-time, thus allows us to exploit the analogies to statistical physics. We may interpret the weight factor of the partition function path integral as a probability measure and thus use statistical methods to evaluate the observables. It is a first principle method, since it relies on the fundamental theory without uncontrolled modifications. It is non-perturbative, since it does not rely on coupling expansions. Therefore it is an important tool to study non-perturbative aspects of QCD, like confinement and chiral symmetry breaking. As mentioned in the introduction, non-perturbative methods in the continuum usually depend on the heavy use of modeling or uncontrolled truncations and approximations. Studying a quantum field theory on the lattice can provide the continuum methods with benchmarks to check the viability of these truncations and approximation. The discretization of space-time and the finite volume of the lattice remedy respectively the ultraviolet and infrared divergencies, present in the continuum formulation of some of the field theories. It of course, introduces artifacts to the results, although they can be controlled by decreasing the distance between two sites of lattice, the *lattice spacing*, and by examining the theory on the larger lattices.

In this chapter we will introduce the main aspects of lattice QCD methods, focusing on its relevance for gauge sector studies. We mainly follow [6].

3.1 QCD action on the lattice

In this section we review the formulation of the QCD action on the lattice. We formulate it in a general way, which is applicable to gauge theories with fermions with arbitrary non-Abelian gauge groups. We start from a discretized version of the free Dirac action in 4 dimensions, which reads

$$S_F^0[\psi,\overline{\psi}] = a^4 \sum_{n\in\Lambda} \overline{\psi}(n) \left(\sum_{\mu=1}^{4} \gamma_\mu \frac{\psi(n+\hat{\mu}) - \psi(n-\hat{\mu})}{2a} + m\psi(n) \right), \tag{3.1}$$

where $\psi(n)$ represents the fermion field on the site n of the $4D$ lattice Λ which is given by

$$\Lambda = \{n = (n_1, n_2, n_3, n_4)|0 \leq n_i \leq N_i - 1\} \,, \tag{3.2}$$

where $n_i \in \mathbb{N}$, N_i gives the size of the i-th dimension of the lattice and a is the lattice spacing. The above form of the fermionic action is not invariant under gauge transformations. In the following, we calculate the change in S_F^0 under gauge transformations and modify the action in such a way, that the change under gauge transformations cancels the one from the $S_F^0[\psi, \overline{\psi}]$, maintaining the gauge invariance of the new action. The fermion fields are transformed as follows

$$\psi(n) \to \psi(n) = \Omega(n)\psi(n), \;\; \overline{\psi}(n) \to \overline{\psi}'(n) = \overline{\psi}(n)\Omega^\dagger(n) \,, \tag{3.3}$$

where $\Omega(n)$ is an element of the gauge group of the transformation on each lattice site n. Obviously the mass term is invariant. The kinetic term, that couples fermions sitting on the two different lattice sites is the non-invariant part, shown in the following

$$\overline{\psi}(n)\psi(n+\hat{\mu}) \to \overline{\psi}'(n)\psi'(n+\hat{\mu}) = \overline{\psi}(n)\Omega^\dagger(n)\Omega(n+\hat{\mu})\psi(n+\hat{\mu}) \,. \tag{3.4}$$

The fermions are transformed differently on different sites, since the transformation group element is in general different on each lattice site. It is natural to introduce a variable $U_\mu(n)$, to be called link variable, that connects two neighboring sites, which yields a gauge invariant object $\overline{\psi}(n)U_\mu(n)\psi(n+\hat{\mu})$. The transformation rule of the link variable is defined as follows

$$U'_\mu(n) = \Omega(n)U_\mu(n)\Omega(n+\hat{\mu})^\dagger. \tag{3.5}$$

Thus $U_\mu(n)$ is also an element of the gauge group. Combining this with equation (3.3) the invariance of $\overline{\psi}(n)U_\mu(n)\psi(n+\hat{\mu})$ is guaranteed. Equivalently the invariance of the backward term in the kinetic part is maintained by the group element $U_{-\mu}(n)$, defined as

$$U_{-\mu}(n) \equiv U_\mu(n-\hat{\mu})^\dagger \,. \tag{3.6}$$

Finally the gauged fermion action on the lattice reads,

$$S_F[\psi, \overline{\psi}, U] = a^4 \sum_{n\in\Lambda} \overline{\psi}(n) \left(\sum_{\mu=1}^{4} \gamma_\mu \frac{U_\mu(n)\psi(n+\hat{\mu}) - U_{-\mu}(n)\psi(n-\hat{\mu})}{2a} + m\psi(n) \right) \tag{3.7}$$

After introducing the link variable, $U_\mu(n)$, and its transformation properties, we construct gauge invariant objects, purely made out of link variables. This will be used to formulate the action of a pure gauge theory on the lattice as well as important observables like the Polyakov loop which serves as the order parameter of the deconfinement transition in Yang-Mills theories. It can easily be seen that the multiplication of a line of consecutive links from site n to site m, denoted by $W(n,m)$ transforms like a quark-antiquark pair $\psi(n)\overline{\psi}(m)$. This similarity will be used later. The fact that the transformation depends only on the starting and the ending points of the path makes it clear that a closed loop $W(n_0)$ transforms like

$$W'(n_0) = \Omega(n_0)W(n_0)\Omega(n_0)^\dagger \tag{3.8}$$

$$\implies \mathrm{tr}[W'(n_0)] = \mathrm{tr}[W(n_0)] \tag{3.9}$$

where we used the cyclicity property of the trace to show the gauge invariance of $\mathrm{tr}[W(n_0)]$.

We can now formulate the pure gauge action on the lattice, based on two constructive and two viability considerations. First, it must be gauge invariant and second, it must take into the account all of the links of the lattice. The minimal choice that satisfies the gauge invariance is the trace of the shortest non-trivial closed loops to be called *plaquette* $U_{\mu\nu}$,

$$\begin{aligned} U_{\mu\nu}(n) &= U_\mu(n)U_\nu(n+\hat{\mu})U_{-\mu}(n+\hat{\mu}+\hat{\nu})U_{-\nu}(n+\hat{\nu}) && (3.10)\\ &= U_\mu(n)U_\nu(n+\hat{\mu})U_\mu(n+\hat{\nu})^\dagger U_\nu(n)^\dagger, && (3.11)\end{aligned}$$

in the last line we used (3.6). The summation over all these plaquettes includes all of the links of the lattice. The third consideration is that the action, S, must be real so that e^{-S} acts as the probability and finally it must produce the correct continuum limit. Putting all these together, we arrive at the Wilson formulation of the gauge action

$$S_G[U] = \frac{2}{g^2}\sum_{n\in\Lambda}\sum_{\mu<\nu}\mathrm{Re}\,\mathrm{tr}[\mathbb{1} - U_{\mu\nu}]. \tag{3.12}$$

The prefactor and the unity operator from which the plaquette is subtracted, ensure the correct continuum limit. Finally, the QCD action reads

$$S_{QCD} = S_F[\psi,\overline{\psi},U] + S_G[U]. \tag{3.13}$$

Later we will see that the fermionic part of the action, $S_F[\psi,\overline{\psi},U]$, suffers from a lattice artifact and we will see how to improve it. In the next section we discuss, other gauge invariant objects, made out of link variables and their applications.

3.2 Wilson loop and quark static potential

In this section, we construct a certain class of gauge invariants, that can be used in defining the quark-anti quark static potential and thereafter in the definition of phenomena like confinement. The trace of a loop of link variables is a natural starting point. The Wilson loop, W_L, is a quantity of this type. It contains two spatial lines of links $S(\mathbf{m},\mathbf{n},n_t)$ and $S(\mathbf{n},\mathbf{m},0)$ and two temporal lines $T(\mathbf{m},0,n_t)$ and $T(\mathbf{n},n_t,0)$ so that the lines of each pair are oppositely oriented. The spatial ones connect the point $\mathbf{m}$ to $\mathbf{n}$ on the hyper-planes of $t = n_t$ and $t = 0$ and the temporal lines connect the points $t = n_t$ and $t = 0$, keeping the spatial coordinate once fixed at $\mathbf{m}$ and once at $\mathbf{n}$. The physical interpretation of the Wilson loop, becomes clear after a simple gauge transformation that sets all the temporal lines equal to $\mathbb{1}$, so that we have

$$\langle W_L\rangle = \left\langle \mathrm{tr}\left[S(\mathbf{m},\mathbf{n},n_t)S(\mathbf{m},\mathbf{n},0)^\dagger\right]\right\rangle. \tag{3.14}$$

$S(\mathbf{m},\mathbf{n},n_t)$, the so-called Wilson line, transforms like a quark anti-quark pair $\psi(m)\overline{\psi}(n)$. We expect the lowest lying modes to survive at larger times, thus for $t\to\infty$ we have

$$\langle W_L\rangle \sim e^{-tV(r)},\ \ r = |\mathbf{m}-\mathbf{n}|,\ \ t = n_t a, \tag{3.15}$$

and only the static pair survives , with $V(r)$ as their (potential) energy. The strong coupling expansion of the Wilson loop together with the first relation in (3.15) leads to a linearly rising static quark potential. For the weak coupling regime, and for short distances we have $V(r) \sim \frac{1}{r}$. We use the continum formulation of quenched QCD to argue for the validity of the following equation

$$V(r) = A + \frac{B}{r} + \sigma r, \tag{3.16}$$

for the static quark potential, where σ is the string tension that was introduced in Chapter 1.

The continuum Yang-Mills action reads

$$S_G[A] = \frac{1}{4}\int d^4x F^a_{\mu\nu}(x) F^a_{\mu\nu}(x), \tag{3.17}$$

where the sum over the color index a in the adjoint representation, as well as over the Lorentz indices is assumed. $F^a_{\mu\nu}(x)$ denotes the field strength tensor

$$F^a_{\mu\nu}(x) = \partial_\mu A^a_\nu(x) - \partial_\nu A^a_\mu(x) - g f_{abc} A^b_\mu(x) A^c_\nu(x), \tag{3.18}$$

where g is the coupling and f_{abc} represents the structure constants of the Lie algebra. In the limit of small coupling $g \ll 1$, one can see that the self-interaction terms in the field strength tensor is suppressed and the gauge action will be dominated by the abelian parts. Thus the Coulomb-type behavior $1/r$ is expected to be dominant in this regime. Equipped with the results of perturbation theory, $\frac{dg(r)}{dr} > 0$, we may consider the weak coupling regime corresponding to the behavior of the potential at short range. Thus for short distances gluon fields look like the electric fields outgoing from the positive charge and ingoing to the negative charge. At larger distances the non-Abelian feature of the theory, leading to the self-interaction of gluons plays a more important role and we end up with the linear rising potential as the dominant term.

3.2.1 Polyakov loop and the deconfinement transition

As we saw previously, we can calculate the static quark potential from the Wilson loop in the limit of $t \to \infty$. In this section we introduce a modified version of the Wilson loop, the so-called Polyakov loop, that plays the corresponding role at finite temperature. This loop is essentially a Wilson line at fixed spatial coordinate and is wrapped around the time dimension. In a similar way as one can show that a line of link variables $L(m, n)$, connecting the lattice sites m and n transforms like a pair of quark-antiquark, we can see that $L(m, n)\psi(n)$ transforms like $\psi(m)$. This may allow us to interpret $L(m_0, n_0)$ with constant spatial coordinate as an Euclidean time evolution operator. Thus it can be written as

$$L(m_0, n_0) = e^{-a(m_0 - n_0)H}. \tag{3.19}$$

For $m_0 = 0$ and $n_0 = aN_t$ we have a closed loop which is called Polyakov loop, denoted by $L(T)$, where $T = \frac{1}{aN_t}$ is the temperature. Therefore its expectation value $\langle L(T) \rangle$ gives the free energy of the static quark F_q.

$$\langle L(T)\rangle = e^{-a(N_t)F_q} \tag{3.20}$$

If $\langle L(T)\rangle = 0$ it is equivalent to $F_q \to \infty$ thus we need infinite energy to have a free static quark this is compatible with our understanding of the confined phase. The free energy of a static quark is finite for $\langle L(T)\rangle \neq 0$, which is interpreted as the deconfined phase. However, these sharp definitions are limited to the quenched regime, in reality the definition of these phenomena are less clear. E.g. no colored particle ever has been detected thus deconfinement can not be interpreted as the color deconfinement. Isolated quarks and gluons also have not been detected, even in the deconfined phase. Full QCD contains dynamical quarks, thus $\langle L(T)\rangle$ is always non-zero, although a sharp rise at high temperatures occurs. Therefore we should use this terminology cautiously.

3.3 Fermions on the lattice

One of the main purposes of this thesis is to study the effect of dynamical quarks in different thermodynamic regimes on the lattice "observables", which is studied e.g. in Chapter 4 . We will also apply the results of previous studies of this type to learn about neutron stars in Chapter 6. Thus it is important to know how to formalize the fermion action on the lattice. In Section 3.1, we presented a naive form of the fermion action on the lattice, that is preserved under gauge transformations.

3.3.1 Wilson-Dirac action

In this section, first we see how this naive discretization of the fermion action leads to a certain unphysical effect, to be called fermion doubling problem and then we apply the Wilson formulation to avoid this effect. The naive fermion action reads

$$S_F[\psi,\overline{\psi},U] = a^4 \sum_{n\in\Lambda} \overline{\psi}(n)\Big(\sum_{\mu=1}^{4}\gamma_\mu \frac{U_\mu(n)\psi(n+\hat{\mu}) - U_{-\mu}(n)\psi(n-\hat{\mu})}{2a} + m\psi(n)\Big), \tag{3.21}$$

To extract the Dirac operator, dropping all the internal indices we rewrite the action as

$$S_F[\psi,\overline{\psi},U] = a^4 \sum_{n,m\in\Lambda} \overline{\psi}(n)D(n|m)\psi(m)), \tag{3.22}$$

thus the Dirac operator reads

$$D(n|m) = \sum_{\mu=1}^{4}\gamma_\mu \frac{U_\mu(n)\delta_{n+\mu,\hat{m}} - U_{-\mu}(n)\delta_{n-\hat{\mu},m}}{2a} + m\delta_{n,m}. \tag{3.23}$$

The Fourier transform of the Dirac operator, for trivial gauge field reads

$$\begin{aligned} D(p|q) &= \frac{1}{|\Lambda|}\sum_{n,m\in\Lambda} e^{-ip\cdot na} D(n|m) e^{iq\cdot ma} \\ &= \frac{1}{|\Lambda|}\sum_{n\in\Lambda} e^{-i(p-q)\cdot na}\Big(\sum_{\mu=1}^{4}\gamma_\mu \frac{e^{iq_\mu a}-e^{-iq_\mu a}}{2a} + m\mathbb{1}\Big) \\ &= \delta(p-q)\tilde{D}(p), \end{aligned} \tag{3.24}$$

where $|\Lambda|$ is the total number of lattice points. Finally the Dirac operator in Fourier space reads

$$\tilde{D}(p) = \frac{i}{a}\sum_{\mu=1}^{4}\gamma_\mu \sin(p_\mu a) + m\mathbb{1}. \tag{3.25}$$

The propagator of free quarks is given by $\tilde{D}^{-1}(p)$. Using the relation

$$\Big(a\mathbb{1} + i\sum_{\mu=1}^{4}\gamma_\mu b_\mu\Big)^{-1} = \frac{a\mathbb{1} - i\sum_{\mu=1}^{4}\gamma_\mu b_\mu}{a^2 + \sum_{\mu=1}^{4} b_\mu^2}, \tag{3.26}$$

for massless quarks, we arrive at

$$\tilde{D}^{-1}(p) = \frac{ia^{-1}\sum_{\mu=1}^{4}\gamma_\mu \sin(p_\mu a)}{a^{-2}\sum_{\mu=1}^{4}\sin(p_\mu a)^2} \tag{3.27}$$

The above relation has the correct continuum limit, though in contrast to the continuum massless quark propagator it has more than one pole. Due to the sin function in the denominator we get a pole not only at $p = (0,0,0,0)$ but also at any momentum with componants $p_\mu = n_\mu \frac{\pi}{a}$, where n_μ is an integer. In the first Brillouin zone we get, 15 more poles than what we get in the continuum. These unphysical poles are called doublers. To remove these unphysical poles, Wilson added a mass-like term to the Dirac operator, so that the modified Dirac operator reads

$$\tilde{D}(p) = \frac{i}{a}\sum_{\mu=1}^{4}\gamma_\mu \sin(p_\mu a) + m\mathbb{1} + \mathbb{1}\frac{1}{a}\sum_{\mu=1}^{4}(1-\cos(p_\mu a)) \tag{3.28}$$

The last term, the so-called Wilson term vanishes at $p = (0,0,0,0)$, while for $p_\mu = \pi/a$ it acts like a mass term proportional to $1/a$ thus even for $m = 0$, doublers gain a mass that goes to infinity in the continuum limit $a \to 0$. Therefore in the continuum limit they decouple from the theory. In this way these unphysical poles do not survive in the continuum. But the Wilson term breaks chiral symmetry of the action explicitly, making the study of chiral symmetry and its spontaneous breaking technically very difficult on the lattice. There are other formulations of fermion actions on the lattice, like the so-called staggered fermions formalism, that reduces the effect of the doublers, but keeps the chiral symmetry of the action intact.

After the Fourier transformation of equation (3.28) and inserting the link variables to make it gauge invariant, The operator reads

$$D(n|m) = (m + \frac{4}{a})\delta_{n,m} - \frac{1}{2a}\sum_{\mu=\pm1}^{\pm4}(1-\gamma_\mu)U_\mu(n)\delta_{n+\hat{\mu},m} \tag{3.29}$$

$$\gamma_{-\mu} \equiv -\gamma_\mu \tag{3.30}$$

Wilson's Dirac action preserves certain symmetries, among them γ_5-hermiticity is important for the reality of the fermion determinant. In the next section we will explain this symmetry and its consequences.

3.3.2 γ_5-hermiticity

The property of γ_5-hermiticity of the Dirac operator is defined as follows

$$(\gamma_5 D)^\dagger = \gamma_5 D \Rightarrow D^\dagger = \gamma_5 D \gamma_5 \tag{3.31}$$

The mass term $m + 4/a$ obviously satisfies the above relation, using $\gamma_5^2 = 1$. We thus only need to verify it for the hopping term. Multiplying γ_5 from left and right to the hopping term and using $\{\gamma_\mu, \gamma_5\} = 0$ we have

$$\begin{aligned}
&\sum_{\mu=\pm1}^{\pm4}\gamma_5(\mathbb{1}-\gamma_\mu)\gamma_5 U_\mu(n)\delta_{n+\hat{\mu},m} = \sum_{\mu=\pm1}^{\pm4}(1+\gamma_\mu)U_\mu(n)\delta_{n+\hat{\mu},m} \\
&= \sum_{\mu=\pm1}^{\pm4}(1-\gamma_\mu)U_{-\mu}(n)\delta_{n-\hat{\mu},m} = \sum_{\mu=\pm1}^{\pm4}(1-\gamma_\mu)U_\mu(n-\hat{\mu})^\dagger\delta_{n-\hat{\mu},m} \\
&= \sum_{\mu=\pm1}^{\pm4}(1-\gamma_\mu)U_\mu(m)^\dagger\delta_{n,m+\hat{\mu}}
\end{aligned} \tag{3.32}$$

where in the second line we use equation (3.30) and in the last line equation (3.6) has been used. To obtain the final result we use the δ-function to replace $n - \hat{\mu}$ by m and we also use the equivalence of $\delta_{n-\hat{\mu},m} \equiv \delta_{n,m+\hat{\mu}}$. Thus we prove equation (3.31). In the following we show how this property is used in the discussion of the reality of the fermion determinant and what is its relevance for the simulation of QCD on the lattice . Using γ_5 hermiticity one can show that, if λ is an eigenvalue of Wilson's Dirac operator so is λ^* thus the fermion determinant is always real. In the next section we introduce the chemical potential to the Wilson's Dirac operator and we see how this affects our conclusion about the reality of the determinant.

3.4 Introduction of the chemical potential

The chemical potential is a measure of the charge density (particle-antiparticle difference) in the system. Particles and antiparticles travel oppositely in the time direction. Therefore the non-zero chemical potential is introduced via an asymmetry between the forward and the backward hopping terms in the time direction, as formulated in the following

$$\begin{aligned} D_4 = -\frac{1}{2a}\sum_{n\in\Lambda} \big(& f(a\mu)(1-\gamma_4)U_4(n)\,\delta_{n+\hat{4},m} \\ &+ f(a\mu)^{-1}(1+\gamma_4)U_4(n-\hat{4})^\dagger\,\delta_{n-\hat{4},m}\big). \end{aligned} \tag{3.33}$$

The asymmetry is manifest by two different factors for the forward and the backward terms. Since the dominance of the positive charge is equivalent to the suppression of the negative one, these two factors are inverse to each other. For $\mu = 0$, the original form of the Dirac operator should be restored, thus $f(0) = 1$. Time reversal invariance which demands the invariance of the Dirac operator under the exchange of the positive and the negative time directions $4 \leftrightarrow -4$, corresponding to the exchange of negative and positive charges ($\mu \to -\mu$), requires $f(-a\mu) = 1/f(a\mu)$. The simplest choice fulfilling these conditions is

$$f(a\mu) = \exp(a\mu). \tag{3.34}$$

Replacing the time sector of the Dirac operator by (3.33) implies that in order to manifest γ_5 hermiticity of the Dirac operator, we need to have $f(a\mu) = 1/f^*(a\mu)$. The only real value satisfying this condition is $f = 1$. Thus the Dirac operator at finite density no longer satisfies (3.31) and therefore its determinant can become complex. This has a direct effect on the possibility of Monte-Carlo simulations on the lattice at finite density. With a complex fermion determinant the weight factor in the path integral is not anymore real and positive, thus it can not play the role of a probability in the simulation. This difficulty is known as the sign problem. In the last part of this section we will have a quick look at the various methods of dealing with or circumventing the sign problem on the lattice.

3.4.1 The sign problem and its "solutions"

In this section we will have a closer look at the technical aspects of the sign problem, also known as the complex action problem for reasons to become clear in this section, following [24]. We may try to deal with this problem by simulating the phase quenched theory, i.e., take the absolute value of the determinant as a part of the weight factor and absorb its phase in the definition of an observable. The full expectation value $\langle O\rangle_{full}$ in terms of the phase quenched one $\langle O\rangle_{pq}$ is given by

$$\langle O\rangle_{full} = \frac{\langle e^{i\phi}O\rangle_{pq}}{\langle e^{i\phi}\rangle_{pq}} \tag{3.35}$$

$$Z_{full} = e^{\Omega f},\quad Z_{pq} = e^{\Omega f_{pq}} \tag{3.36}$$

$$\langle e^{i\phi}\rangle_{pq} = \frac{Z_{full}}{Z_{pq}} = e^{-\Omega\Delta f} \tag{3.37}$$

Where $\Omega = \frac{V}{T}$ and $\Delta f = f - f_{pq}$. $Z_{full} \leq Z_{pq}$ thus $\Delta f \geq 0$. Unless $f = f_{pq}$, in the thermodynamics limit $\Omega \to \infty$, the denominator of $\langle O\rangle_{full}$ goes to zero and the expectation value is not anymore well defined. Since the severity of this problem grows exponentially with the volume, the sign problem is known as an exponentially hard problem. In the following we mention some of the approaches, developed in order to treat this problem.

From the previous section we remember that γ_5 hermiticity in the presence of the chemical potential requires $f^* = 1/f$ which is not satisfied for a real chemical potential implemented by $f(a\mu) = \exp(-a\mu)$. In contrast $f(a\mu)$ as a function of an imaginary chemical potential μ_I, would satisfy the requirement, thus it maintains the reality of the fermion determinant. The method of imaginary chemical potential, performs the simulation in the region, where $\mu^2 < 0$ and by analytical continuation, extrapolates the results to the physical region where the chemical potential is real. Taylor expansion is another method of studying QCD at finite μ on the lattice. It is applicable to the region where $\mu/T \ll 1$ so for small chemical potentials and large temperatures. As a result this method is not applicable to the case of cold dense matter, a typical example of this situation is the inside of neutron stars.

Studying QCD-like theories as we described previously, a way to circumvent the sign problem on the lattice, provides us with information that can be insightful for the case of real QCD at finite density. In Chapter 4 we study ghost and gluon correlation functions of QC$_2$D at finite density on the lattice. We present the lattice formulation of these quantities in the following section.

3.5 Gauge Correlation functions on the lattice

To calculate the gluon correlation functions on the lattice, we define the gluon field on the lattice, with lattice spacing a as follows

$$A^a_\mu(x) = \frac{\sqrt{\beta}}{4ia}\mathrm{tr}\tau^a(U_\mu(x) - U_\mu(x)^\dagger) + \mathcal{O}(a^2). \tag{3.38}$$

Where $\beta = 4D_f/g^2$ is related to the bare coupling g, which has dimension $a^{-\frac{4-d}{2}}$, d is the dimensionality of the space-time. D_f is the dimension of the fundamental representation of the gauge algebra. τ^a represents the generator of the algebra $a = 1, .., D_{adj}$, D_{adj} is the dimension of the adjoint representation and is given by $D_{adj} = D_f^2 - 1$.

In momentum space, the Fourier transform of $A^a_\mu(x)$ on the lattice reads

$$A^a_\mu(p) = e^{-\frac{i\pi P_\mu}{N_\mu}} \sum_X e^{2\pi i \sum_i \frac{P_i X_i}{N_i}} A^a_\mu(x). \tag{3.39}$$

As already seen from the fermion action the physical momentum p_i, in terms of the lattice one P_i is given by

$$p_i = \frac{2}{a}\sin\frac{P_i\pi}{N_i}. \tag{3.40}$$

P_i as the components of P assumes the integer values $-N_i/2+1, \ldots, N_i/2$ and the components X_i of X are the coordinates in the lattice ranging from 0 to $N_i - 1$. The periodic boundary conditions reduces the set of independent momenta to $0 ... N_i/2$.

The material, presented in this section is based on [25, 26, 27, 28].

3.5.1 Gluon propagator

The expectation value of the gluon propagator in position space is defined as follows

$$D^{ab}_{\mu\nu}(x-y) = \frac{1}{V}\langle A^a_\mu(x)A^b_\nu(y)\rangle. \tag{3.41}$$

The reality of the gluon fields in position space, gives the following result for the Fourier transform of the propagator

$$D^{ab}_{\mu\nu}(p) = \frac{1}{V}\langle A^a_\mu(p)A^b_\nu(-p)\rangle. \tag{3.42}$$

On the lattice, in Landau gauge, we calculate the $4D$ transverse projection of the above correlation function

$$D^{ab}_{\mu\nu}(p) = \sigma^{ab}_{\mu\nu}D(p),\ \sigma^{ab}_{\mu\nu} = (\delta_{\mu\nu} - \frac{p_\mu p_\nu}{p^2})\delta^{ab}D(p) = \frac{1}{\mathrm{V}N}\sum_{a,\nu}\langle(Re[A^a_\nu(p)])^2 + (Im[A^a_\nu(p)])^2\rangle \tag{3.43}$$

where V is the volume of the lattice and *N* is the number of the independent degrees of freedom. So that $N = (d-1)D_{adj}$ for $p \neq 0$ and $N = dD_{adj}$ for $p = 0$. The symmetries of the theory allow for taking the average over *N*. The Landau gauge condition reduces the independent space-time degrees of freedom to $d-1$, but only when $p \neq 0$. Otherwise, it stays at *d*, since for $p = 0$ the condition $P_\mu A_\mu = 0$, is not anymore a constraint.

3.5.2 Three-gluon vertex on the lattice

The full three-gluon vertex $\Gamma^{A^3,\,abc}_{\mu\nu\rho}$ is not directly available on the lattice, but one can evaluate the corresponding full Green's function

$$G^{A^3,\,abc}_{\mu\nu\rho}(p,q,k) = \frac{1}{V}\langle A^a_\mu(p)A^b_\nu(q)A^c_\rho(k)\rangle. \tag{3.44}$$

Due to the vanishing of any vector condensates in Yang-Mills theory, this Green's function equals the connected Green's function, but it is still necessary to amputate it. The relation of the full vertex $\Gamma^{A^3,\,def}_{\lambda\sigma\omega}(p,q,k)$ with the Green's function is then given by

$$G^{A^3,\,abc}_{\mu\nu\rho}(p,q,k) = D^{ad}_{\mu\lambda}(p)D^{be}_{\nu\sigma}(q)D^{cf}_{\rho\omega}(k)\Gamma^{A^3,\,def}_{\lambda\sigma\omega}(p,q,k). \tag{3.45}$$

Momentum conservation requires $k = -p - q$. Thus G^{A^3} is a function of p and q and the angle between them ϕ. The full three gluon vertex is given by

$$\Gamma = \sum_i f_i\Gamma^i, \tag{3.46}$$

where Γ^i represent the linearly independent tensor structures, constructed from three Lorentz vectors p_μ, q_ν and k_ρ and Kronecker delta of any possible pair of the three Lorentz indices, that are carried by the three gluons. The three gluon vertex as a composition of bosons must be symmetric under the exchange of its constituents, the color structure constant being antisymmetric, necessitates antisymmetric Lorentz structures. The Landau gauge condition requires another constraint to be satisfied by the relevant tensor structures so that finally we end up with four independent Lorentz tensors that construct the full three gluon vertex. To calculate the contribution of each tensor structure, we have to calculate the projection of $G^{A^3,\,abc}_{\mu\nu\rho}(p,q,k)$ on each of the tensor structures. The procedure is given in

$$G^{i,\,A^3}(p,q,\phi) = \frac{\Gamma^{i,\,A^3,\,abc}_{\mu\nu\rho}(p,q,k)\,G^{A^3,\,abc}_{\mu\nu\rho}(p,q,k)}{\Gamma^{i,\,A^3,\,abc}_{\mu\nu\rho}(p,q,k)\,D^{ad}_{\mu\lambda}(p)\,D^{be}_{\nu\sigma}(q)\,D^{cf}_{\rho\omega}(k)\,\Gamma^{i,\,A^3,\,def}_{\lambda\sigma\omega}(p,q,k)}, \tag{3.47}$$

where the denominator gives the correct normalization. Namely, if the only contributing structure were Γ^1 then from (3.45), we had $G^{i,\,A^3}(p,q,\phi) = 1$. In order to include the effects of discretization correctly, we use the lattice modification of these tensor structures. Here we present the explicit form of the lattice-improved tree-level tensor structure

$$\begin{aligned}\Gamma^{\mathrm{tl}\;L\;A^3\;abc}_{\mu\nu\rho}(p,q,k) = -igf^{abc}\,e^{i\pi(p_\mu+q_\nu+k_\rho)/N}[(\widetilde{q-k})_\mu\delta_{\nu\rho}\cos(\hat{p}_\nu) + (\widetilde{k-p})_\nu\delta_{\mu\rho}\cos(\hat{q}_\rho)\\ + (\widetilde{p-q})_\rho\delta_{\mu\nu}\cos(\hat{k}_\mu)].\end{aligned} \tag{3.48}$$

with the following definitions

$$\tilde{p}_\mu = 2\sin(\hat{p}_\mu)\,, \tag{3.49}$$

$$\hat{p}_\mu = \frac{\pi p_\mu}{N}, \tag{3.50}$$

where $\tilde{p}_\mu$ gives the physical momentum in lattice units and p_μ are the integer lattice momenta.

3.5.3 Ghost propagator

Ghosts are auxiliary degrees of freedom that are introduced to Yang-Mills theory in the process of gauge fixing. Gauge fixing is necessary to get rid of redundant degrees of freedom, which are gauge transforms of each other and thus physically equivalent. A gauge is fixed by inserting a non-trivial **1** to the action.

$$1 = \int \mathcal{D}\alpha(x)\delta(G(A^\alpha))det(\frac{\delta(G(A^\alpha))}{\delta\alpha}), \tag{3.51}$$

where A^α is the gauge field A which is transformed under the following infinitesimal gauge transformation

$$(A^a_\mu)^\alpha = A^a_\mu - D_\mu\alpha^a. \tag{3.52}$$

Here D_μ is the covariant derivative and α is the parameter of the gauge transformation. $\delta(G(A^\alpha))$ in (3.51) guarantees the gauge-fixing condition $G(A_\mu) = 0$. For the Landau gauge, $G(A^\alpha_\mu) =$

$\partial_\mu A^\alpha$, we have

$$\frac{\delta(G(A^\alpha))}{\delta\alpha} = -\partial_\mu D\mu. \tag{3.53}$$

Equation (3.53), represents the form of the Faddeev-Popov operator in the Landau gauge. Ghosts enters the formalism of the theory, when the determinant of this operator in equation (3.51) is interpreted as the result of a Grassmann integral over the Grassmann fields which live in the adjoint representation of the gauge group. In this sense the Faddeev-Popov operator is the kernel of the ghost action. The explicit form of this operator in the continuum is given by

$$M^{ab} \equiv -\partial_\mu D^{ab}_\mu = \delta(x-y)(-\partial^2\delta^{ab} + gf^{abc}\partial_\mu A^c_\mu). \tag{3.54}$$

On the lattice this operator is defined by its operation on the Lorentz scalar field $\omega^a(x)$, (where a is a color index)

$$\begin{aligned} &M^{ab}(x,y)\omega^b(y) = \\ &\delta_{xy}\sum_\mu \Big(G^{ab}_\mu(y)[\omega^b(y) - \omega^b(y+e_\mu)] - G^{ab}_\mu(y-e_\mu)[\omega^b(y-e_\mu) - \omega^b(y)] \\ &+\sum_c f^{abc}[A^b_\mu(y)\omega^c(y+e_\mu) - A^b_\mu(y-e_\mu)\omega^c(y-e_\mu)]\Big). \end{aligned} \tag{3.55}$$

The first two terms give the lattice equivalent of the second derivative operator $\partial^2\omega(x)$ and the last two terms are the lattice form of the operation of ∂_μ on $A_\mu(x)\omega(x)$. $G^{ab}_\mu(x)$ is defined by

$$G^{ab}_\mu(x) = \frac{1}{8}\mathrm{tr}\big(\{\sigma_a,\sigma_b\}[U_\mu(x) + U_\mu(x)^\dagger]\big), \tag{3.56}$$

which is proportional to δ^{ab}. Thus it appears as a factor of the terms composing the lattice corresponding of the second derivative term in (3.55) in analogy to the continuum operator in (3.54). By integrating out the ghost fields in the path integral the ghost propagator in terms of the Faddeev-Popov operator reads

$$D^{ab}_G(p) = \frac{1}{V}\langle (M^{-1})^{ab}(p)\rangle. \tag{3.57}$$

The challenging part is the calculation of the inverse of the real space Faddeev-Popov operator, $(M^{-1})^{ab}(x,y)$ to obtain the ghost propagator, given in (3.57)

$$(M^{-1})^{ab}(p,q) = \sum_{x,y} e^{2\pi i(px+qy)/N}(M^{-1})^{ab}(x,y). \tag{3.58}$$

which has been studied in [29].

3.5.4 Ghost-gluon vertex

The calculation of the ghost-gluon vertex is done along the same line as the three-gluon vertex. We calculate the ghost-gluon three point function given by

$$G_\mu^{c\bar{c}A\;abc}(x,y,z) = \langle A^a_\mu(x)\bar{c}^b(y)c^c(z)\rangle = \langle A^a_\mu(x)M^{bc-1}(y,z)\rangle. \tag{3.59}$$

on the lattice. The Fourier transformation reads

$$G_\mu^{c\bar{c}A\;abc}(p,q,k) \;=\; \frac{1}{V}\langle c^a(p)\bar{c}^b(q)A^c_\mu(k)\rangle. \tag{3.60}$$

Then we project it on the tensor structures, that are constructing the vertex. Since only the gluon carries the Lorentz index, the Lorentz tensors will be one dimensional, constructed from two independent Lorentz vectors, namely the independent momenta. The Landau gauge condition reduces the number of the possible structures to one which is the tree-level ghost gluon vertex given by

$$\Gamma_\mu^{\mathrm{tl}\;c\bar{c}A\;abc}(p,q,k) = igf^{abc}q_\mu. \tag{3.61}$$

The corresponding structure on the lattice reads

$$\Gamma_\mu^{\mathrm{tl}\;L\;c\bar{c}A,\;abc}(p,q,k) = igf^{abc}e^{i\pi k_\mu/N}\tilde{q}_\mu\cos(\hat{q}_\mu). \tag{3.62}$$

Again, the cosine and the exponential are lattice artifacts, going to 1 in the formal continuum limit $a \to 0$.

3.6 Simulation method

In the present section, we review basic conceptual aspects of the simulation of gauge theories on the lattice. The expectation value of an observable in the path integral formalism is given by

$$\langle O\rangle = \frac{1}{Z}\int D[U]e^{-S[U]}\,O[U],\; Z = \int D[U]e^{-S[U]}, \tag{3.63}$$

where $O[U]$ is an operator composed out of field variables U and $e^{-S[U]}$ gives the weight factor of the specific field configuration, with $S[U]$ as the action of the theory. The analytical calculation of the above integral is almost impossible for many of the physically interesting cases. We thus need to estimate it by a finite sum over many configurations which are weighted according to the weight factor $e^{-S[U]}$. A set of consecutive configurations, contributing to this sum is termed *Markov chain*. The procedure of generating such a set, to be called a *Markov process* is explained in the following:

We start from some arbitrary configuration, following a stochastic process, we generate configurations whose probability distribution eventually goes to the Boltzmann factor, which is the equilibrium probability distribution, presented by $P[U]$. In the following we investigate the main properties of a Markov process and then we propose an algorithm that generates the configurations according to these properties, the so-called *Metropolis algorithm*. If one imagines each field configuration to be a point in the configuration space, the Markov process is represented by an ordered set of points that is dense in the region with the largest weight factor $e^{-S[U]}$. The probability to get from the configuration U to the successive point U' in the Markov chain is denoted by $T(U'|U)$, and obeys the following relations

$$0 \leq T(U'|U) \leq 1, \ \sum_{U'} T(U'|U) = 1. \tag{3.64}$$

The first condition requires $T(U'|U)$ as a probability to be less or equal one and the second is the normalization condition. For the equilibrium probability, $P[U]$ we have

$$\sum_{U} T(U'|U)P[U] = \sum_{U} T(U|U')P[U']. \tag{3.65}$$

The above relation, termed *balance equation*, says that in equilibrium, the probability of going to a configuration is equal to the probability of going out of this configuration. Namely, there is no sink or source of probability in equilibrium. The probability $P[U]$ satisfying this relation is the equilibrium probability, applying the normalization condition in (3.64) we have

$$\sum_{U'} T(U|U')P[U'] = P[U]. \tag{3.66}$$

The equation (3.65) is the main clue to obtain an algorithm generating configurations according to the Markov process. A sufficient condition, whose solution satisfies (3.65) is

$$T(U'|U)P[U] = T(U|U')P[U'], \tag{3.67}$$

known as the *detailed balance condition*. In the following we introduce the *Metropolis algorithm* to generate a Markov chain, based on (3.67). The algorithm consists of the following steps, for one $update$, namely going from U_{n-1} to U_n

i: We choose an arbitrary configuration U' with a priori selection probability $T_0(U'|U)$

ii: This proposed configuration is accepted as our new configuration with probability

$$T_A(U'|U) \equiv \min\left(1, \frac{T_0(U|U')e^{-S[U']}}{T_0(U'|U)e^{-S[U]}}\right). \tag{3.68}$$

In most cases we consider $T_0(U|U') = T_0(U'|U)$ and thus the acceptance probability is essentially given by

$$T_A(U'|U) = e^{-\Delta S}, \tag{3.69}$$

where ΔS is the change in the action. Thus, an update which decreases the action is always accepted. If the update increases the action there is still a non-vanishing probability that the proposed configuration is accepted, accounting for fluctuations and preventing the algorithm from getting stuck in some local minimum. It can be shown that this procedure obeys the detailed balance condition. By repeating these two steps, we generate a Markov chain of configurations.

Chapter 4

Ghost and Gluon correlation functions of QC_2D

In Chapter 2, we explained the applications of studying QCD-like theories on the lattice especially at finite densities. In this chapter we present the results of the study of the gluon and the ghost correlation functions of QC_2D in vacuum and at finite temperature and density. The content of this chapter is to appear in a future publication. Here we review our motivations of studying the gauge sector.

One of the most important gauge correlation functions are propagators. In the quenched regime of QCD the problem of confinement is related to the IR behavior of ghost and gluon propagators [30, 27]. According to Gribov-Zwanziger and Kugo-Ogima scenarios, the ghost propagator is IR enhanced, while the gluon propagator is suppressed in that regime. Since at low energies physics of the strong interaction is dominated by hadrons and therefore color singlet objects, it was suggested to consider quarks in a static state and derive the dynamics out of the behavior of the gauge sector. This was part of the motivation of studying YM theories.

On the other hand we need to answer the question about the relevance of the study of the gauge variant quantities for the physics, which is gauge invariant. One motivation is that the lattice is affected by artifacts which are not present in other non-perturbative, yet first principle approaches like functional methods (DSE and FRG). These methods usually should deal with an infinite number of coupled differential equations involving gauge variant objects. Thus various truncation schemes and gauge fixing is applied to solve these equations. Lattice can provide benchmarks for approximations and truncations, necessary for these methods.

Furthermore in many cases these methods need a gauge variant input for their calculation of gauge-invariant quantities, these inputs are calculated in a non-perturbative manner on the lattice and is inserted to the equations resulting from functional methods.

Apart from providing bench marks or inputs for other non-perturbative methods, studying gauge variant objects on the lattice is important on its own because of its application in the calculation of the quark mass, the strong coupling constant and the chiral condensate. They can be obtained by the calculation of quark and gluon propagators and higher n-point functions [31, 32, 33].

The main focus of this chapter, is on the gauge sector of QC_2D at finite density, i. e. the minimal Landau-gauge [28] gluon and ghost propagators as well as their 3-point vertices on the lattice. This extends previous studies of the gluon propagator alone [34]. In addition, as a derived quantity, we will also determine the running coupling in the miniMOM scheme [35]. For comparison, we study the same theory in the vacuum and at finite density, as well as pure Yang-Mills theory.

The details of the simulations are laid out in Section 4.1. A study of systematic errors is relegated to appendix 4.7. Results in the vacuum will be discussed in Section 4.3 and at finite temperature in 4.4.

The main results at finite density and zero temperature are shown in Section 4.5. Unexpectedly, we do not observe any substantial dependency of the studied correlation functions on the density, even when crossing the observed [36, 37, 16, 34, 38, 39, 40] transition of this theory, except for the slight attenuation of the gluon propagator already seen in [34]. Especially, the running coupling remains strong throughout the whole density range. These findings will be summarized in Section 4.6.

On the one hand, our findings imply that keeping the gauge sector only slightly modified in continuum calculations, as was done in [41, 42, 43, 44], is well justified. On the other hand, this implies that the transition observed is driven by the quarks, and is not into a weakly-coupled regime. This is actually in-line with the observations made for the Wilson potential [36, 37, 16, 34]. This result should be contrasted with the observation that at low densities the matter is an essentially free diquark superfluid after the silver blaze point [36, 37, 16, 34, 45, 46], while this is no longer true beyond the phase transition at larger densities.

Some preliminary results have been available in [47].

4.1 Setup, observables, and technical details

4.1.1 Configurations

Table 4.1: Employed lattice parameters and number of configurations. Note that a 'residual' temperature due to the finite lattice extent will be given as zero.

N_s	N_t	β	κ	a^{-1} [GeV]	L [fm]	T [MeV]	μ [MeV] ($a\mu$)	aj	Configuration
32	32	1.6	0.182	0.741	8.51	0	0	0	2000
32	32	1.7	0.178	0.857	7.36	0	0	0	1014
12	24	1.9	0.168	1.06	2.23	0	0	0	313
32	32	1.9	0.168	1.06	5.95	0	0	0	640
12	24	1.9	0.168	1.06	2.23	0	265 (0.250)	0.02 0.04	50 127
12	24	1.9	0.168	1.06	2.23	0	318 (0.300)	0.02 0.03 0.04	102 54 160

Continued on next page

Table 4.1 continued

N_s	N_t	β	κ	a^{-1} [GeV]	L [fm]	T [MeV]	μ [MeV] ($a\mu$)	aj	Configuration
16	24	1.9	0.168	1.06	2.98	0	318 (0.300)	0.04	1960
32	32	1.9	0.168	1.06	5.95	0	318 (0.300)	0.04	299
12	24	1.9	0.168	1.06	2.23	0	345 (0.325)	0.02	48
								0.04	128
12	24	1.9	0.168	1.06	2.23	0	371 (0.350)	0.02	49
								0.04	284
12	24	1.9	0.168	1.06	2.23	0	392 (0.370)	0.04	126
12	24	1.9	0.168	1.06	2.23	0	398 (0.375)	0.02	52
								0.04	153
12	24	1.9	0.168	1.06	2.23	0	403 (0.380)	0.04	126
12	24	1.9	0.168	1.06	2.23	0	424 (0.400)	0.02	42
								0.04	138
16	24	1.9	0.168	1.06	2.98	0	424 (0.400)	0.04	100
12	24	1.9	0.168	1.06	2.23	0	451 (0.425)	0.02	52
								0.04	136
12	24	1.9	0.168	1.06	2.23	0	477 (0.450)	0.02	68
								0.04	181
								0.06	34
12	24	1.9	0.168	1.06	2.23	0	488 (0.460)	0.04	60
12	24	1.9	0.168	1.06	2.23	0	498 (0.470)	0.04	158
12	24	1.9	0.168	1.06	2.23	0	504 (0.475)	0.04	50
12	24	1.9	0.168	1.06	2.23	0	509 (0.480)	0.04	164
12	24	1.9	0.168	1.06	2.23	0	519 (0.490)	0.04	165
12	24	1.9	0.168	1.06	2.23	0	530 (0.500)	0.02	49
								0.03	54
								0.04	158
16	24	1.9	0.168	1.06	2.98	0	530 (0.500)	0.04	2000
32	32	1.9	0.168	1.06	5.95		530 (0.500)	0.04	126
12	24	1.9	0.168	1.06	2.23	0	557 (0.525)	0.04	283
12	24	1.9	0.168	1.06	2.23	0	583 (0.550)	0.02	52
								0.04	52
								0.06	36
12	24	1.9	0.168	1.06	2.23	0	610 (0.575)	0.04	166
12	24	1.9	0.168	1.06	2.23	0	636 (0.600)	0.02	50
								0.04	31
16	24	1.9	0.168	1.06	2.98	0	636 (0.600)	0.04	100
12	24	1.9	0.168	1.06	2.23	0	689 (0.650)	0.02	52
								0.04	149
12	24	1.9	0.168	1.06	2.23	0	742 (0.700)	0.02	50
								0.03	50
								0.04	116
16	24	1.9	0.168	1.06	2.98	0	742 (0.700)	0.04	2000

Continued on next page

Table 4.1 continued

N_s	N_t	β	κ	a^{-1} [GeV]	L [fm]	T [MeV]	μ [MeV] ($a\mu$)	aj	Configuration
12	24	1.9	0.168	1.06	2.23	0	795 (0.750)	0.02	50
16	24	1.9	0.168	1.06	2.98	0	795 (0.750)	0.04	120
12	24	1.9	0.168	1.06	2.23	0	848 (0.800)	0.02	50
								0.04	142
16	24	1.9	0.168	1.06	2.98	0	848 (0.800)	0.04	120
12	24	1.9	0.168	1.06	2.23	0	901 (0.850)	0.02	50
12	24	1.9	0.168	1.06	2.23	0	954 (0.900)	0.02	48
								0.03	51
								0.04	67
16	24	1.9	0.168	1.06	2.98	0	954 (0.900)	0.04	1100
12	24	1.9	0.168	1.06	2.23	0	1007 (0.950)	0.02	50
12	24	1.9	0.168	1.06	2.23	0	1060 (1.000)	0.02	50
								0.04	126
12	24	1.9	0.168	1.06	2.23	0	1166 (1.100)	0.02	50
								0.04	88
48	32	1.7	0.178	0.857	8.10	27	0	0	302
32	8	1.9	0.168	1.06	5.95	133	0	0	2000

In the following we use ensembles which have been created using the methods described in [36, 16, 34]. Most of these configurations have also been used in these works. They were created using an unimproved Wilson gauge action with 2 flavors of unimproved Wilson quarks[1]. The details of the employed lattice parameters and the number of configurations are listed in table 4.1. For purpose of comparisons we have used besides the finite-density simulations also simulations in the vacuum and at zero density and finite temperature below the critical one. The quark mass parameter at finite density was fixed to $\kappa = 0.168$, which corresponds to rather heavy pions with mass $m_\pi = 717(25)$ MeV. In comparison, at $\beta = 1.7$ and $\kappa = 0.178$ it is 668(6) MeV [16].

We shortly remind the reader of the following definitions: $\beta = 4D_f/g^2$, where D_f is the dimension of the fundamental representation and g is the bare coupling. $\kappa = \frac{1}{am+4}$, where am represents the mass of quarks in lattice unit.

For the coarsest and the finest lattices at $\beta = 1.6$ and $\beta = 1.9$ lattice spacings have been determined using hadronic observables in [36, 16, 34], corresponding to $a = 0.266$ fm and $a = 0.186$ fm. Using various observables to interpolate, most notably the running coupling to be discussed below, we estimate the lattice spacing at $\beta = 1.7$ to be $a = 0.23$ fm [2], which we will be using throughout.

At finite density a diquark condensation is expected to take place in 2-color QCD [51]. As this is a spontaneous symmetry breaking, this requires a limiting process of explicit breaking on a lattice [52, 53]. To this end, a diquark source j is introduced [34], and varied over a range given

---

[1] Note that for the employed lattice parameters there are potentially various bulk issues [48]. However, the gauge quantities investigated here have not shown any sensitivity to such problems [49], and are therefore likely safe.

[2] In [50] the lattice spacing for $\beta = 1.7$ using the static quark potential is calculated to be $a = 0.229(3)$ fm, which is compatible to our result.

in table 4.1. In principle, an extrapolation to zero j is then necessary. However, as discussed in appendix 4.7, essentially no statistically significant dependency on j is found for the quantities investigated here.

The configurations have afterwards been fixed to minimal Landau gauge using an adaptive stochastic overrelaxation algorithm [27]. We will occasionally compare to results from pure Yang-Mills theory. For this purpose, we will use results from [49, 9, 54, 55], using as far as possible the same lattice volumes and discretizations. This will allow to estimate the unquenching effects as well as the influence of the finite-density environment. At finite temperature, we will compare to results at roughly the same ratio T/T_c, where $T_c = 217(23)$ MeV in the QC$_2$D case [34].

4.2 Observables

In Section 3.5, we introduce the correlation functions of ghost and gluon fields and their formulation on the lattice. In the present section we review the formulation of propagators at finite temperature and density, we also introduce, derived quantities like the running coupling that are also calculated at finite density and temperature as well as in vacuum.

4.2.1 Propagators

We formulate the longitudinal ((chromo)electric) and transverse ((chromo)magnetic) dressing functions of the gluon propagator, with respect to the heat bath [56] in the following

$$D_T(p_0,\vec{p}^2) = \frac{1}{(d-2)N_g}\left\langle \sum_{\mu=1}^{3} A_\mu^a(p)A_\mu^a(-p) - \frac{p_0^2}{\vec{p}^2}\, A_0^a(p)A_0^a(-p) \right\rangle, \tag{4.1}$$

$$D_L(p_0,\vec{p}^2) = \frac{1}{N_g}\left(1+\frac{p_0^2}{\vec{p}^2}\right)\langle A_0^a(p)A_0^a(-p)\rangle, \tag{4.2}$$

Here, $d = 4$ is the dimensionality and $N_g = 3$ is the number of gluons. In the vacuum, both coincide, $D_T = D_L = D$.

As already discussed, gauge bosons are introduced to guarantee gauge invariance of the Lagrangian. However, this leads to the divergence of the path integral due to the multiple counting of the physically equivalent configurations (equivalent up to a gauge transformation). This infinity is not a problem in itself and can be fixed by a normalization constant. The problem is that the local gauge invariance, implies that the quadratic part of the gauge action density has zero eigenvalues thus the propagator of the gauge field cannot be defined. The gauge fixing procedure, involves the introduction of the Faddeev-Popov determinant. A more detailed explanation has been given in Section 3.5. The definition of the Faddeev-Popov operator is

$$M_{ab} = -\partial_\mu D_\mu^{ab}. \tag{4.3}$$

The determinant of this operator appears in the path integral. Using the properties of Grassmann numbers, it can be written as a Grassmann integral over the so called ghost fields. The importance of this reformulation is rooted in the non-Abelian structure of the theory, that due to the covariant derivative, it couples the gluon fields to the ghost field and therefore, the ghost correlation functions must be taken into account in the study of the dynamical effects of non-Abelian gauge theory.[3] In the following we define the ghost propagator,

$$D_G(p_0, \vec{p}^2) = \frac{1}{V}\langle (M^{-1})^{aa}(p)\rangle. \tag{4.4}$$

We studied this propagator for both hard modes and soft modes.

4.2.2 Schwinger function

Mass and widths of the particle are among the properties encoded in the propagator, which can be read from the Schwinger function, defined on the lattice as follows [57]

$$\Delta(t) = \frac{1}{a\pi}\frac{1}{N_t}\sum_{P_0=0}^{N_t-1}\cos\left(\frac{2\pi t P_0}{N_t}\right) D(P_0^2), \tag{4.5}$$

where N_t is the size of the temporal extension, and P_0 is the Matsubara frequency. Thus this function carries information of the lowest energy modes, termed soft-modes. Since the mass of the particle is the lowest energy that can be carried by the particle, these modes are informative about the mass of the particle. The stability of a particle is signaled by the reality of the pole mass. For example the free scalar particle with propagator $D(p) = \frac{1}{p^2+m^2}$ has a Schwinger function $\Delta(t) \sim e^{-mt}$. An unstable particle with complex pole mass has an oscillatory Schwinger function [58], The results of the gluon Schwinger function will be presented in the following sections, where we will try to interpret it, with regard to the pole mass $\tilde{m}$ properties, that is defined by

$$\tilde{m} = -\frac{d\ln(\Delta(t))}{dt}. \tag{4.6}$$

Another quantity that reveals the properties of the zero modes of the degrees of freedom is the screening mass that encodes the interaction properties, and is defined as follows,

$$m = \frac{1}{\sqrt{D(0)}}. \tag{4.7}$$

The main distinction between these two kinds of masses is that the screening mass is a renormaliztaion dependent quantity but the pole mass is a renormalization group invariant quantity, so in principle it can be a physical quantity though in our case it is gauge-dependent [28].

---

[3] It is worth to mention that in the abelian case the equivalent relation for the Faddeev-Popov operator, the covariant derivative is replaced by the normal partial derivative, thus no coupling of the ghosts to the gauge field.

4.2.3 Running coupling

The running coupling is a measure of the strength of an interaction in QFT. In order to understand the dynamics behind phenomena like confinement and hadronizations in low energy and also the high precision measurements in hadron scattering experiments at high energies, all driven by QCD interaction, we need to have a good knowledge of the behavior and values of the running coupling for the whole momentum regime. Perturbative calculations result in asymptotic freedom at high energies, they also predict an ever increasing coupling at low energies. The latter is neither phenomenologically nor non-perturbatively confirmed. A phenomenological argument for the break-down of the perturbative prediction, originates in phenomena like hadronization and color-confinement, where the quark and gluon loops are suppressed and hadrons become the main degrees of freedom.

Here for the first time we present the result of calculating the running coupling of QC$_2$D at finite density on the lattice and we compare the result with quenched and unquenched vacuum results. The unquenched results at finite temperature will be also compared to the finite temperature $SU(2)$ Yang-Mills results. We use the ghost-gluon vertex to define the running coupling. In the vacuum, it is defined as [59, 35]

$$\alpha(p^2) = \alpha(\mu^2) p^6 D_G^2(p^2) D(p^2), \tag{4.8}$$

$$\alpha(\mu^2) = \frac{1}{\pi\beta}. \tag{4.9}$$

Where as in the previous sections $D_G(p)$ and $D(p)$ denote respectively ghost and gluon propagators.

Thus at finite density and temperature, longitudinal and transverse couplings read

$$\alpha_T(p_0, \vec{p}^2) = \alpha(\mu^2)(p_0^2 + \vec{p}^2)^3 D_G^2(p_0, \vec{p}^2) D_T(p_0, \vec{p}^2), \tag{4.10}$$

$$\alpha_L(p_0, \vec{p}^2) = \alpha(\mu^2)(p_0^2 + \vec{p}^2)^3 D_G^2(p_0, \vec{p}^2) D_L(p_0, \vec{p}^2). \tag{4.11}$$

4.2.4 Vertices

Vertices describe the basic interactions between the elementary degrees of freedom of QCD and are thus crucial for the understanding of non-trivial phenomena driven by strong interactions. The properties of vertices, in particular in the momentum regime about the momentum of constituent quarks, are important for the formation of bound states. Furthermore, the far infrared behavior of vertices should be connected to the confining properties of the theory, since confinement necessarily originates in the interaction of the fields. Therefore, a determination of these vertices is important for the understanding of the non-perturbative aspects of QCD. Finally, in QCD the vertices are also important for the breaking of chiral symmetry, and thus are a central ingredient in the understanding of hadron physics [60]. A nonperturbative investigation of the structure of the ghost-gluon vertex is also important for studies of gluon and ghost propagators using Dyson-Shwinger equations (DSE). In fact, in these studies, one makes use of Ansätze for the behavior of the propagators and vertices in the equations, in order to obtain solvable truncation schemes. Of course, a nonperturbative input for these quantities is important for a truly non-perturbative solution of the DSE [61]. To determine the dressing-function of the ghost-gluon vertex and the dressing-function of the tree-level tensor of the three-gluon vertex, we follow the procedures in [27], the detailed explanation has been presented in 3.5, here we summarize it, as follows

$$G = \frac{\Gamma V}{\Gamma D_1 D_2 D_3 \Gamma}. \tag{4.12}$$

Here Γ is the (lattice-improved) [62] tree-level vertex, V^c and V^3 are the three-point functions

$$V^C = \langle A_\mu^a (M^{bc})^{-1} \rangle \tag{4.13}$$

$$V^3 = \langle A_\mu^a A_\nu^b A_\rho^c \rangle \tag{4.14}$$

for the ghost-gluon and the three-gluon vertex, respectively. We use the same momentum configurations, one gluon momentum vanishing, two momenta orthogonal, and all momenta equal as in [27].

At finite temperature and finite density many more tensor structures contribute in the construction of the vertices. We follow here [55] and only consider the full transverse zero-modes of the tree-level vertices, corresponding to all Matsubara frequencies vanishing and using only the transverse propagators for amputation.

4.3 Vacuum results

According to several studies on the lattice [63, 64, 65], and in continuum [66, 67], inclusion of dynamical quarks does not affect the gauge sector of QCD dramatically. The main observed effect is the suppression of gluon propagator at mid-momentum. This effect can be understood with respect to the strengthened interaction via the inclusion of quarks that leads to larger screening mass. Recent results in continuum could be found in [68, 69].

For QC$_2$D, we see a similar behavior in Figure 4.1. The gluon dressing function is substantially suppressed at mid-momentum and in the infrared. This observation is in line with the other essential similarities of $SU(2)$ and $SU(3)$ in Yang-Mills sector. We also notice that the effect of lattice artifacts, from the coarsest to the two finer lattices is significant. The effect in the two finer lattices (unquenched data), is of similar order as for Yang-Mills theory. At large momenta the effect of the different anomalous dimensions also starts to emerge.

The Ghost dressing function is almost unaffected by the inclusion of the dynamical quarks, that can be understood in terms of the decoupling of the ghost from the matter sector. Consequently the running coupling given in equation (4.8) also qualitatively and quantitatively reproduces the Yang-Mills results in the momentum region of half to 1 Gev which is of great importance for the hadron phenomenology [70, 66, 71, 69, 72]. It only shows discrepancies at high momenta, that can be the effect of the anomalous dimension of the gluon propagator. Similarly, ghost-gluon vertex is unaffected by unquenching, that is seen in Figure 4.2.

Three-gluon vertex is the observable which is affected much stronger than the others by statistical fluctuations [27]. Thus, we can hardly make a firm statement based on Figure 4.3. However,

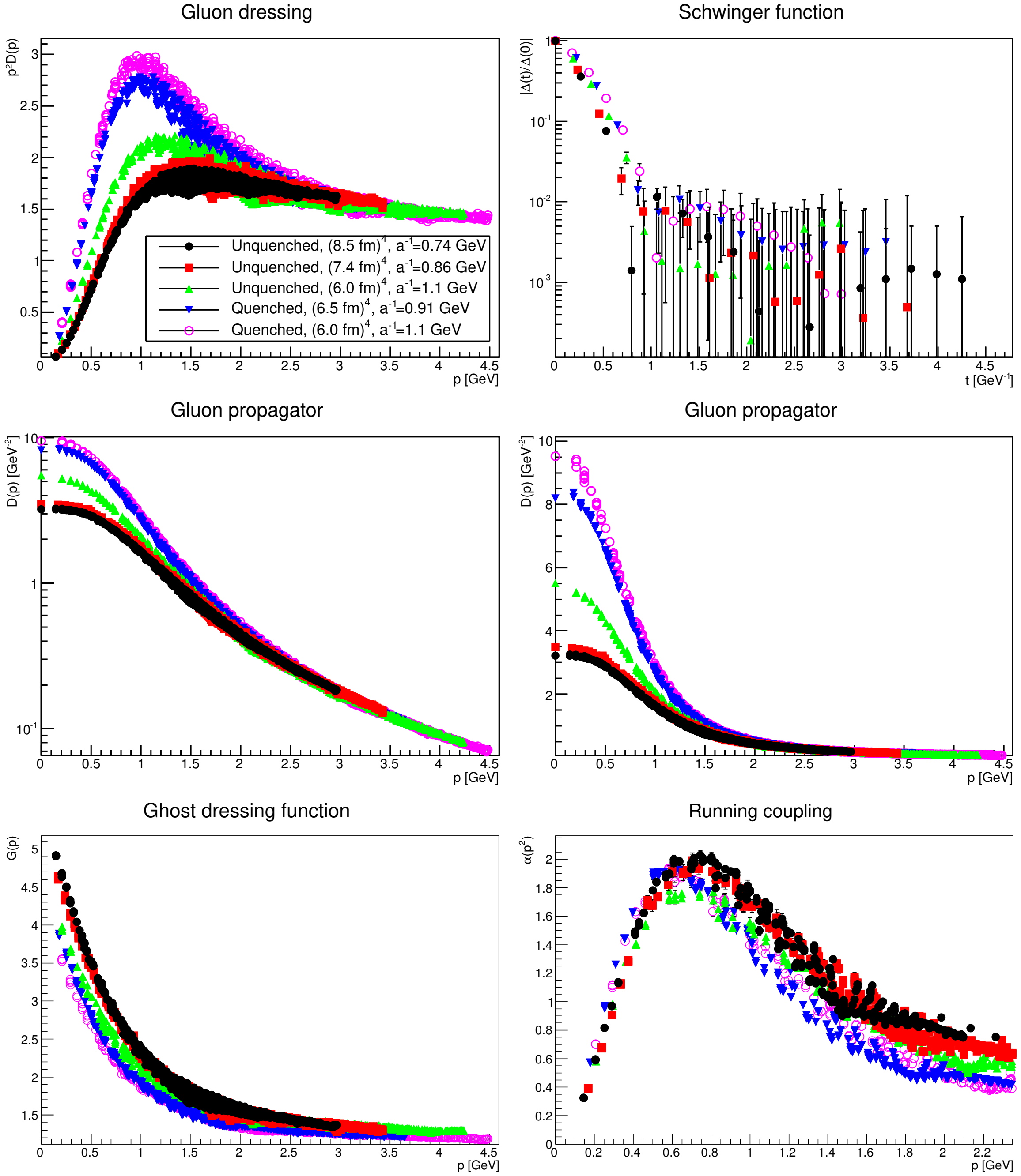

Figure 4.1: The quenched and unquenched gluon dressing function (top-left panel), Schwinger function (top-right panel), gluon propagator (middle panels, logarithmic and linear), ghost dressing function (bottom-left panel) and running coupling (bottom-right panel). Quenched data is from [49]. Error bars partly smaller than the symbol size. Results have not been renormalized.

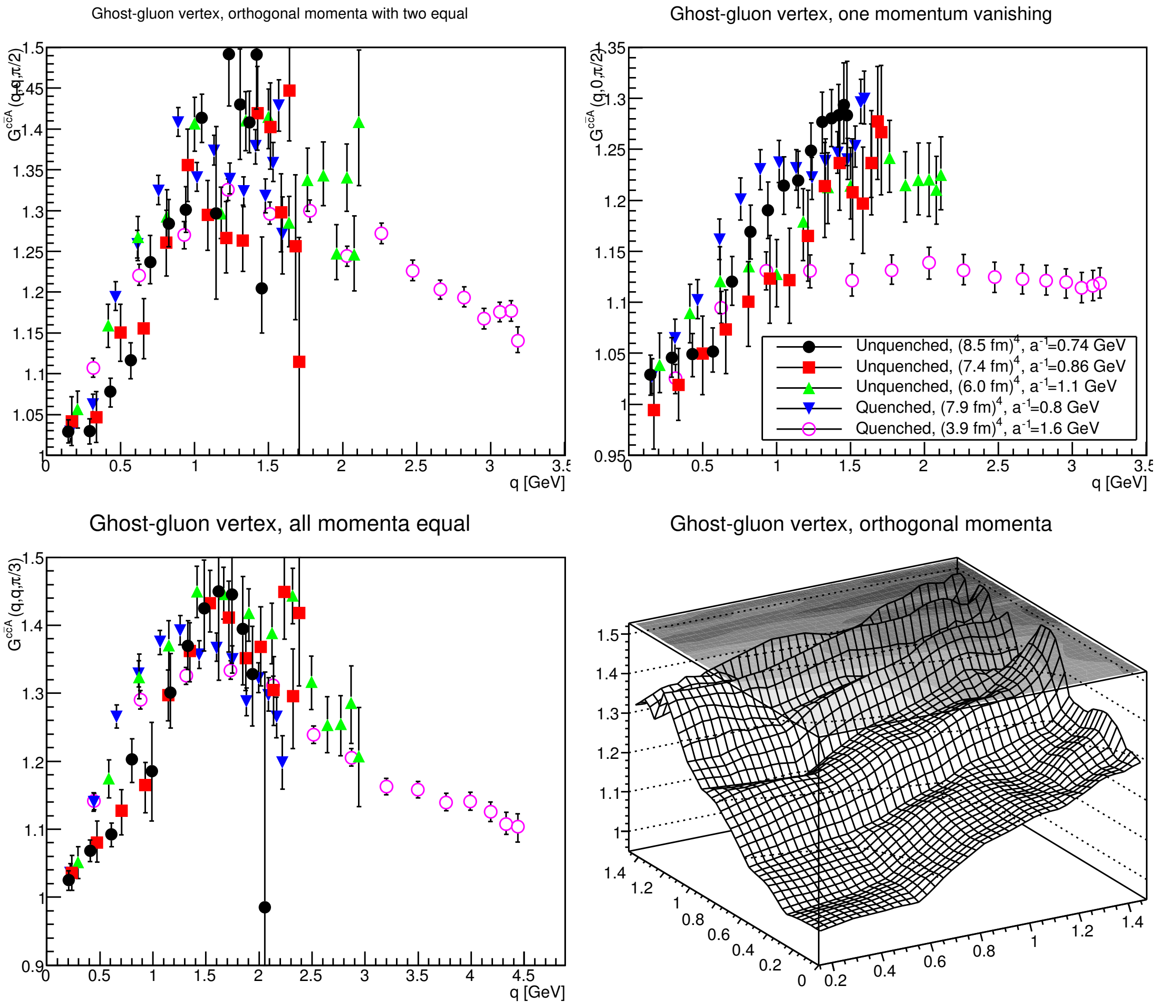

Figure 4.2: The ghost-gluon vertex dressing function for different momentum configurations in comparison to quenched data from [54]. See text for details. Results have not been renormalized.

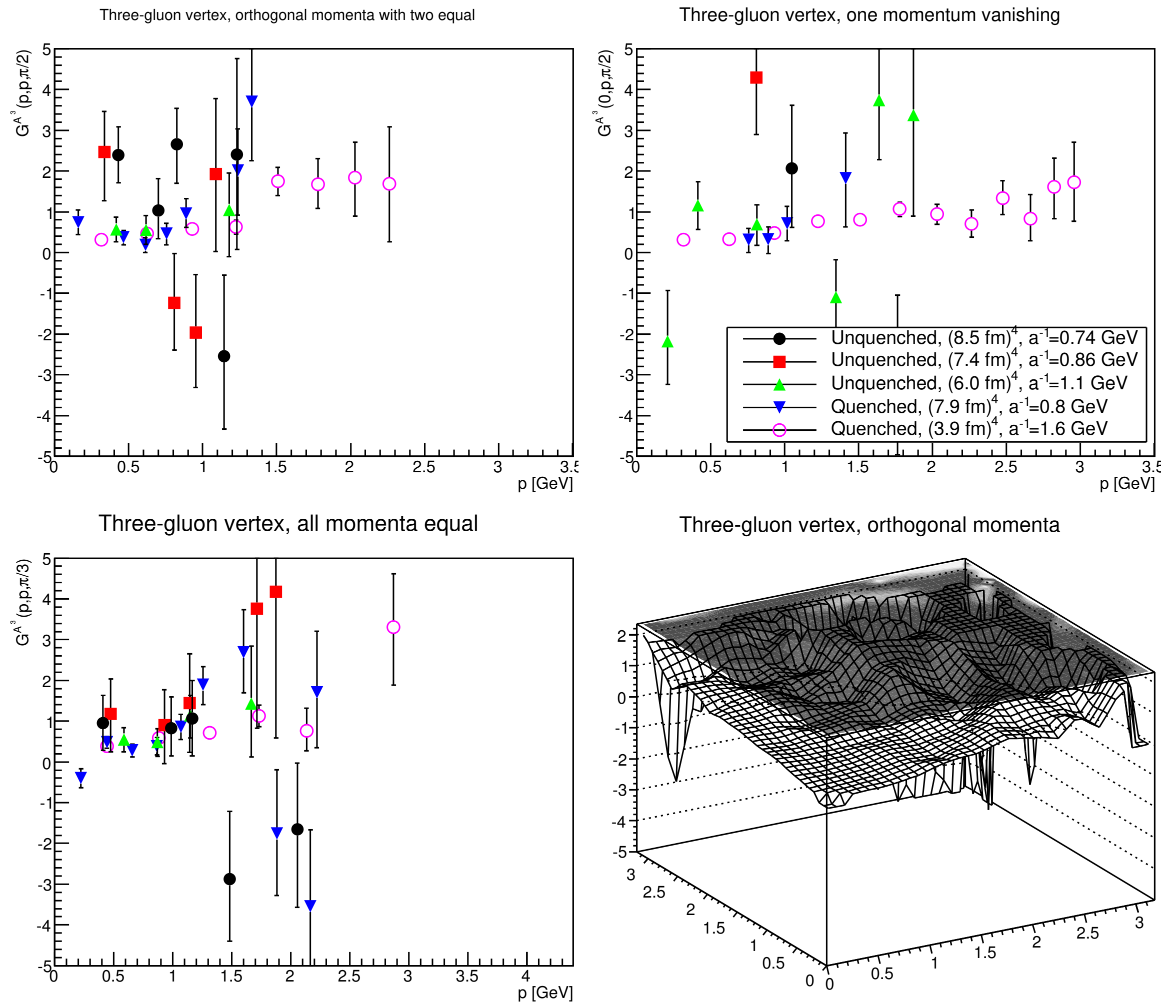

Figure 4.3: The three-gluon vertex dressing function for different momentum configurations in comparison to quenched data from [54]. Points with a relative error of larger than 100% have been suppressed. See text for details. Results have not been renormalized.

within the errors, the same trend as seen for other correlators is seen here, which shows almost no effect of the dynamical quarks.

4.4 Finite-temperature results

The study of the gluon propagator in $SU(2)$ and $SU(3)$ Yang-Mills theories, shows that the phase transition is signaled by the significant screening of the longitudinal gluon propagator, above T_c[9, 73, 74, 75, 76, 77]. For the unquenched case the only available temperatures are below T_c so we could not investigate the effects of a possible crossover. The screening effect of the unquenching, observed in the vacuum is also observed at finite temperature, comparing the data at $0.6T_c$, the corresponding effect is much more pronounced in longitudinal propagator than in the transverse one. However the effect, observed here, might be a finite volume effect.

Another observation is that in the unquenched case the longitudinal and transverse propagators are quantitatively very close compared to the Yang-Mills propagators in low momenta, suggesting that the effect of the temperature might be stronger in the quenched regime. This is in line with observations from 3-color QCD [63]. More precisely, there is an enhancement of electric propagator in low momenta but it is much weaker than the same effect in the quenched regime. This can be traced back into the apparently enhanced finite-volume effects in the low-temperature regime for the longitudinal one [9, 73, 74, 75, 76, 77]. Thus, the same pattern seems to emerge as in ordinary QCD. While not shown explicitly, the hard modes of Matsubara frequency n behave essentially as the soft modes evaluated at $(2\pi nT)^2 + \vec{p}^2$, as was already observed in the quenched case [9, 75]. Schwinger function in Figure 4.4 in the regime up to about $t = 1$ fm, shows significantly slower decay for the quenched case compared to all the unquenched results. A closer look at the unquenched results, would reveal that the longitudinal Schwinger function of the highest temperature, $T = 0.6T_c$, decays slightly slower than two others with the temperatures $T = 0$, $T = 0.1T_c$. At larger times the statistical noise precluded any statements, as shown in Figure 4.4.

The soft mode ghost dressing function[4], shown in Figure 4.4, shows no qualitative deviation from the quenched case in that it is not responding to temperature at all [9, 56, 13]. Although the unquenched high temperature data shows an enhancement with respect to the quenched data, but this might be a finite volume artifact rather than a physical effect. We can back up this speculation by the vacuum results seen in Figure 4.1, where there was no difference between quenched and unquenched data of the same volume and lattice spacing. Concerning the temperature dependence in the unquenched data, we do not see any systematic behavior. On one hand, the overlap of the data of the two lowest temperatures, signals no temperature dependence. On the other hand, a screening of ghost dressing function is observed at the highest temperature in the low momentum regime. These two observation are not consistent, regarding the effect of temperature so our best guess is that the latter effect is more a finite volume artifact than a physical effect. We also can not exclude the effect of discretization, although in low momenta it might be less determining. The same also applies again to the not-shown hard modes, which can be described approximately as for the gluonic hard modes.

---

[4] The statistical not significant oscillatory behavior at $T = 0.1T_c$ is an artifact of using a point-source for inversion, and would vanish with increasing statistics [27].

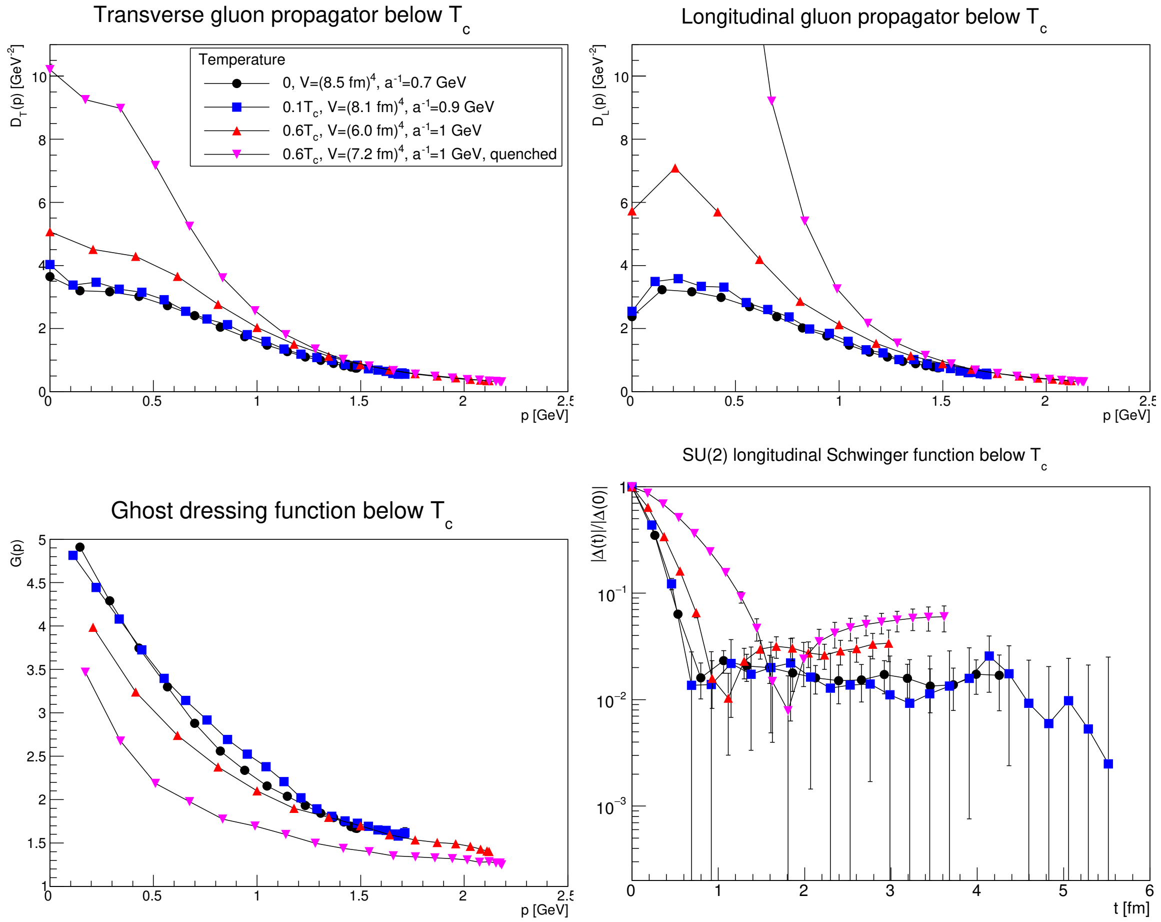

Figure 4.4: The soft mode of the magnetic gluon propagator (top-left panel), the soft mode of the electric gluon propagator (top-right panel), the ghost dressing function (lower-left panel), and the Schwinger function of the electric gluon (lower-right panel) at finite temperature. Quenched results are from [9]. Results have not been renormalized and momenta are all along a spatial edge of the lattice. Momenta for propagators here and hereafter are along an edge to reduce lattice artifacts at small momenta.

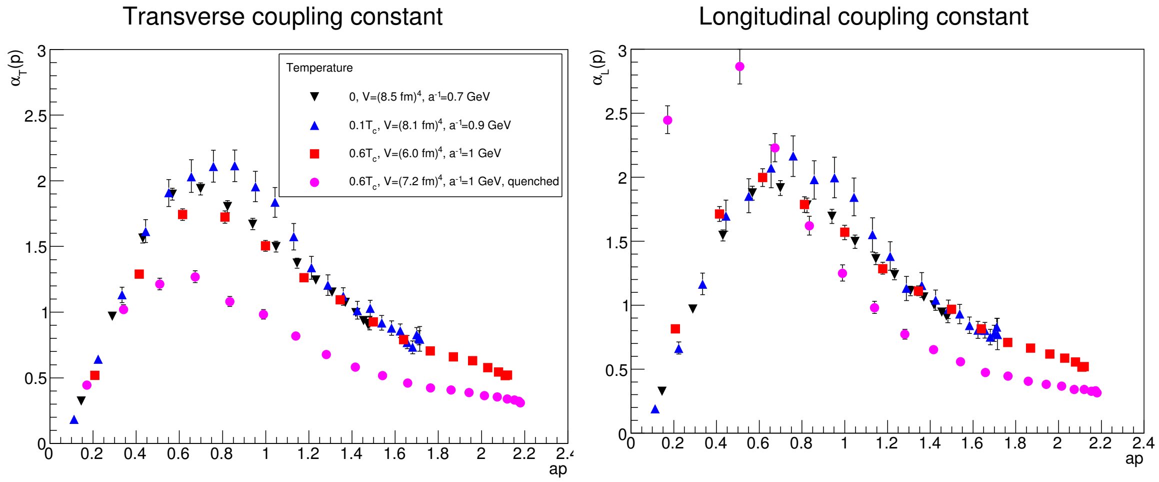

Figure 4.5: The transverse (left panel) and longitudinal (right panel) running coupling at finite temperature. Quenched results are from [9]. All along a spatial edge of the lattice. Note that the lowest momentum point of the longitudinal coupling in the quenched case is likely strongly affected by finite-volume and discretization effects [74, 9].

As noted in equations (4.10) and (4.11) the running coupling also splits into a magnetic and an electric one. The results are shown in Figure 4.5. The main signal is that in the unquenched regime the running coupling is almost independent of the temperature, at least below T_c. For the magnetic coupling, a trend is seen around the maximum but it is not systematic thus may be an artifact. Another observation is the enhancement of the unquenched transverse sector with respect to the quenched results starting from medium momenta, while both sectors are identical at low momenta. The latter can be understood due to the enhancement of the transverse gluon propagator and the screened ghost propagator (that contributes quadratically) at low momenta. So that the ghost and the gluon cancel each others effect. The decrease of the gluon propagator and the quadratic contribution of the ghost propagator favor the screening of the coupling in the quenched case, long before the UV region. Since the running coupling is a derived quantity, these may be lattice artifacts as well as the effects seen previously in the propagators.

The results for the soft magnetic ghost-gluon vertex are shown in Figure 4.6. They show essentially no temperature-dependence, as in the quenched case [55]. The only visible effect seems to be at vanishing gluon momentum, and then again in the same way as for the quenched case. However, this may actually be a finite-volume effect [54], and should therefore not be overrated. Thus, also at (low) finite temperature in the unquenched case this vertex is almost tree-level.

Because of the much larger statistical noise for the three-gluon vertex [27] its results, shown in Figure 4.7, are much less conclusive. The only available data with reasonable statistical errors is at $0.6T_c$ that is in line with the quenched data at $0.7T_c$. Thus we may carry over the independence of three-gluon vertex from the dynamical quarks, seen in Figure 4.3 to the finite temperature regime. We may as well conclude that the three-gluon vertex is almost temperature independent, at least for $T < T_c$.

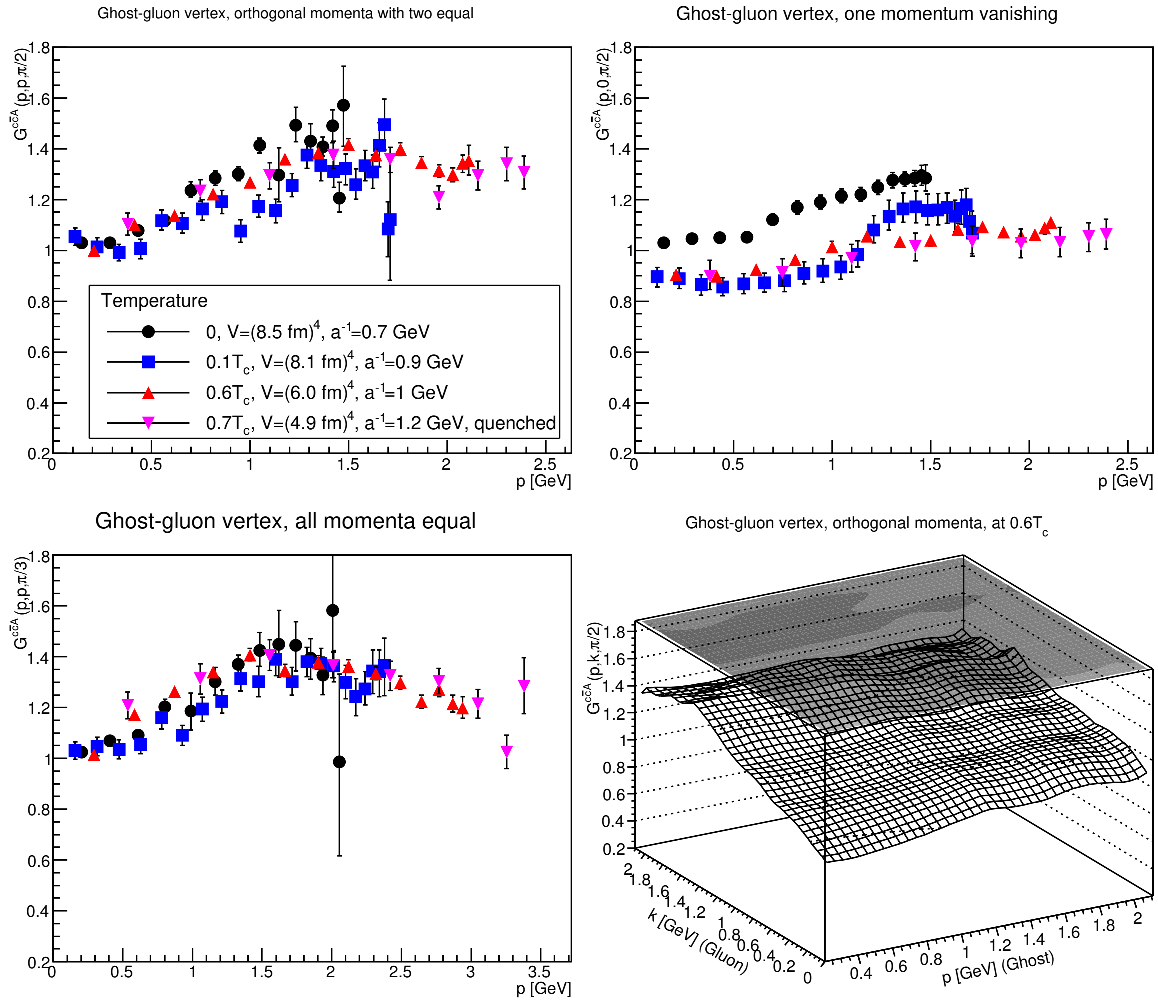

Figure 4.6: The ghost-gluon vertex dressing for different momentum configurations at finite temperature in comparison to quenched data from [55]. See text for details. Results have not been renormalized.

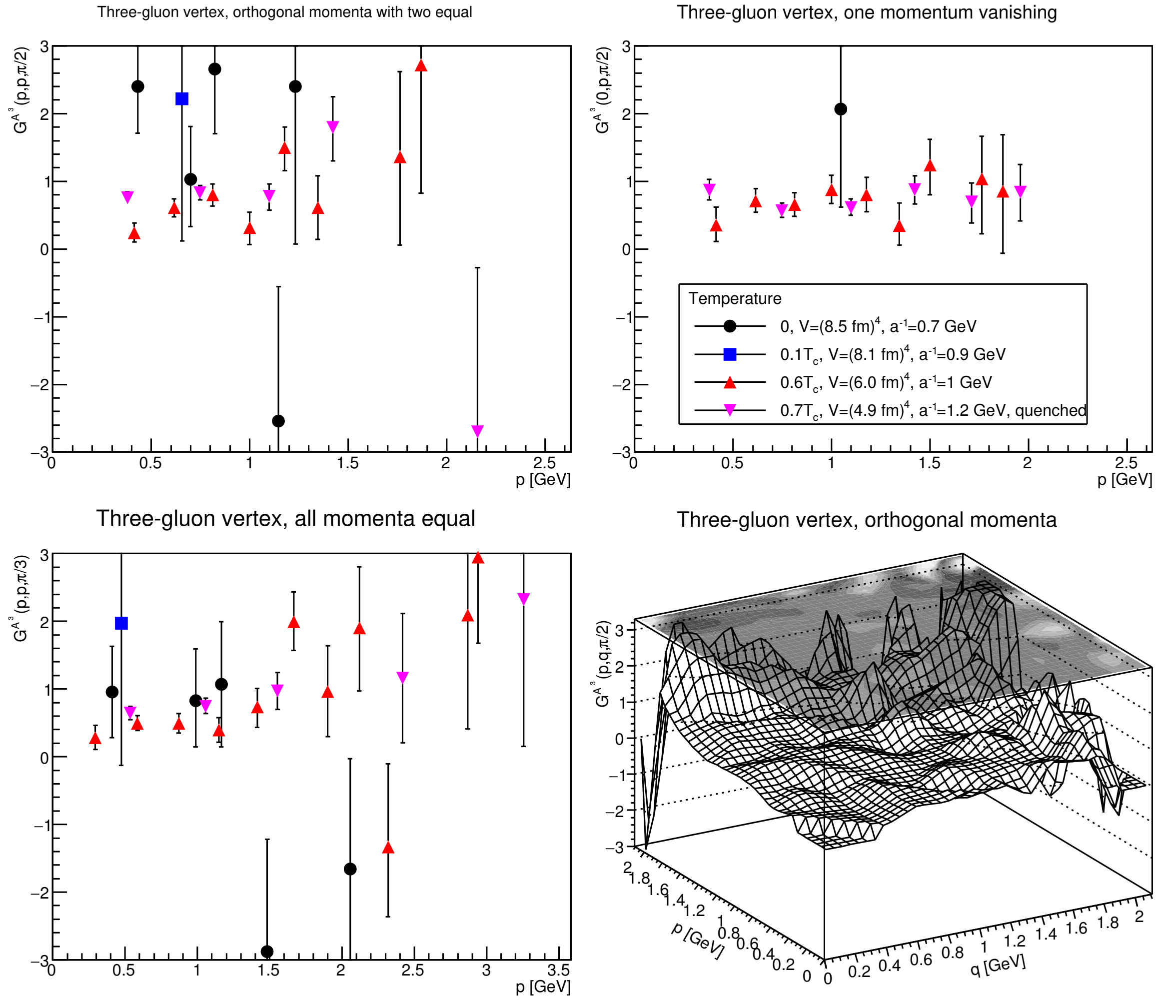

Figure 4.7: The three-gluon vertex dressing for different momentum configurations at finite temperature in comparison to quenched data from [55]. See text for details. Results have not been renormalized.

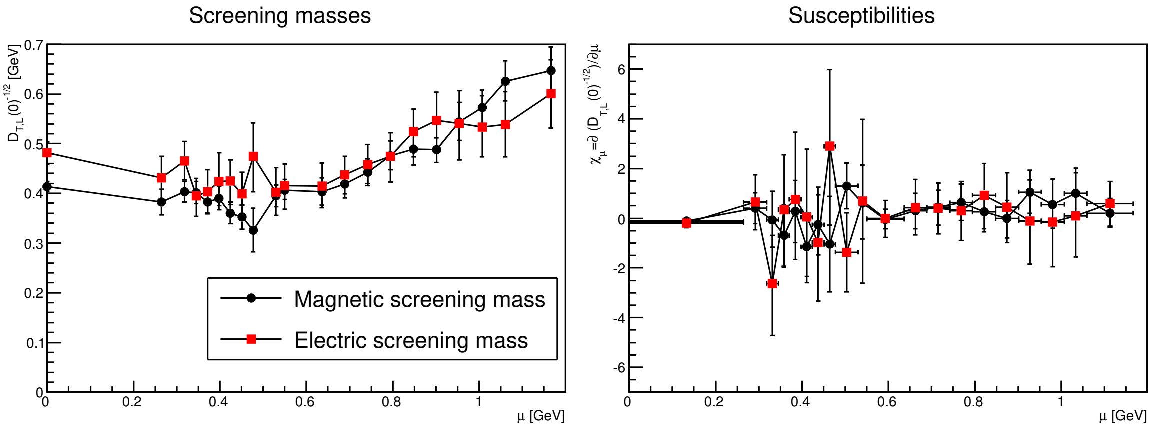

Figure 4.8: The dependence of the screening masses (left panel) and susceptibilities (right panel) with density at fixed volume 24×12^3.

4.5 Finite density results

In the present section, we discuss our finite density results which are the main results of this project.

We know that the screening mass by definition, encodes the far IR behavior of the gluon propagator. In the low momenta regime, $p \ll T$ and/or $p \ll \mu$, the effect of finite temperature and density is most pronounced. On the other hand from Yang-Mills theories, we know that the screening mass behavior is indicative of the phase transition and its type. Thus a natural starting point to study the effect of a possible phase transition would be investigating the behavior of the screening mass with the increase in the chemical potential. Our study, presented in Figure 4.8, in accordance with previous investigations [34, 16], shows no pronounced change, except for a slow increase after the supposed phase transition (or crossover) at $\mu \approx 750$ MeV [34, 16]. Also, no abrupt change is seen at the Silver-Blaze point at about $\mu \approx 375$ MeV, which signals the fact, that the density dependence of the matter sector is not reflected by the gauge sector. The weak response to the supposed to be phase transition is in marked contrast to the finite-temperature transition [9], where in particular in the high-temperature phase, the magnetic and the electric screening mass differed substantially, and at least the electric one strongly depends on the temperature. This is especially interesting as the Polyakov loop shows the same behavior in the high-temperature/density region [34]. Thus, the gluodynamics, as represented by both the Polyakov loop and the gluon propagator, acts quite different. This should actually not come as a surprise. After all the Polyakov loop is sensitive to the group structure of the links, while the gluon propagator in Landau gauge is sensitive to the algebra. They can therefore, in principle, differ in behavior. This seems to be the case at finite density, though not at finite temperature Yang-Mills theory.

The same pattern is repeated in the full momentum dependency shown in Figure 4.9. Except for the dip in the magnetic screening mass around $\mu \approx 450$ MeV, which creates an infrared enhancement for the magnetic propagator, the only observable trend is a continuing suppression above $\mu \approx 750$ MeV. Note that for larger volumes in Figure 4.10, see appendix 4.7, no trend towards such a dip is observed, though this may be also an artifact of the limited statistics. This is also emphasized on the larger volume, where the evolution is smoother. It also shows much better the fact that the gluon propagator above and below the transition at $\mu \approx 750$ MeV shows distinct

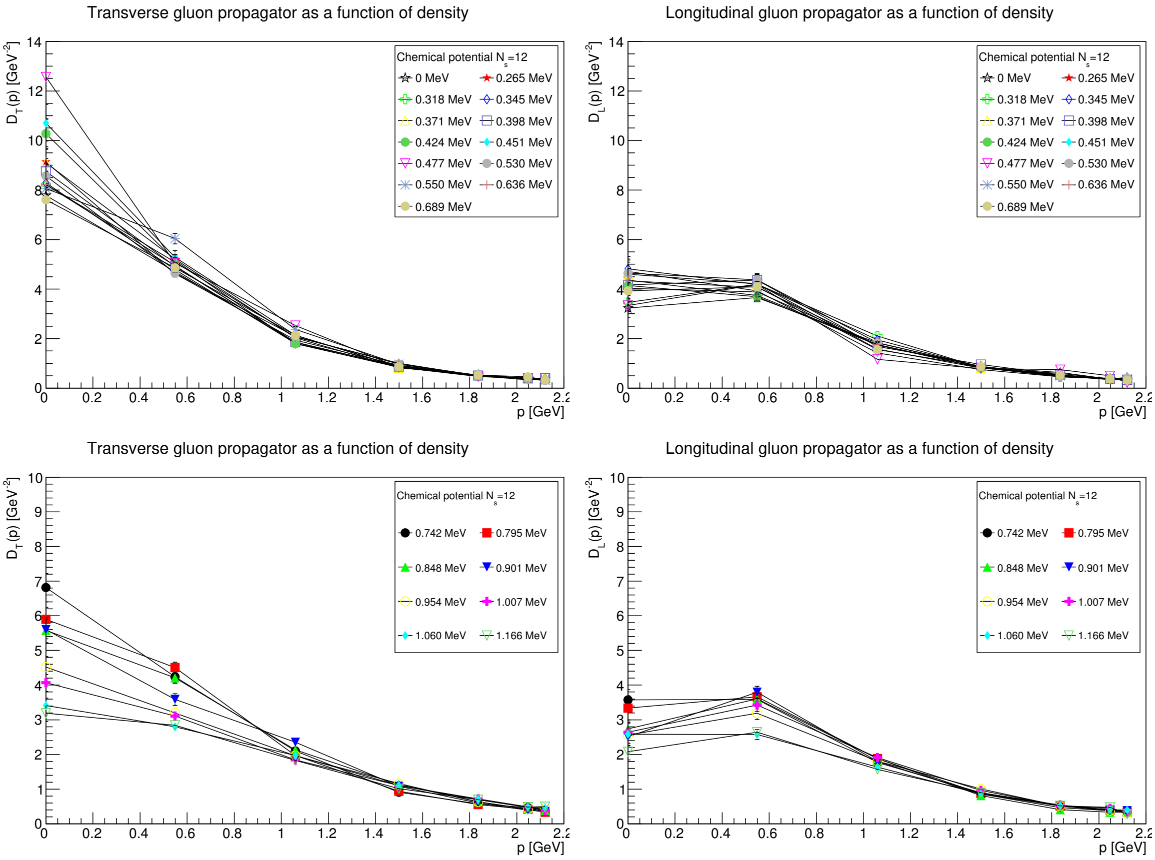

Figure 4.9: The dependence of the transverse (left panels) and longitudinal (right panels) gluon propagator on the chemical potential for $\mu < \mu_c$ (top panels) and $\mu > \mu_c$ (bottom panels).

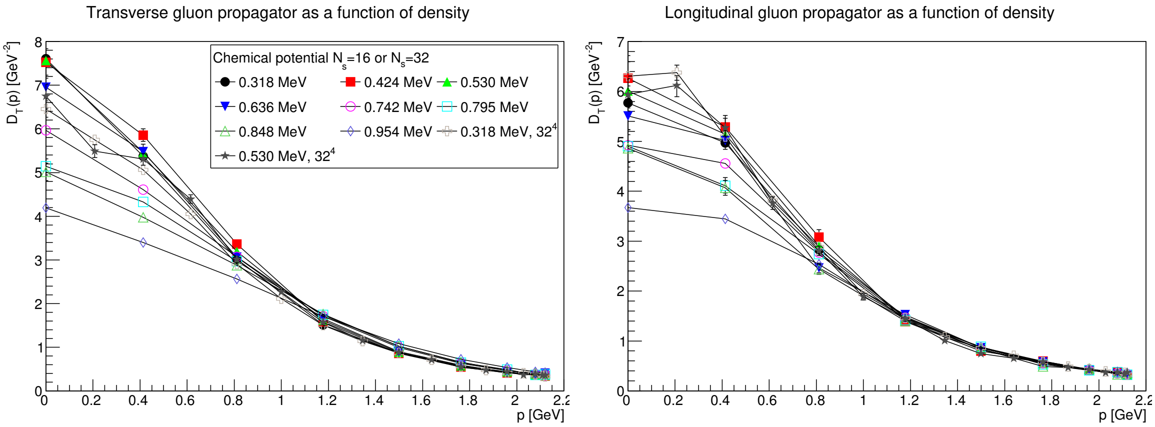

Figure 4.10: The dependence of the transverse (left panels) and longitudinal (right panels) gluon propagator on the chemical potential at fixed volume 24×16^3 or 32^4

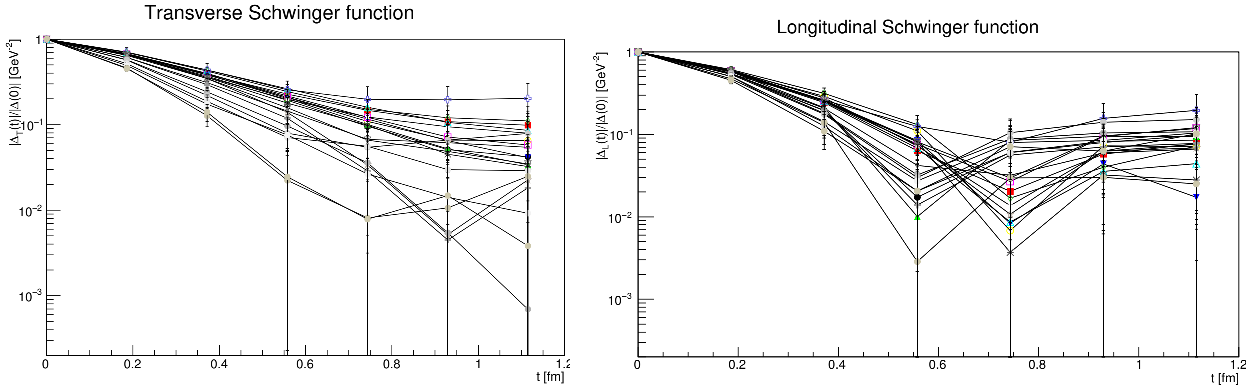

Figure 4.11: The dependence of the transverse (left panel) and longitudinal (left panel) Schwinger function on the chemical potential at fixed volume 24×12^3

difference in the suppression at low momenta. But again, there is no sharp difference in the transverse and longitudinal sector, apart from the stronger sensitivity of the transverse propagator to the chemical potential for $\mu > \mu_c$in the IR region compared to the longitudinal one.

Also due to the limited statistics, it is only possible to state that the Schwinger function in Figure 4.11 does not substantially change before the zero crossing, which appears to remain at all densities, and at about the same time scale of 1 fm.

Ghost dressing function also does not show any significant effect of the chemical potential. Although a weak enhancement is seen in the lowest momenta for the higher chemical potentials, $\mu \approx 900$ MeV, in Figure 4.12 (upper panel), it does not persist on the higher available momenta for 24×12 lattice. However it persists in the larger volume (lower panel) for almost all densities and available momenta. Weather or not it is a genuine IR physical effect, much higher statistics and monitoring more chemical potentials in IR as well as applying different lattice setups will be needed to establish it. Because it is seen not for every step in the increasing of μ but for each few steps (in the larger volume case) and is seen at very high densities in the smaller volume, where lattice artifacts are stronger. For larger momenta, even this weak effects vanishes.

Running coupling hardly shows any chemical potential dependence in Figure 4.13. This can be due to the interplay of the effects in gluon propagator and ghost propagator. More specifically, due to the quadratic contribution of the less affected component, namely the ghost propagator that washes out the effects of the gluon propagator. The present result does not favor any density dependence scenario for the running coupling. The error bars are too large to allow for any stronger statement.

Thus we may infer that running coupling derived from the ghost and gluon propagators is almost unaffected by the density, esp. in the momentum region of our interest. The gauge sector at finite density appears to be largely inert. This will also be confirmed below for the interaction vertices.

Especially, this also implies that approximations using a vacuum gauge sector and contain all density-dependence in the quark sector alone, like [41, 42, 43, 44], are probably much better than should naively be expected. This would simplify calculations in other non-perturbative methods, like functional methods, substantially. Of course, whether this carries over to full QCD is

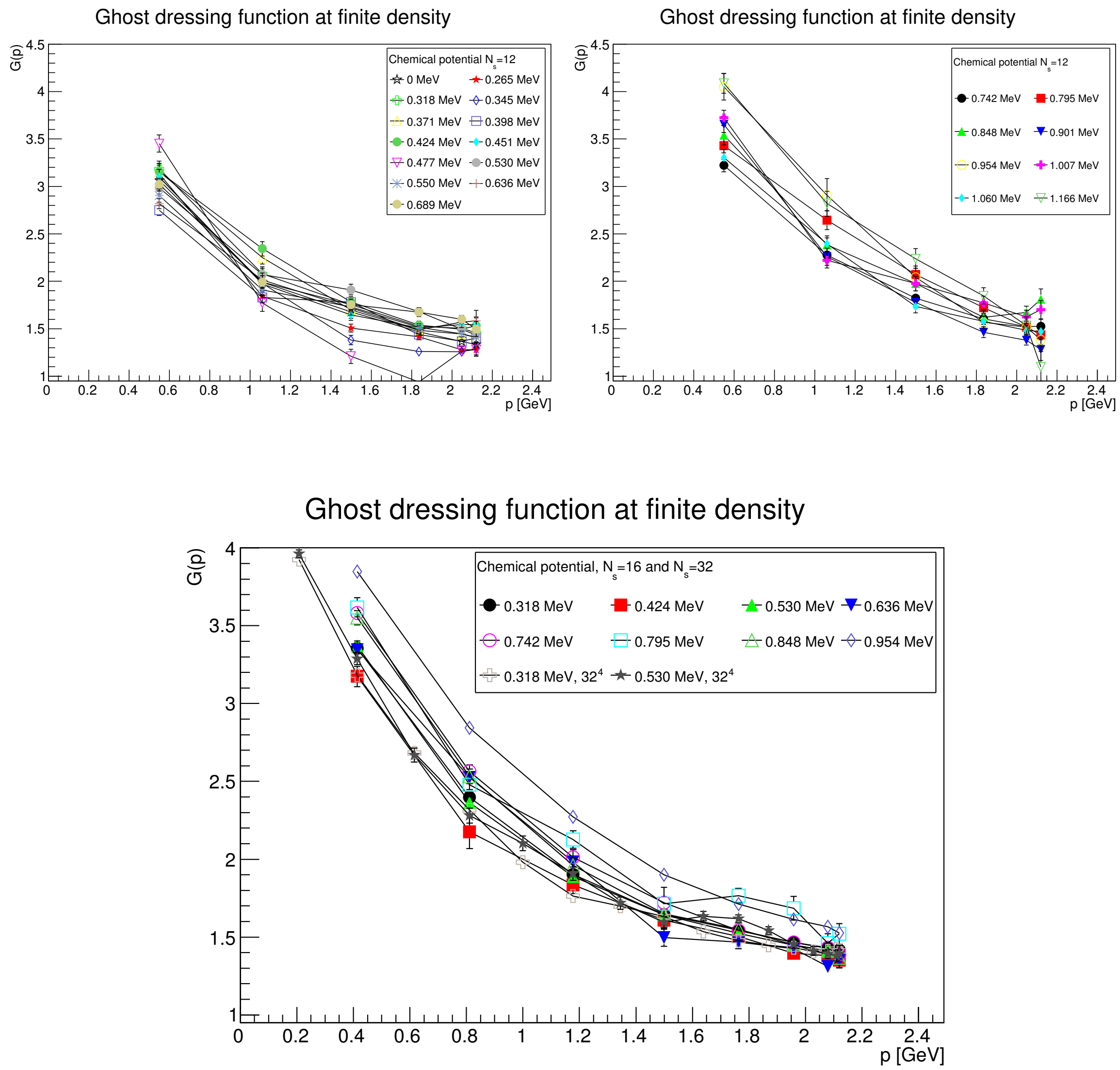

Figure 4.12: The dependence of the ghost dressing function on the chemical potential at fixed volume 24×12^3, $\mu < \mu_c$ (left panel), $\mu \geq \mu_c$ (right panel) and 24×16^3 or 32^4 (lower panel).

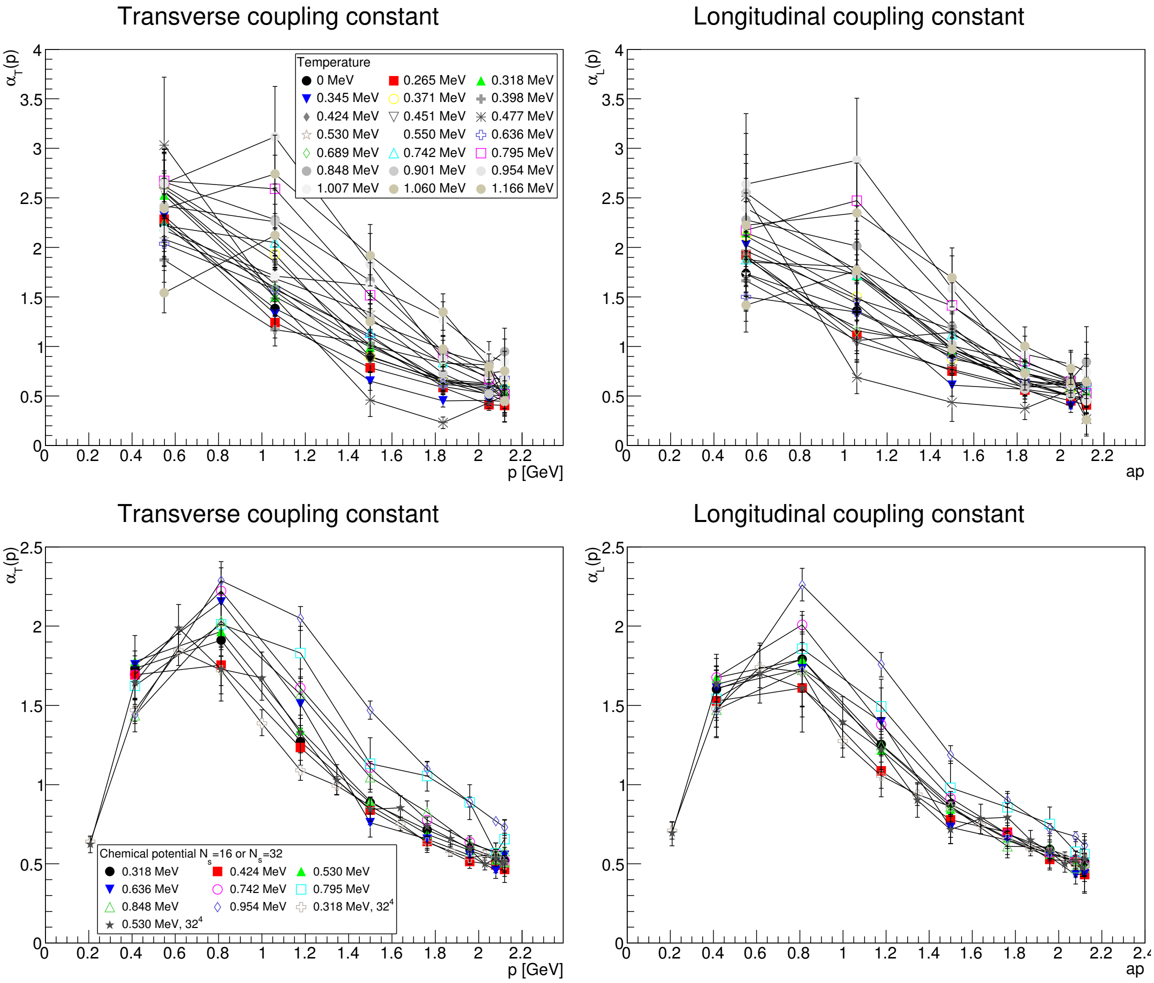

Figure 4.13: The dependence of the transverse (left panels) and longitudinal (right panels) running coupling on the chemical potential at fixed volume 24×12^3 (top panels) and 24×16^3 (bottom panels).

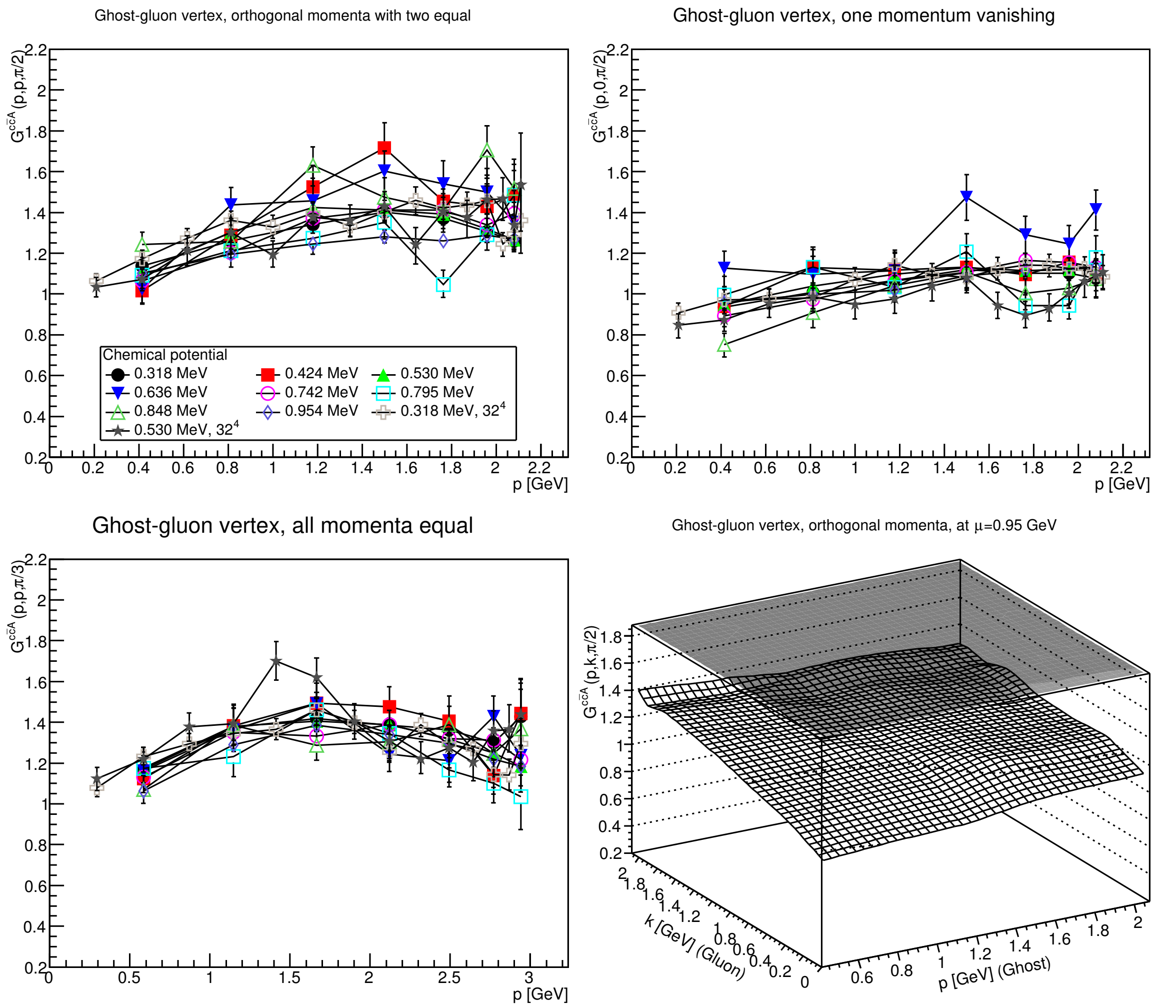

Figure 4.14: The ghost-gluon vertex dressing for different momentum configurations at finite density in different momentum configurations for spatial size $N_s = 16$ and $N_s = 32$. The bottom-right panel is at the largest chemical potential of 954 MeV.

an assumption so far. A test with other models, like G_2-QCD [78], which shows a much more complicated pattern at finite density [21], will be an important cross check.

The results for the ghost-gluon vertex for the larger volume is shown in Figure 4.14. On the smaller volume, which is denser in the chemical potential, the fluctuations are substantially larger. These obscure that there is no statistically significant dependency on the density, as is visible for the larger volume. This is in line with the observations on the running coupling above which, after all, is derived from this vertex.

The results for the soft, magnetic three-gluon vertex are finally shown in Figure 4.15. Within errors, no change with chemical potential is seen, including at the transition point. This is in marked contrast to the situation at finite temperature [55], where the same quantity shows a substantial dependency on the temperature around the transition temperature. This behavior of the magnetic vertex could not have been inferred from the behavior of the gluon propagator at finite density. Since after all, also at finite temperature the magnetic gluon propagator shows (almost) no dependence on the temperature, while the magnetic vertex does.

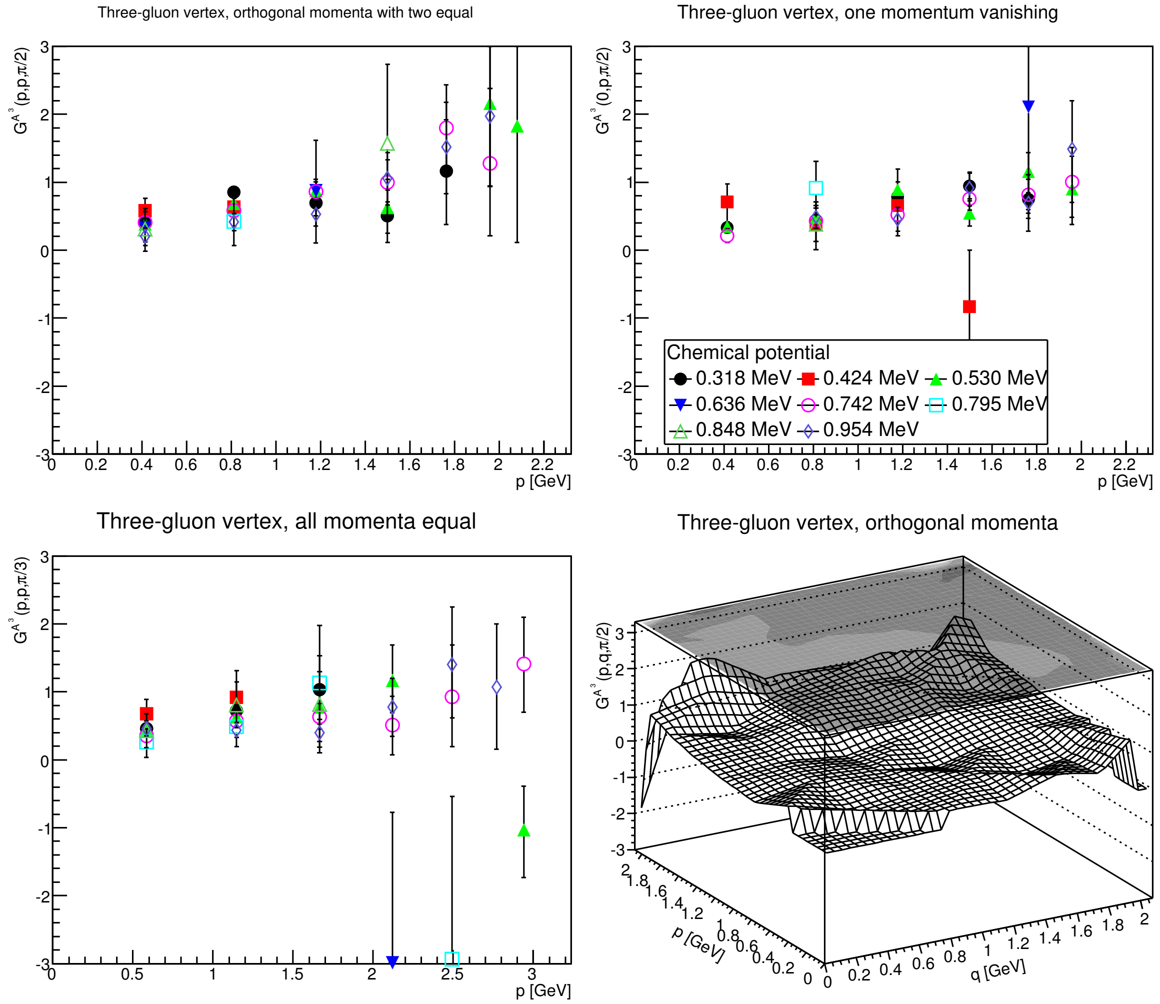

Figure 4.15: The three-gluon vertex dressing for different momentum configurations at finite density in different momentum configurations for spatial size $N_s = 16$. Only points with a relative error less than 100% are displayed. The bottom-right panel is at the largest chemical potential of 954 MeV.

4.6 Conclusions

Summarizing, we have studied the behavior of the gauge sector in two-color QCD both in the vacuum and in the phase diagram. At zero chemical potential the behavior is as expected from corresponding results for three-color QCD as well as Yang-Mills theory. At finite chemical potential no statistical significant change is seen as compared to the vacuum, except a slight increase in screening in both magnetic and electric gluon propagators. Thus, the gauge sector is essentially inert, even across the observed phase change. This is also in marked contrast to quark sector observables, like the Wilson loop and the Polyakov loop, which show different behavior below and above this transition [34, 16]. This suggests that approximation schemes which assume such a behavior [41, 42, 43, 44] are probably much better than expected.

Of course, this will only be useful if this would extend to three-color QCD. There are two possible approaches to do so. One would be to consider more theories, which are accessible at finite density in lattice calculations. Especially G_2-QCD, which shows a substantially more involved phase structure at zero temperature [21], would be a candidate. The other one would be to work with this assumption in other methods, and eventually push them to calculate observable quantities, e. g. neutron star properties. If they would provide reasonable accuracy in their description, this would provide an independent check of the inertness of the gauge sector, at least at intermediate densities.

4.7 Systematic errors

There are several sources of systematic errors in our lattice calculations. Besides the usual vacuum source of finite volume and finite lattice spacing, thermodynamics introduces in addition the finite aspect ratio [9]. In addition, in the investigated system an explicit diquark source j was introduced to induce diquark condensation [34, 16]. The actual desired results would be obtained in the limit of $j \to 0$. As is visible from the available lattice settings of table 4.1, we are only able to study the dependence on j as well as a mixed dependency on the spatial volume and the aspect ratio. Because all our finite density results are at fixed β, we are not able to make a statement about discretization error.

It is, however, noteworthy that both kinds of systematic errors are quite different. The volume (aspect-ratio) error is a genuine consequence of having a finite lattice. A finite diquark source, however, is a physical disturbance of the system, and can equally well be applied to the continuum theory. Thus, by investigating both effects we probe two very different systematic influences.

As is seen in Section 4.5, essentially the only quantity substantially influenced by the density are the screening masses. We will therefore concentrate here on the effects of these two systematic error sources on this quantity. However, we have, in detail, also investigated the impact on all other quantities, and did not find any cases in which stronger effects are present than the one in the screening masses.

The dependence of the screening masses on the diquark source as a function of chemical potential is shown in Figure 4.16. There is no statistically significant dependency on the diquark

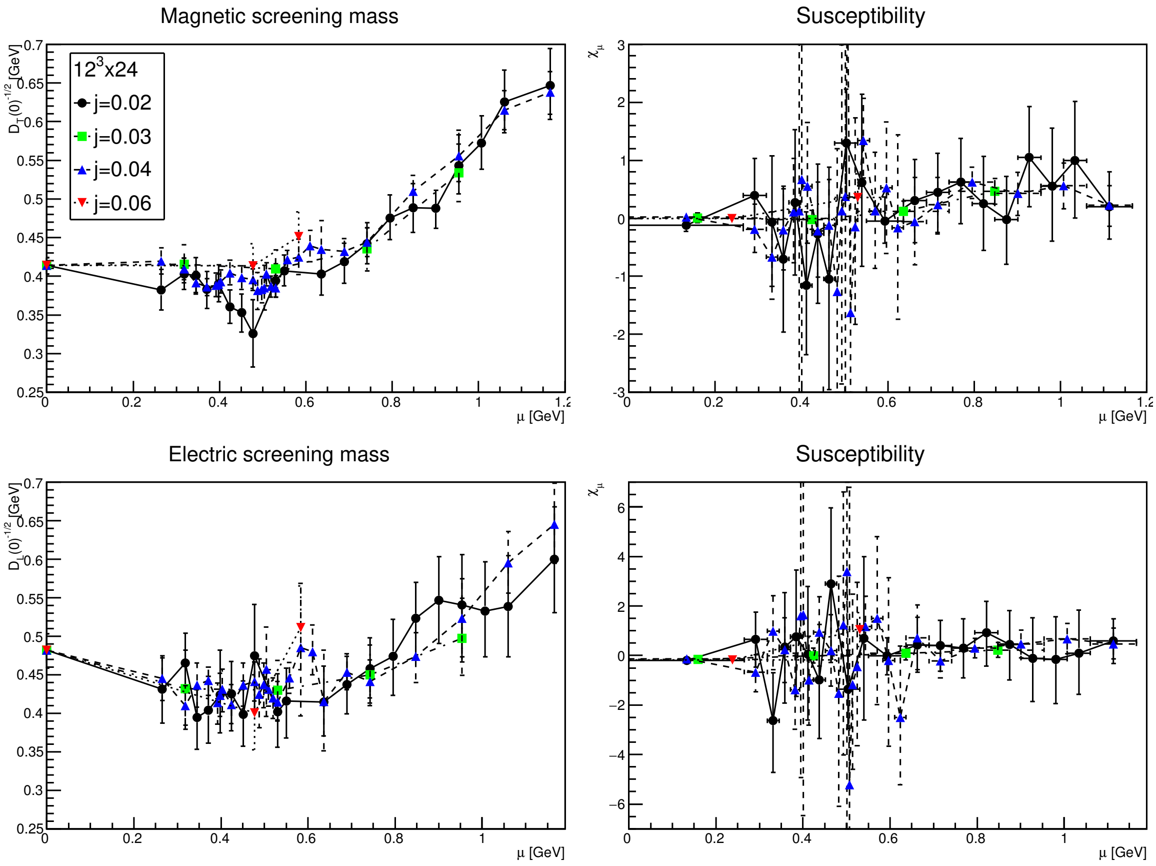

Figure 4.16: The dependence of the magnetic (top panels) and electric (bottom panels) screening masses (left panels) and susceptibility (right panels) on the diquark sources at fixed volume.

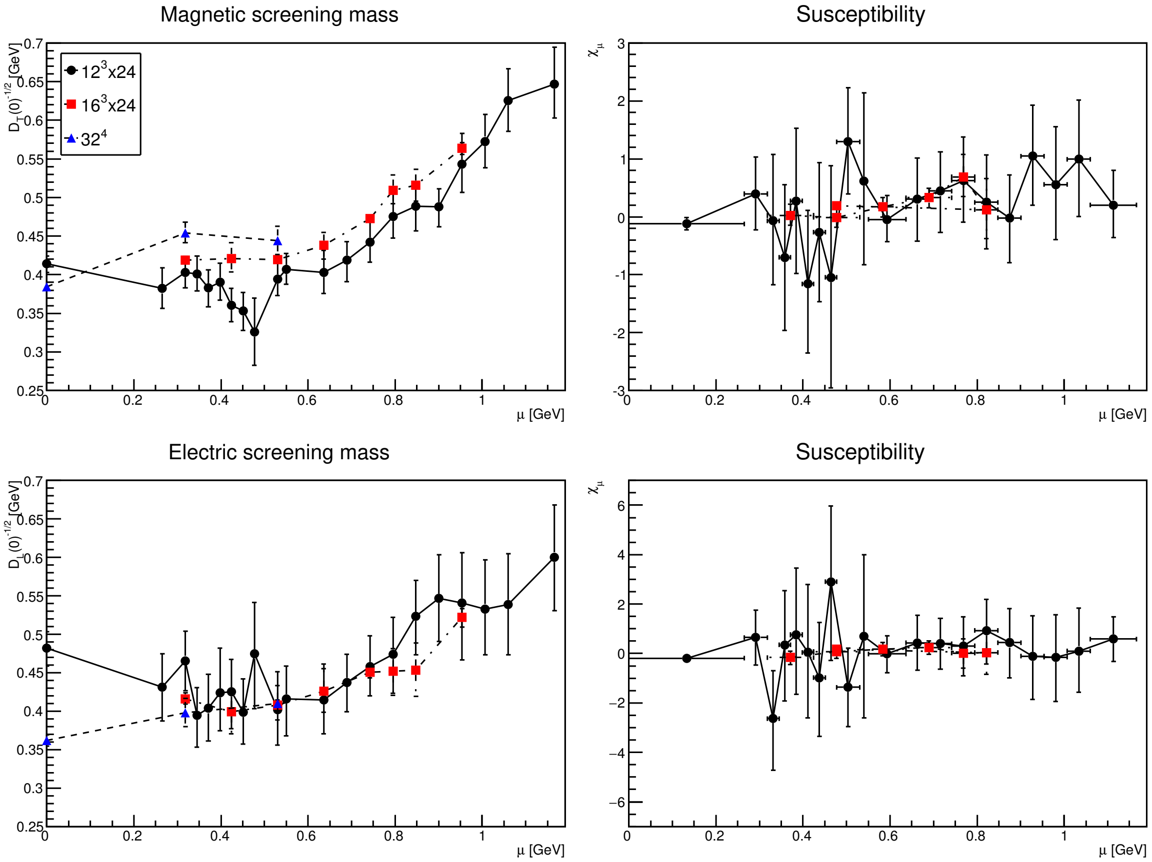

Figure 4.17: The dependence of the magnetic (top panels) and electric (bottom panels) screening masses (left panels) and susceptibility (right panels) on the physical volume and aspect ratio.

source visible at any chemical potential, nor is there a difference between the magnetic and electric screening masses. Thus, within the available statistical accuracy there is no effect, and thus any extrapolation to zero diquark sources [34, 16] is not meaningful for the investigated observables. Thus, the dependency on the diquark source is neglected throughout.

The situation is somewhat different when it comes to finite-volume and aspect-ratio effects, as shown in Figure 4.17. In the magnetic case a slight, but significant, dependence is seen, especially when it comes to the, almost ten times larger, largest volume. In the electric case, no such effect is seen once at finite density. Still, within errors no qualitative effect is seen even in the magnetic case, and even the quantitative effect is only moderate. Still, this suggests to investigate the volume dependence closer in the main text.

Chapter 5

Yang-Mills equation of state from the gluon propagator

5.1 Motivation

A full understanding of the QCD phase diagram involves non-perturbative calculations of the QCD n-points functions. As it has already been discussed, among all, the gluon propagator is of essential importance and various non-perturbative methods have been employed to calculate it. First principle calculations like, functional and lattice methods are the most reliable but at the same time computationally most demanding ones and they both suffer from different artifacts, as mentioned before. In the present chapter we are going to propose a different non-perturbative method to calculate gluon propagator and using the propagator as an input to obtain the equation of state of Yang-Mills theories. This proposal is inspired by an analogy between a theory developed in the context of condensed matter physics, to be discussed in the next section and one loop calculation of a propagator for a finite temperature field theory.[1] As we will see, this analogy would suggest a specific ansatz for the gluon propagator that can absorb the non-perturbative contribution of hard modes ($p \gg T$), into a single parameter called "contact parameter". In order to verify the viability of this ansatz, we use it as a fit function to several lattice setups of $SU(2)$ Yang-Mills at finite temperature. In the fitting procedure we can calculate the fit parameter and then given the effective form of the gluon propagator we calculate the pressure in terms of the so called contact parameter. This possibility is a remarkable aspect of the fit ansatz, that makes the pressure integral finite so that it does not suffer from UV divergencies. We will see this explicitly in Section 5.5.

5.2 Condensed matter theory of short range interactions

In this section, we introduce the formalism of the contact interaction, also known as pseudo-potential. We briefly rehearse the important concepts, like the scattering length and the relative

---

[1] This analogy has been established in a more rigorous way, applying functional renormalization group in [79].

wave function in this context. The physical motivation is to understand a dilute interacting system at low temperature, so that the average inter-particle distance $v^{1/3}(v = \frac{V}{N})$ and the thermal wavelength λ are much larger than the range of the interaction r_0. Thus the effective interaction experienced by a particle is small, even though the inter-particle potential may have large values. At low energies the details of the potential do not play an important role in the scattering process and the dynamism can be explained only by a single parameter of the potential- scattering length a- that is roughly the effective diameter of the potential. The method of pseudo-potential tries to simulate the above explained system. A natural starting point is the two-body problem in a hard-sphere potential with diameter a. The two-body wave function is given by

$$\Psi(\mathbf{r_1}, \mathbf{r_2}) = e^{i\mathbf{P}\cdot\mathbf{R}}\psi(\mathbf{r}). \tag{5.1}$$

Where $\psi(\mathbf{r})$ is the relative wave function. $\mathbf{R}$ is the center of mass, and $\mathbf{r}$ is the distance between the two particles. The Schrödinger equation in the c.o.m of the system is

$$(\nabla^2 + k^2)\psi(\mathbf{r}) = 0 \;\; (r > a) \tag{5.2}$$

$$\psi(\mathbf{r}) = 0 \;\; (r \le a), \tag{5.3}$$

where k is the relative wave number $k \sim \frac{1}{r}$. Since the system is dilute, k is small. At low energies the details of the potential can not be resolved, so we may only study (S-wave) spherical symmetric solutions of the above equation. For $(k \to 0)$ the solution is

$$\psi(r) = \alpha(\frac{1}{a} - \frac{1}{r}) \;\; (r > a), \tag{5.4}$$

$$\psi(r) = 0 \;\; (r \le a). \tag{5.5}$$

Now we want to find the equivalent hard core potential for the short range interaction, that we discussed previously. Namely, to find a potential such that its solution for $r \to 0$ is (5.4). The corresponding Schrödinger equation is (5.2) but for all $r \neq 0$ which means, the range of interaction compared to all the other length scales is close to zero. The generalized wave function $\tilde{\psi}(r)$ which is the solution of (5.2) for $r \neq 0$, must satisfy the boundary condition

$$\tilde{\psi}(a) = 0, \tag{5.6}$$

in order to find the equivalent pseudopotential. Since the microscopic interaction is short range, we demand the following low energy $(k \to 0)$ behavior for $r \to 0$,

$$\tilde{\psi}(r) \to (\frac{1}{a} - \frac{1}{r})\chi. \tag{5.7}$$

In the above equation χ is a constant, given by the boundary condition at $r \to \infty$, which reads

$$\chi = \frac{\partial}{\partial r}(r\tilde{\psi}(r)). \tag{5.8}$$

The short range interaction is zero everywhere but at $r = 0$, thus in order to have a nontrivial effect over a finite region, it must be infinite at $r = 0$. This suggests the following generalization of (5.2) for this interaction, satisfying (5.6)

$$(\nabla^2 + k^2)\tilde{\psi}(r) = 4\pi a \delta(\mathbf{r}) \frac{\partial}{\partial r}(r\tilde{\psi}(r)). \tag{5.9}$$

We can also understand the above formula in analogy to the Gauss's law in electrostatic for the point charge, demanding the short range behavior of the relative wave function as $\tilde{\psi}(r)$ in (5.7). The operator $\delta(\mathbf{r})\frac{\partial}{\partial r}r$ is called the pseudopotential, and in the following we are going to study its properties under integration for the regimes of finite and infinite momenta, we follow the argument presented in [80]. To do so, we need to study the Fourier transform of (5.9) and therefore we define the operator $\Lambda(\mathbf{k})$, as follows

$$\delta(\mathbf{r})\frac{\partial}{\partial r}(re^{i\mathbf{k}.\mathbf{r}}) \equiv \delta(\mathbf{r})\Lambda(\mathbf{k}). \tag{5.10}$$

By integrating over r on both sides of (5.10) for finite momenta, we have

$$\Lambda(\mathbf{k}) = 1\,(k < \infty). \tag{5.11}$$

To include the effect of $k \sim \infty$, we multiply both sides of (5.10) by $\frac{1}{k^2}$ and integrate over $\mathbf{k}$, which gives

$$\int d^3k \frac{\Lambda(\mathbf{k})}{k^2} = 0. \tag{5.12}$$

Clearly, if (5.11) were true for the whole real line then the above integral could not converge. Therefore the dominant contribution in the above result comes from $\Lambda(\mathbf{k})_{k\sim\infty}$, that is why we may call $\Lambda(\mathbf{k})$, *filter* of the high energy modes. It is transparent for the finite k ($\Lambda(\mathbf{k}) = 1$) and kills the diverging modes in (5.12). We may as well define a complementary operator $L(\mathbf{k})$ as follows

$$L(\mathbf{k}) = 0\,(k < \infty), \quad \int \frac{d^3k}{2\pi^3}\frac{L(\mathbf{k})}{k^2} = 1. \tag{5.13}$$

It kills finite momentum modes and regularizes high momenta contribution. The operator $\eta(\mathbf{k})$ takes both finite and infinite momenta contributions into the account by combining $\Lambda(\mathbf{k})$ and $L(\mathbf{k})$ in the following relation

$$\eta(\mathbf{k}) \equiv \Lambda(\mathbf{k}) + \frac{L(\mathbf{k})}{4\pi a}, \tag{5.14}$$

that shows $\eta(\mathbf{k})$ satisfies

$$\eta(\mathbf{k}) = 1\,(k < \infty), \quad \int \frac{\eta(\mathbf{k})d^3k}{k^2} = \frac{1}{4\pi a}. \tag{5.15}$$

The Fourier transformed operator $\tilde{\eta}(\mathbf{r})$ defined as follows

$$\tilde{\eta}(\mathbf{r}) = \int \frac{d^3k}{(2\pi)^3}\eta(\mathbf{k})e^{i\mathbf{k}.\mathbf{r}}, \tag{5.16}$$

acts like the delta function for a well-behaved function $f(\mathbf{r})$, but it annihilates short range contributions to the wave function,

$$\int d^3r\tilde{\eta}(\mathbf{r})f(\mathbf{r}) = f(0) \tag{5.17}$$

$$\int d^3r\tilde{\eta}(\mathbf{r})[\frac{1}{r} - \frac{1}{a}] = 0, \int d^3r\tilde{\eta}(\mathbf{r})\hat{\mathbf{r}} = 0. \tag{5.18}$$

From (5.15) we have

$$\int \frac{d^3k}{(2\pi)^3}\eta(\mathbf{k})f(\mathbf{k}) = \frac{c}{4\pi a} + \lim_{K\to\infty}\int_{|\mathbf{k}|<K} \frac{d^3k}{(2\pi)^3}[f(\mathbf{k}) - \frac{c}{k^2}]. \tag{5.19}$$

The above relation, shows that $\eta(\mathbf{k})$ singles out the $k \sim \infty$ contribution in the integral, and encodes it in two parameters, the "cut off" a, which is the same as the scattering length and contact parameter $c = \lim_{|\mathbf{k}|\to\infty} k^2 f(\mathbf{k})$. In the following, we are going to apply the introduced formalism to the energy of a many-body fermionic system with short range interaction, given by

$$E = \frac{-\sigma}{2m}\lim_{\epsilon\to 0}\int_{D(\epsilon)} d^{3N+3M}R\phi^*(\mathbf{R})\nabla^2\phi(\mathbf{R}). \tag{5.20}$$

$$\sigma\int d^{3N+3M}R\phi^*(\mathbf{R})\phi(\mathbf{R}) = 1 \tag{5.21}$$

The above relation indicates the operator of the kinetic energy as the energy operator of the system, which is justified as long as the distance between each two fermions with opposite spin is nonzero $(r > \epsilon)$. The region of the configuration space that this condition is held for, is represented by $D(\epsilon)$. The fermions with the same spin are indistinguishable particles, therefore a symmetrization prefactor σ is necessary, however its explicit form is irrelevant for our discussion, we just keep in mind that we have N fermions with the spin up and M fermions with spin down. The effect of the contact interaction is absorbed into the short range behavior of the many-body wave function $\phi(\mathbf{R})$. Where $\mathbf{R}$, stands for $3N + 3M$ dimensional configuration space of $N + M$ fermions and ∇^2 is $3N + 3M$ dimensional Laplace operator. In the next step, we argue that (5.20) is equal to X, defined as follows

$$X \equiv \frac{-\sigma}{2m}\int_S d^{3N+3M}Rd^3\tilde{\eta}(t)\phi^*(\mathbf{R})\nabla^2_{\mathbf{t}}\zeta(\mathbf{R},\mathbf{t}). \tag{5.22}$$

where $\zeta(\mathbf{R},\mathbf{t})$ is given in the following

$$\begin{aligned} \zeta(\mathbf{R},\mathbf{t}) &= \sum_{i=1}^{i=N}\phi(\mathbf{R}',\mathbf{t}+\mathbf{r_i}) + \sum_{j=1}^{j=M}\phi(\mathbf{R}'',\mathbf{t}+\mathbf{s_j}) \\ \phi(\mathbf{R}',\mathbf{t}+\mathbf{r_i}) &= \phi(\mathbf{r_1},...,\mathbf{r_i}+\mathbf{t},\mathbf{r_N},...,\mathbf{s_1},...,\mathbf{s_i},...,\mathbf{s_M}) \\ \phi(\mathbf{R}'',\mathbf{t}+\mathbf{s_j}) &= \phi(\mathbf{r_1},...,\mathbf{r_i},...,\mathbf{r_N},\mathbf{s_1},...,\mathbf{s_j}+\mathbf{t},...,\mathbf{s_M}) \end{aligned} \tag{5.23}$$

It is an attempt to present the energy of the system in terms of an integral over the whole configuration space, without excluding the interaction region. We will later on use the claimed equality $(E = X)$, to single out the contribution of the contact interaction in the form of (5.19). We decompose the space of integration S as follows,

$$S = D(\epsilon) + I(\epsilon), \;\; X = X_{D(\epsilon)} + X_{I(\epsilon)}. \tag{5.24}$$

First we show $E = X_{D(\epsilon)}$, then for having $(E = X)$, we need to show

$$X_{I(\epsilon)} = 0. \tag{5.25}$$

Since for $\mathbf{R} \in D(\epsilon)$, the relative wave function of a fermionic pair $\psi(r) = (\frac{1}{a} - \frac{1}{r})$ is finite and continuous thus $\tilde{\eta}(\mathbf{t})$ acts as a Dirac delta function. We briefly show that

$$\mathbf{R} \in D(\epsilon) \Longrightarrow X_{D(\epsilon)} = E. \tag{5.26}$$

We rewrite (5.22) in the form of

$$\begin{aligned} X &= \frac{-\sigma}{2m}\Big(\sum_{i=1}^{i=N}\int d^3t\tilde{\eta}(\mathbf{t})I_i + \sum_{j=1}^{j=M}\int d^3t\tilde{\eta}(\mathbf{t})I_j\Big) \\ I_i(\mathbf{t}) &= \int_{D(\epsilon)} d^{(3N+3M)}R\phi^*(\mathbf{R})\nabla^2_{\mathbf{t}}\phi(\mathbf{R}', \mathbf{t}+\mathbf{r_i}), \\ I_j(\mathbf{t}) &= \int_{D(\epsilon)} d^{(3N+3M)}R\phi^*(\mathbf{R})\nabla^2_{\mathbf{t}}\phi(\mathbf{R}'', \mathbf{t}+\mathbf{s_j}). \end{aligned} \tag{5.27}$$

We show that I_i is finite and continuous for $\mathbf{R} \in D(\epsilon)$, and thus $\tilde{\eta}(\mathbf{t})$ acts as a Dirac delta function. In order to show this, we use the following factorization of $\phi(\mathbf{R}', \mathbf{t}+\mathbf{r_i})$ with respect to the relative wave function of the one pair of fermions

$$\phi(\mathbf{R}', \mathbf{t}+\mathbf{r_i}) = \psi(|\mathbf{r}+\mathbf{t}|)A(\mathbf{R}', \mathbf{r_0}) \tag{5.28}$$

$$\psi(r) = (\frac{1}{r} - \frac{1}{a}), \;\; r = |\mathbf{r}_i - \mathbf{s}_i|, \;\; \mathbf{r_0} = \frac{\mathbf{r}_i + \mathbf{s}_i}{2}, \tag{5.29}$$

$$d^{3N+3M}R = d^{3N+3M-6}R\, d^3r_0\, d^3r \tag{5.30}$$

For $r > \epsilon$, $\psi(r)$ and thus $\phi(\mathbf{R}', \mathbf{t}+\mathbf{r_i})$ are finite and infinitely differentiable. The normalization condition (5.21), demands $\phi(\mathbf{R}) \underset{r\to\infty}{\longrightarrow} 0$ together with the fact that ∇^2_t suppresses the integrand of I_i in (5.27) at infinity even more than $\phi(\mathbf{R})$ thus I_i and equivalently I_j are finite. Therefore $\tilde{\eta}(\mathbf{t})$ in the relation for X (5.27) acts as a Dirac delta function and we have

$$\begin{aligned} &\int d^3t\tilde{\eta}(\mathbf{t})I_i(\mathbf{t}) = I_i(0) \\ &= \int_{D(\epsilon)} \phi^*(\mathbf{R})\nabla^2_{\mathbf{r_i}}\phi(\mathbf{R}', \mathbf{r_i}) \end{aligned} \tag{5.31}$$

The same is true for $I_j(t)$. Therefore

$$X_{D(\epsilon)} = \frac{-\sigma}{2m}\Big(\int_{D(\epsilon)} d^{3N+3M}R\phi^*(\mathbf{R})\nabla^2\phi(\mathbf{R})\Big) = E \tag{5.32}$$

In the next step, we show $X_{I(\epsilon)} = 0$. We consider the term $\phi(\mathbf{R}', \mathbf{t} + \mathbf{r_i})$ in (5.23) , and replace $\zeta(\mathbf{R}, \mathbf{t})$ by this term in (5.22). Then we calculate the corresponding integral X_i, which is defined, dropping irrelevant constants, as follows

$$\begin{aligned} X_i &\equiv \int_{I(\epsilon)} d^{3N+3M-6}R' d^3r_0 \int d^3t \tilde{\eta}(t) \nabla^2_{\mathbf{t}} K(\mathbf{R}', \mathbf{r_0}, \mathbf{t}), \\ K(\mathbf{R}', \mathbf{r_0}, \mathbf{t}) &= \int_{r<\epsilon} d^3r \big[A^*(\mathbf{R}', \mathbf{r_0})(1/r - 1/a)\big] \\ &\times \big[A(\mathbf{R}', \mathbf{r_0} + \mathbf{t/2})(1/|\mathbf{r} + \mathbf{t}| - 1/a)\big] \end{aligned} \tag{5.33}$$

where we used the factorization of $\phi(\mathbf{R}', \mathbf{t} + \mathbf{r_i})$ introduced in (5.28) and we dropped terms of $\mathcal{O}(r)$. Since the main contribution comes from $t \ll \epsilon$ given $\epsilon \to 0$, we may expand $K(\mathbf{R}', \mathbf{r_0}, \mathbf{t})$ in powers of t. We may also drop any term, of the order t^3 or higher because of the action of Laplace operator ∇^2_t that leaves us with a positive power of t, which will give zero, under $\tilde{\eta}(t)$ integration. Thus after the expansion we end up with $K(\mathbf{R}', \mathbf{r_0}, \mathbf{t}) \sim c_1(t/2 - t^2/(6a)) + \mathbf{c_2}.\hat{\mathbf{t}}t^2$. Finally we have $\nabla^2_t K \sim c_1(1/t - 1/a) + 4\mathbf{c_2}.\hat{\mathbf{t}}$, which is annihilated by the $\tilde{\eta}(t)$ integration, using (5.17) and (5.18). Thus $X_{I(\epsilon)} = \sum_i X_i = 0$ and $X = E$.

In the second quantization formalism (5.22) can be written as

$$-2mX = \langle \phi | \int d^3r d^3t \tilde{\eta}(\mathbf{t}) \nabla^2_t \psi^\dagger(\mathbf{r}) \psi(\mathbf{r} + \mathbf{t}) | \phi \rangle. \tag{5.34}$$

The Fourier transform of the above equation together with $X = E$, give

$$E = \int \frac{d^3k}{(2\pi)^3} \eta(\mathbf{k})(k^2/2m)n(\mathbf{k}), \;\; n(\mathbf{k}) = \langle \phi | c^\dagger_{\mathbf{k}} c_{\mathbf{k}} | \phi \rangle. \tag{5.35}$$

Using (5.19), we can decompose energy E to the finite and infinite contributions ending up with

$$E = \int \frac{d^3k}{(2\pi)^3} \eta(k) \frac{k^2}{2m} n(k) = \frac{C\Omega}{4\pi a m} + \lim_{K_0 \to \infty} \int_{k<K_0} \frac{d^3k}{(2\pi)^3} \frac{k^2}{2m} [n(k) - \frac{C}{k^4}], \tag{5.36}$$

$$C = \lim_{k \to \infty} k^4 n(k). \tag{5.37}$$

Summarizing the path which led us here, we saw that the energy of the system E is given by the kinetic energy expectation value in a configuration space excluding the sub-space with $r < \epsilon$ in equation (5.20), (r is the distance between two fermions with opposite spins). E can also be written as an integral over the whole space, while $\tilde{\eta}(\mathbf{r})$ annihilates the short range relative wave function. Equivalently $\eta(\mathbf{k})$ in the first term of (5.36) singles out the $k \to \infty$ contribution, reflecting the effect of the contact interaction.

In the next section of this chapter, we are going to establish a connection between this formalism and the non-perturbative calculation of the 2-point functions in the finite temperature field theory.

5.3 2-point functions at finite temperature

In this section we will see first, how we can calculate a typical 2-point function at finite temperature from the partition function and then how this 2-point function is related to the energy of the system. Based on the one loop calculation of the energy and in analogy with the contact interaction formalism, introduced in the previous chapter we speculate on the non-perturbative behavior of the 2-point function at $p \gg T$. This will lead us to an ansatz for the finite temperature gluon propagator, whose viability will be checked in the next section.

$$Z = \int \mathcal{D}[\phi] e^{-\beta \sum_p \phi^*(p) D(p,m_i) \phi(p)} \tag{5.38}$$

$$Z = C(detD)^{-1} \tag{5.39}$$

In the above equations, Z represents the partition sum at finite temperature. $D(p, m_i)$ represents the energy operator and m_i refers to all the relevant scales of the system like the bare mass m, the coupling g, the chemical potential μ and the temperature T. The prefactor C in the last equation is an irrelevant constant for our present formal discussion. The energy of the free and interacting theory are given respectively as follows

$$D_0 = p^2 + m^2 \tag{5.40}$$

$$D = p^2 + m^2 + \Sigma(p, m, T, g, \mu) \tag{5.41}$$

The one loop calculation of this self energy $\Sigma(p, m, T, g, \mu)$ at finite temperature and zero chemical potential, gives

$$\Sigma(p, m, g, T) \sim T \int \frac{q^2}{((p-q)^2 + m_T^2)(q^2 + m_T^2)} dq \tag{5.42}$$

where the thermal mass m_T is a function of all the parameters $m_T = m(m, g, T)$. The above integral is maximum around $q = p$. We expand the integrand around this maximum

$$q' = p - q, \;\; q^2 dq \to p^2 dq' - 2pq' dq' + q'^2 dq' \tag{5.43}$$

$$\Sigma(p, m_T) = \frac{Tp^2}{p^2 + m_T^2} \int \frac{1}{q'^2 + m_T^2} dq' + \frac{T}{(p^2 + m_T^2)} \int \frac{q'^2}{(q'^2 + m_T^2)} dq' \tag{5.44}$$

The first term in the above equation, denoted by Σ_0, is dominated by $q' \sim 0$ and $p \to \infty$. Thus it is important in the perturbative regime and would not play an important role in the analogy to the contact interaction. The second term in Σ, indicated by Σ_1 is dominated by $q' \to \infty$, thus it may reflect the effect of the contact interaction, it is also maximal when $p \to 0$, therefore is relevant in the non-perturbative regime. The argument presented here will be used as a guide to construct an ansatz for the gluon propagator at finite temperature in the next section.

5.4 Fit ansatz

The propagator is given by $G^{-1} = D$. It is then written in terms of a perturbative contribution $G_0^{-1} + \Sigma_0$ and nonperturbative one as follows,

$$G^{-1} = G_0^{-1} + \Sigma = G_0^{-1} + \Sigma_0 + \Sigma_1. \tag{5.45}$$

We already argued that Σ_0 contains perturbative informations, thus we may replace $G_0^{-1} + \Sigma_0$ by the inverse of the perturbative propagator G_0'. We also saw that Σ_1 is dominated by the high energy modes in the loop integral, so that the effect of the short range interaction is encoded in this term. A generalization of this term would be $\frac{C_T}{G_0'}$, where the integral is replaced by C_T, the contact term, to be specified by the fit to the lattice data. The fit-ansatz will be of the form

$$G^{-1} = G_0'^{-1} + C_T G_0'. \tag{5.46}$$

According to [49] G_0' is given by

$$G_0'(p) = \frac{1}{((33\frac{1.8}{52\pi}(\log[\frac{p^2}{4}]) + 1)^{\frac{13}{22}})p^2 + m_T^2}. \tag{5.47}$$

We absorbed the effect of temperature at low energies, into m_T and since we are interested in high energy modes $p \gg T$, we drop this term in the ansatz. The final form of the fit function is

$$G(p) = \frac{1 + \frac{C_T}{16}}{((33\frac{1.8}{52\pi}(\log[\frac{p^2}{4}]) + 1)^{\frac{13}{22}})p^2 + \frac{C_T}{((33\frac{1.8}{52\pi}(\log[\frac{p^2}{4}])+1)^{\frac{13}{22}})p^2}} \tag{5.48}$$

The factor $(1 + C_T/16)$ guarantees the renormalization condition $G(p = 2) = \frac{1}{4}$.

5.4.1 Results

We fit the expression in (5.48) to the lattice data of the longitudinal gluon propagator, for $p > 2$ Gev. We present the result in Figure 5.1 for a sample of data, at low and high temperatures and also around the phase transition $T_c = 0.303$ Mev. The contact term calculated as the fit parameter to each set of lattice data as a function of temperature is presented in Figure 5.2 The first observation is that slightly after the phase transition, the contact term becomes increasingly positive. Thus C_T might be considered as a new order parameter for finite temperature Yang-Mills phase transition. We check on the viability of the fit by looking at the plots of $data[i]/fit[i]$ the closer it gets to 1 the better the quality of the fit. one can see for some of the lattices there are few data points with $data/fit < 0.95$ therefore we try to improve the fit for the lattices with more than 2 points giving $data/fit < 0.95$, by chosing a subset of data with $p > 3$ Gev. The result after this improvement is shown in Figure 5.3 There is a large effect of systematics that keeps us from any firm interpretation of the data below T_c. We relegate their study to Section 5.8

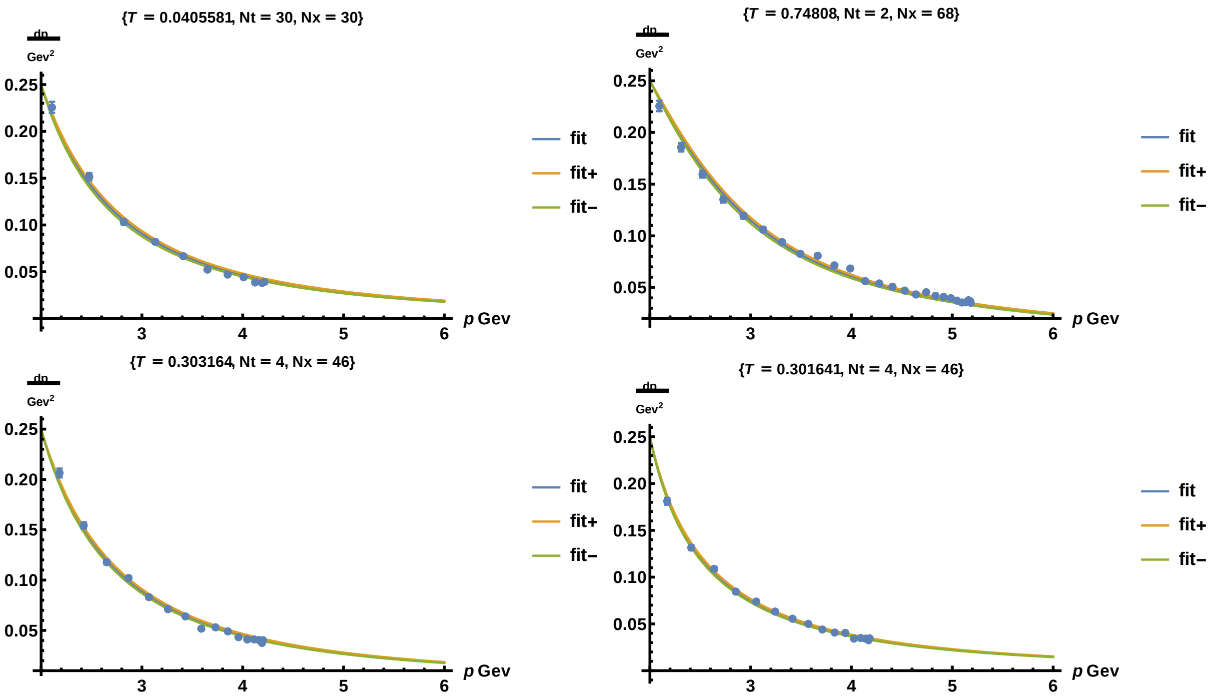

Figure 5.1: The fit function with the corresponding lattice data for low temperature (top panel, left), high temperature (top panel, right) and the vicinity of T_c (bottom panels), the legends "fit", "fit+" and "fit-" correspond to the fits to the average and upper bound and lower bound of the data.

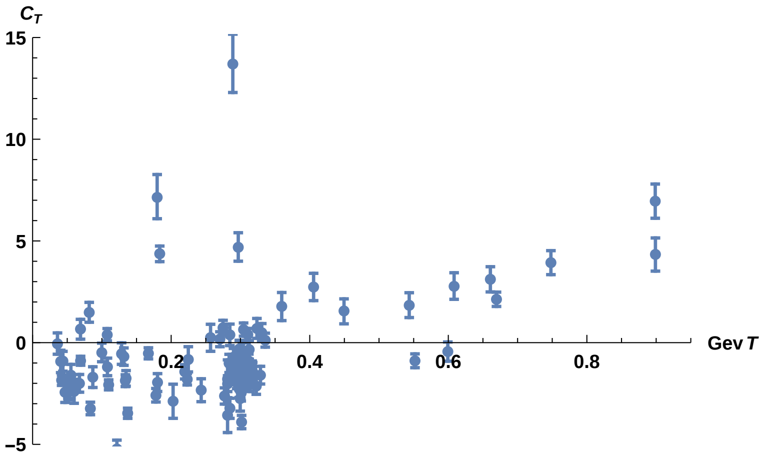

Figure 5.2: The contact term C_T in terms of the temperature T

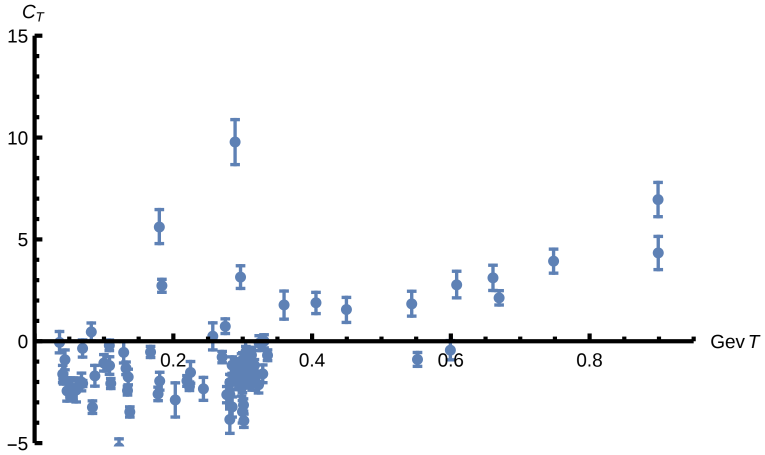

Figure 5.3: The contact term C_T in terms of the temperature T

5.5 Equation of state

In this section we try to calculate the equation of state of $SU(2)$ Yang-Mills theory at finite temperature. The pressure is given by

$$P = \frac{1}{\beta V} \ln Z, \tag{5.49}$$

$$\ln Z = \mathrm{Tr} \ln D, \tag{5.50}$$

where Z is the partition function and $D = G^{-1}(p)$. Thus the formal calculation of the pressure, using 5.46 would be

$$\begin{aligned} P &= \frac{1}{\beta V} \mathrm{Tr} \ln[G_0'^{-1}(p) + C_T G_0'(p)] \\ &= \frac{1}{\beta V} (\mathrm{Tr} \ln[G_0'^{-1}(p)] + \mathrm{Tr} \ln[1 + C_T G_0'^2(p)]) \end{aligned} \tag{5.51}$$

In order to obtain the pressure explicitly in terms of the temperature we fit different polynomials up to the 4th order in T to the C_T data presented in Figure 5.3. Here we use the result of the best fit, and we relegate the discussion of the fits quality to the next section. The fit function that we choose to apply in the pressure calculation is of the form

$$C(T) = a + bT^2, \tag{5.52}$$

$$\{a, b\} = \{-1.7, 9.4\}, \tag{5.53}$$

a and b are fit parameters. The fit to the data is presented in Figure 5.4

Tr is running over all the momenta and frequencies and since we fit to the data with zero Matsubara, Tr is equivalent to a three dimensional integration in the momentum space.

$$\mathrm{Tr} \equiv \sum_{\mathbf{p}} \equiv V \int \frac{d^3p}{(2\pi)^3} \tag{5.54}$$

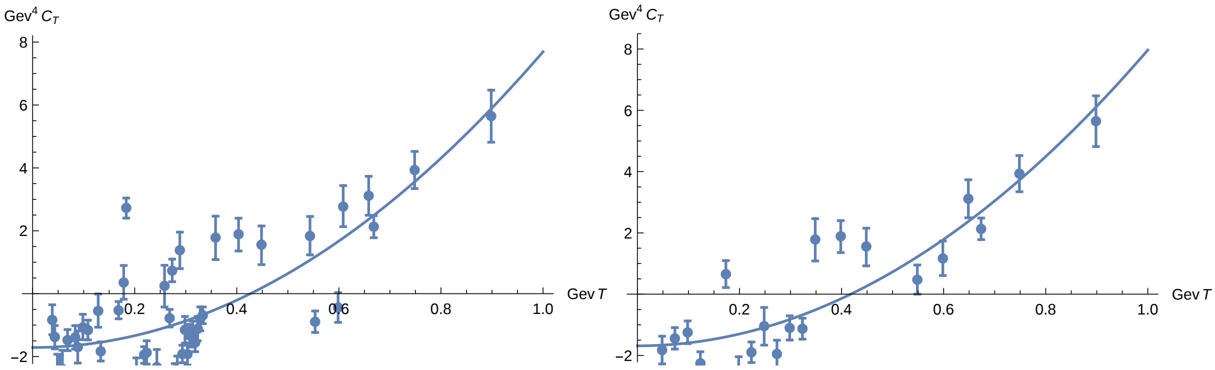

Figure 5.4: The fit to the C_T data for the smallest (left) and largest bin-size 5 and 25 Mev, respectively.

Since we are interested in the contribution of the contact term to the pressure, we calculate it explicitly, using the following approximation

$$\begin{aligned} P_c &= \frac{1}{\beta}\int \frac{d^3p}{(2\pi)^3}\ln[1+C(T)G_0'^2(p)],\\ \frac{T^2}{p^2}\ll 1 \Longrightarrow P_c &= \frac{1}{\beta}\int_2^{\infty}\frac{d^3p}{(2\pi)^3}(a+bT^2)G_0'^2(p),\\ P_c &= \frac{k_BT}{2\pi^2}(0.31(a+bT^2)),\\ \underset{(5.53)}{\Longrightarrow} P_c &= \frac{k_BT}{2\pi^2}(-0.53+2.9T^2). \end{aligned} \tag{5.55}$$

In this exploratory calculation, we only took the contribution of gluons to the pressure. In order to obtain the full expression for the pressure of $SU(2)$ Yang-Mills, we need to apply our method to the ghost propagator as well and include both. Though straightforward, it is beyond the scope of this thesis. In the next section we use the binning method that we mentioned here to decrease the statistical error on the C_T data.

5.6 Binning of data and fit to C_T data

In order to decrease the statistical error of the data we use the binning method, which means, for each set of data in the region of temperature of the size= b_s, we take the average on the values of C_T to be called $\overline{d}(a+b_s/2)$ and associate the point $\{a+b_s/2, \overline{d}(a+b_s/2)\}$ to a set of data located in the region $a+b_s$. This procedure is repeated for all the subregions of temperature of size "b_s"from the first available temperature a to the last b. We varied the bin-size b_s from 0.005 to 0.025 Gev.

The next step is to fit different polynomials with the degrees from 1 to 4 in the following we present the result of fitting various polynomials of the form $a_0 + a_iT^i, i = 1, .., 4$ to the binned data of different binning size, identified in each plot's label in Figure 5.5 from the fit functions in

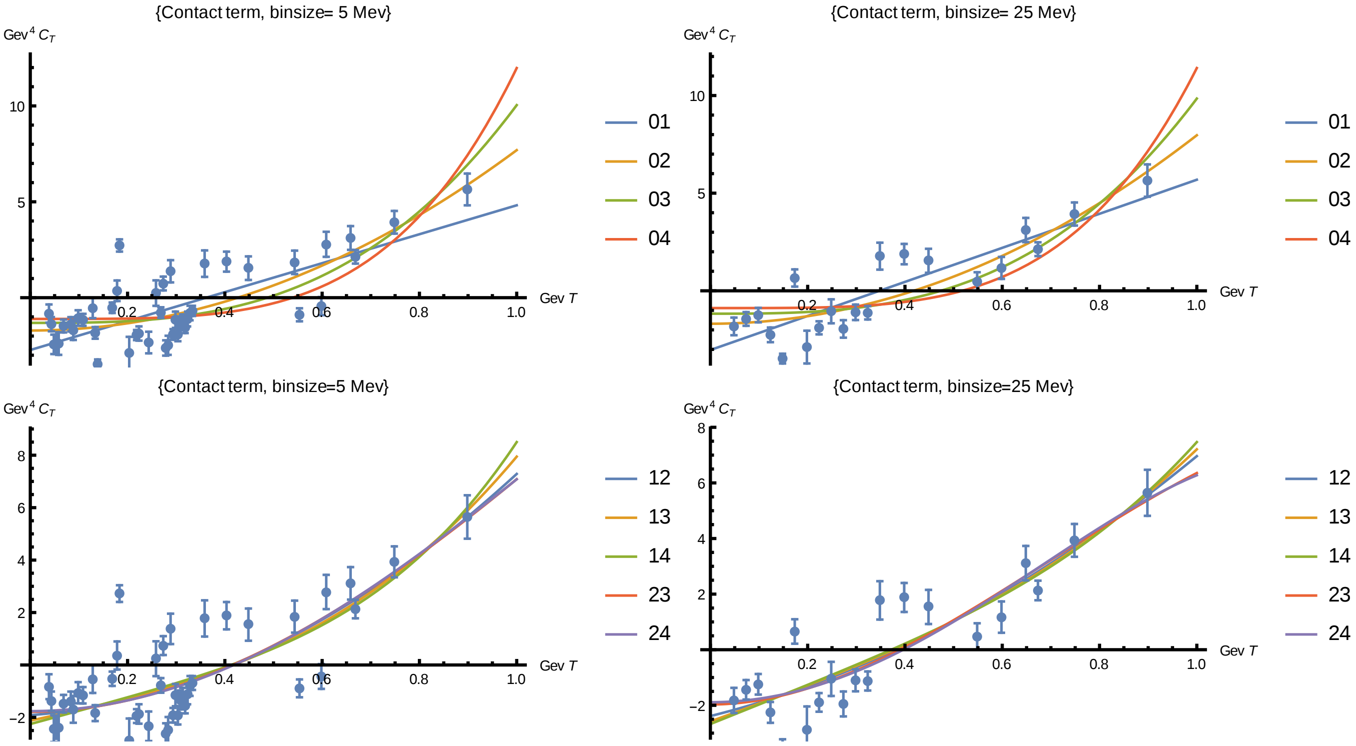

Figure 5.5: The fit to the C_T data for the fit function $a_0+a_iT^i$, $i = 1, .., 4$ (top panels) The legends of the form ”$1i,\ i = 2, 3, 4$” correspond to $a_0+a_1T+a_iT^i,\ i = 2, 3, 4$ (no sum over i) (bottom panels), accordingly ”23” and ”24”, respectively represent $a_0 + a_2T^2 + a_3T^3$ and $a_0 + a_2T^2 + a_4T^4$.

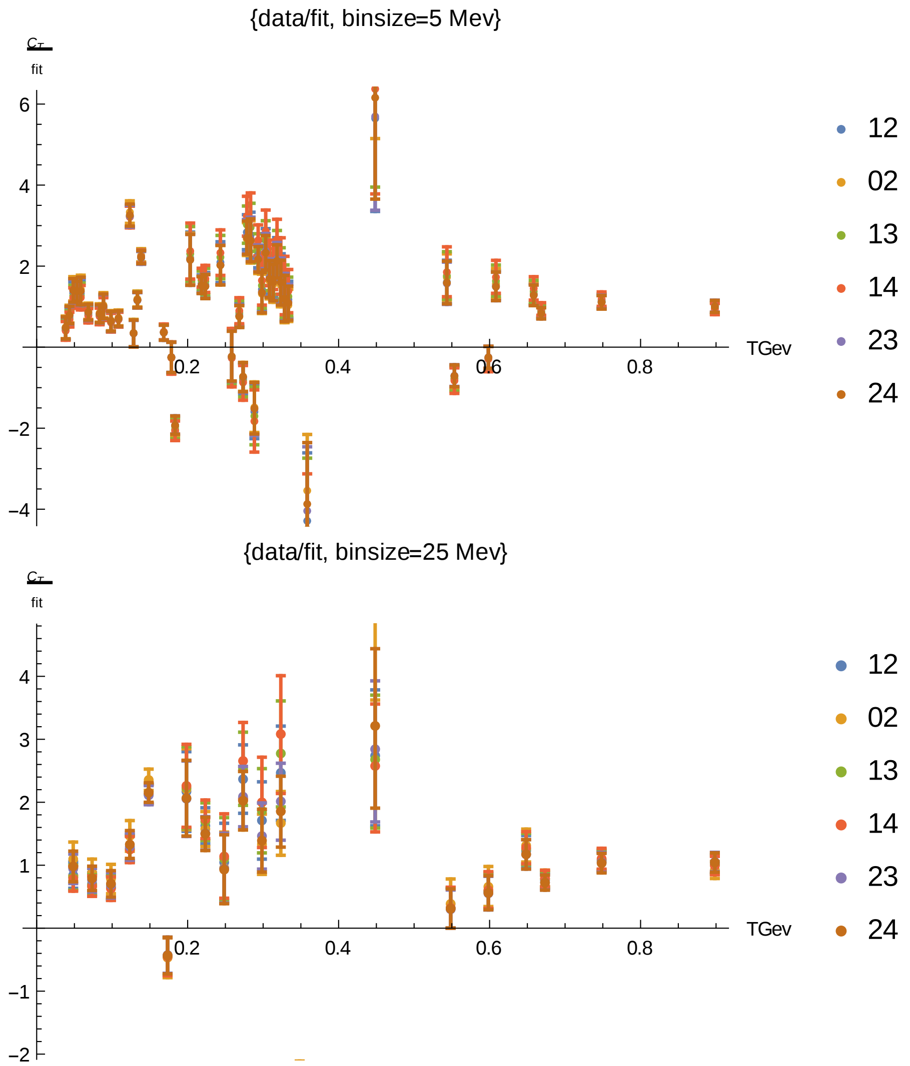

Figure 5.6: $data/fit$ for binsize 5 Mev (top panel) and for binsize 25 Mev (bottom panel). Different legends represent various fit functions to the data as indicated in Fig. 5.5

the top panel of Figure 5.5, the one quadratic in T, shows the best agreement to the data. The bottom panel are all in a good agreement with the data. We applied the χ^2-test, and found the quadratic fit of the form $a_0 + a_2T^2$, slightly better than other fit functions. That is the reason we used it in the calculation of the pressure. In order to estimate the quality of these fits we plotted the $data/fit$ for all the bin-size we show it here for the smallest and the largest binsizes 5 Mev and 25 Mev. As seen in Figure 5.6, all the fits that are presented are equally good and we need much more precise data to decide between them.

5.7 Conclusion and outlook

The primary aim of this project is to extract the equation of state from the gluon propagator at finite temperature. In analogy to a formulation developed in the context of condensed matter physics, we applied a one parameter fit ansatz for the gluon propagator. In order to calculate the pressure we need to have this parameter as a function of temperature, while we only have it for different lattice setups. Thus we fit different polynomials to this data. The most viable one is the fit quadratic with temperature, applying this fit function in the relation for the pressure we could calculate the gluon contribution to the pressure. The next step would be to apply the method to the ghost propagator and take also the contribution of the ghost into the account. In order to decide between the fit polynomials to C_T data, we need higher statistics and as always more lattice setups to reduce the effects of the lattice artifacts.

5.8 Systematics

We also studied the effect of the breaking of rotation symmetry and other discretization artifacts in Figure 5.7. In the top panel, we see that at almost the same temperature we got two different value for C_T, belonging to two different spacial lattice size, while they have equal temporal size and thus this discrepancy could be an effect of finite lattice sizes. We can see similar effects in the bottom panel for the temporal extension. These effect are strongest at low temperatures, where we could weaken them to some extent by the binning procedure.

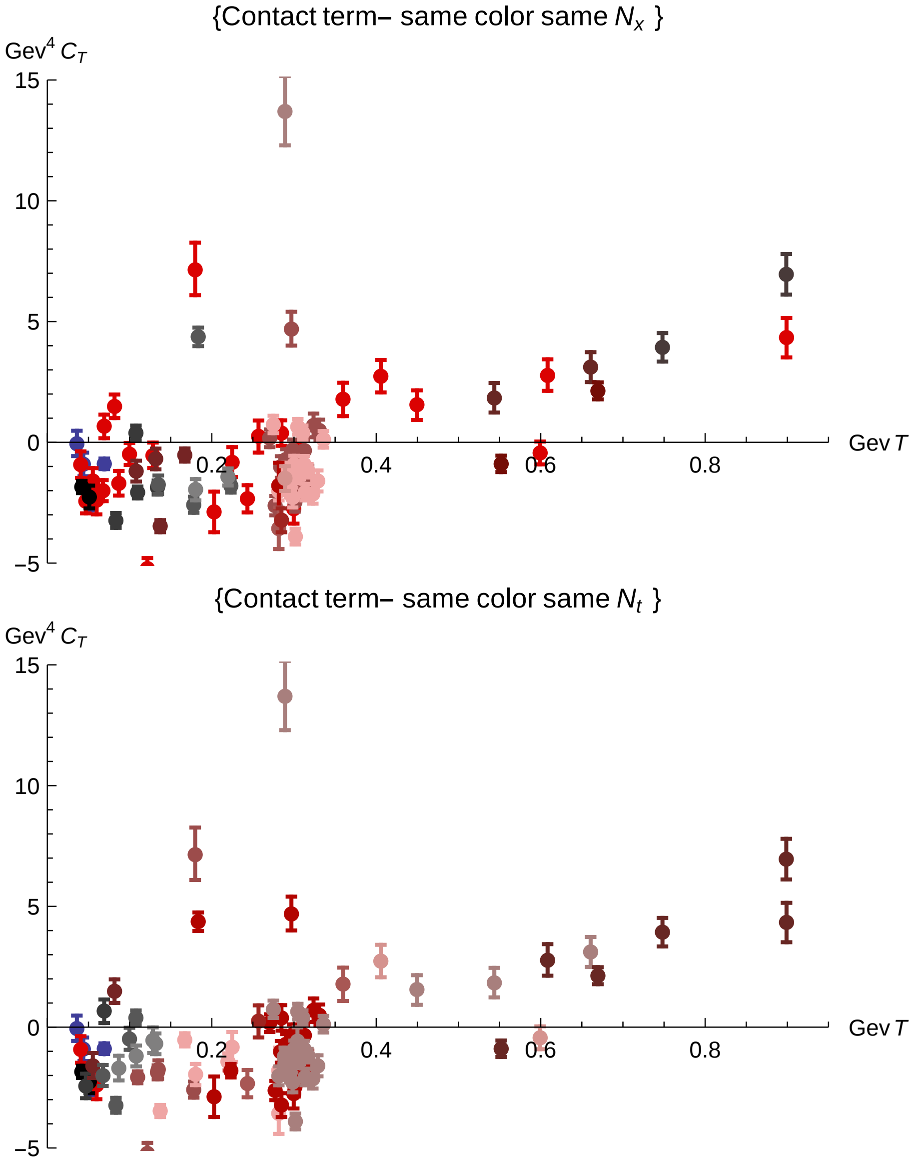

Figure 5.7: Contact term as a function of temperature, different colors indicate different N_t (top panel) and different N_x (bottom panel)

Chapter 6

G$_2$-QCD Neutron star

6.1 Introduction

As we already mentioned, a strong motivation for studying the QCD-like theories is to understand the structure of neutron stars, as cold and dense strongly interacting matter. Since the infamous sign problem makes it impossible to study QCD at finite density on the lattice, we try to get an insight to the real case by studying QCD-like theories at finite density using the lattice method. In this chapter, we are going to present the results of a direct application of these kind of studies to the problem of the neutron star structure. In Chapter 2, we saw that G_2 and $SU(2)$ share essential features with the $SU(3)$ gauge theory, so we may wonder, if such similarities can be found in the structure of the macroscopic objects with interactions governed by each of these theories. In order to address this question more specifically, we notice that some properties of the macroscopic objects are inherited from the microscopic theory by construction and some are dynamical. The dynamical effects of QCD at finite density are the main challenges in understanding the neutron star structure. So we construct a neutron-star like object that is similar to the real neutron star as much as possible so that we may carry over the macroscopic properties to the case of a real neutron star. G_2 is the optimal choice that can provide us with the fundamental degrees of freedom necessary for our purpose. Namely quarks that form a ”G$_2$neutron” ($7 \bigotimes 7 \bigotimes 7 = 1 \bigoplus ...$) and thus a G$_2$ neutron star in the same line with QCD. As we already discussed in Chapter 2, because of the reality of all its representations, G$_2$ in contrast to QCD, is accessible to lattice simulations at finite density. We therefore use the data for the baryon number density as a function of the chemical potential to calculate the equation of state of the neutron star, based on a few minimal assumptions and then using the Tolman-Oppenheimer-Volkov (TOV) equation we calculate the mass-radius equation of the G$_2$-QCD neutron star. This chapter is organized as follows:

In the next section we review the evolution process of stars which finally form a neutron star and sketch the argument that leads us to the TOV equation for the neutron star mass-radius relation. In the third section, we discuss the G$_2$-QCD lattice data of baryon number density versus chemical potential and the derivation of the equation of state from this data. The fourth section is devoted to the results obtained for the mass-radius relation of G$_2$-QCD neutron stars as well as mass and radius vs central chemical potential. In the fifth section we discuss the sources of systematic errors and possible ways to improve it. We then conclude with the summary and outlook for further studies along these lines.

6.2 Mass-radius relation of a neutron star

Neutron stars are the densest and smallest stars, with the mass comparable to the mass of the sun but a size much smaller than the one of the earth. They are the remnant core of supernovae explosions of heavy stars with masses above $8M_\odot$. This core collapses under the strong gravity and low thermal pressure. It becomes so dense that is finally stabilized due to the Fermi pressure. Conservation of the angular momentum then requires them to rotate very fast with the period of rotation between 1.4 ms to 30 s. This fast rotation induces a strong magnetic field around the star that is one of the main sources of their detection. On the other hand the high density and rapid rotation of the star make the curvature of the space time around it highly nontrivial. Thus neutron stars are relativistic objects. This requires the application of the theory of general relativity (GR) to formulate the mass-radius relation. First, we shortly introduce aspects of the Einstein equations that are of relevance for our argument and then we sketch the derivation of the TOV equation. The Einstein equations quantify the relation between matter and space-time. Namely, how the distribution of mass-energy in space and time can form the geometry of space time and vice-versa. In these equations the matter part is represented by the energy-momentum tensor $T^{\mu\nu}$ and the geometry of space-time or equivalently gravity by the metric tensor $g^{\mu\nu}$, thus the Einstein equations will be of the form

$$G^{\mu\nu} = \kappa T^{\mu\nu} \quad \kappa \sim G \tag{6.1}$$

where $G^{\mu\nu}$ is a function of the metric $g^{\mu\nu}$ and its derivatives. The constant κ is fixed by looking to the classical limit of the theory, namely by the Newtonian gravity (G is the Newton constant). The Tolman-Oppenheimer-Volkov equation for $M(R)$ of compact stars is derived based on a few simplifying assumptions. The first one is to assume that the metric is spherically symmetric and static, thus the invariant length, which is generally of the form

$$d\tau^2 = g_{\mu\nu} dx^\mu dx^\nu, \tag{6.2}$$

takes the form

$$d\tau^2 = U(r)\, dt^2 - V(r)\, dr^2 - r^2(d\theta^2 + \sin^2\theta\, d\phi^2). \tag{6.3}$$

Which is justified in the absence of a strong external fields and also assuming local equilibrium.

The second assumption is that the neutron star matter is a perfect fluid, based on its similarity to the nuclear matter. Thus the energy momentum tensor is given by

$$T^{\mu\nu} = -p\, g^{\mu\nu} + (p+\epsilon)\, u^\mu u^\nu \tag{6.4}$$

$$u^\mu = \frac{dx^\mu}{d\tau} \overset{(6.2)}{\Longrightarrow} g_{\mu\nu} u^\mu u^\nu = 1. \tag{6.5}$$

Where p and ϵ are respectively the pressure and the energy density of the ideal fluid. For the static star the three-velocity of each element of the fluid is zero,

$$u^\mu = 0\,(\mu \neq 0), \;\; u^0 = 1/\sqrt{g_{00}}. \tag{6.6}$$

This reduces (6.4) to

$$T^{\mu}_{\mu} = p(r)\ (\mu \neq 0),\ \ T^{0}_{0} = \epsilon(r). \tag{6.7}$$

Therefore only diagonal elements survive in the equation (6.1), the general covariance condition[1] put another constraint on this set of equations and finally we end up with three independent equations of the form (no sum over the Lorentz indices is implied.)

$$G^{\mu}_{\mu}(U(r), V(r)) = \kappa T^{\mu}_{\mu}(r), \tag{6.8}$$

leading to equations for $U(r)$ and $V(r)$, both functions of $p(r)$ and $\epsilon(r)$ and their derivatives. Combining these equations and using ($M(R) = 4\pi \int_0^r \epsilon(r')\, r'^2\, dr'$), where $M(R)$ is the mass-energy enclosed in radius r. Finally we arrive at the TOV equation,

$$\frac{dp(r)}{dr} = -\frac{[p(r) + \epsilon(r)]\,[M(R) + 4\pi r^3 p(r)]}{r\,[r - 2M(R)]}. \tag{6.9}$$

It is now clear why we need to know the equation of state $p(\epsilon)$ to know the equation of structure $M(R)$. We now can write the TOV equation in terms of one thermodynamic variable and its derivative and integral e.g. $\epsilon(r)$. Finally we can solve this integro-differential equation, using numerical methods. This equation puts a limit on the maximum mass that a stable compact star can reach. The existence of such a maximum is independent of the equation of state but not its value. Before going to the details of the calculation for a certain equation of state, we make few general observations by analyzing the TOV equation. As we expect intuitively, pressure acts against the gravity to keep the star stable, the larger the mass of the star, the higher the central pressure that sustains its stability. However the TOV equation tells us that an increase in the pressure, increases the drop of it by getting away from the center. Since at $p = 0$ the surface is reached, for too high central pressures the surface is reached too fast and thus we end up with lighter and smaller stars that eventually collapse to blackholes. Therefore for any equation of state there will be a maximum for the mass of the neutron star, so that the increase of the central density does not give a mass beyond this maximum but the resulting branch will be unstable.

There is a limit on the maximum mass of the neutron star that no matter what the equation of state is, the maximum can not get larger than this limit. The value of this limit is calculated to be around $3M_{\odot}$, based on a few general and accepted assumptions, which are listed below:

i: General relativity and its consequences are valid

ii: Matter is stable under a local disturbance $dp/d\epsilon \geq 0$

iii: Disturbances propagate with the speed less than the speed of light $\sqrt{dp/d\epsilon} < 1$ (causality constraint)

iv: The high density equation of state satisfying the above constrain must match continuously to the low density one that described the ordinary matter.

In order to provide a baseline for our study we will solve the TOV equation for the e.o.s of the free neutron gas and later we will compare its results with the G_2-QCD ones.

---

[1] The condition that guarantees the invariance of the form of a physical law under any coordinate transformation

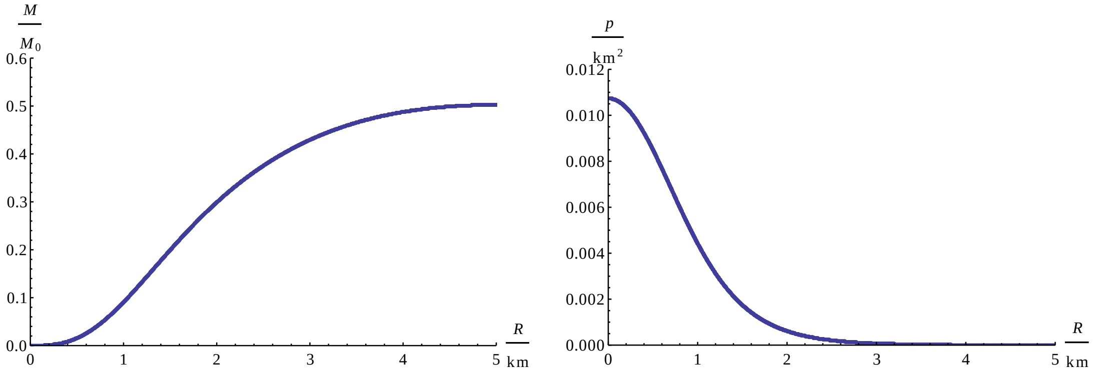

Figure 6.1: Integrated mass as a function of radius (left panel) internal pressure as a function of radius (right panel) for free neutron gas star with $\mu_c = 10\ \text{fm}^{-1}$

6.3 Neutron star composed out of the free neutron gas

The equation of state for $T = 0$ is given by

$$p = n\mu - \epsilon,\ \frac{dp}{d\mu} = n, \tag{6.10}$$

where ϵ is the energy density and n is the number density of neutrons. p and μ denote pressure and chemical potential, respectively. We rewrite the TOV equation in terms of $\mu(r)$ (the chemical potential as a function of radius) using $\frac{dp}{dr} = \frac{dp}{d\mu}\frac{d\mu}{dr}$, which reads

$$\frac{d\mu(r)}{dr} = -\frac{[\mu(r)]\,[M(R) + 4\pi r^3 p(r)]}{r\,[r - 2M(R)]}. \tag{6.11}$$

The above equation is valid for any equation of state at zero temperature and we are going to use it throughout this chapter. First we solve (6.11) for the equation of state of the free neutron gas. The ground State energy density ϵ of the free neutron gas is given by

$$\epsilon = \int_0^{\sqrt{\mu^2-m^2}} \epsilon(k)\, d^3k,\ \ \epsilon(k) = \sqrt{m^2 + k^2}, \tag{6.12}$$

$$n = \frac{(\mu^2 - m^2)^{3/2}}{3\pi^2}. \tag{6.13}$$

The zero temperature approximation is consistent with the situation inside the neutron star, where $n^{\frac{1}{3}} \gg T$. Plugging equations (6.13) and (6.12) into (6.10), we can write $p(r)$ in terms of $\mu(r)$ and insert it into the TOV equation. We then solve it for different central chemical potentials starting from slightly above the mass of the neutron m_n and for $M(0) = 0$, while the surface of the neutron star is reached when $\mu(r) = m_n$ corresponding to $p = 0$. The results for $\mu_c = 10$ fm^{-1} [2], where μ_c represents the central chemical potential, are presented in Figure 6.1. The result of solving the TOV equation for several values of the central chemical potentials is presented in Figure 6.2. It is observed that $M(R)$ of the neutron star composed of the free neutron gas reaches

---

[2] Although it is not a stable configuration, the generic behavior of $M(r)$ and $p(r)$ is the same for all the central densities.

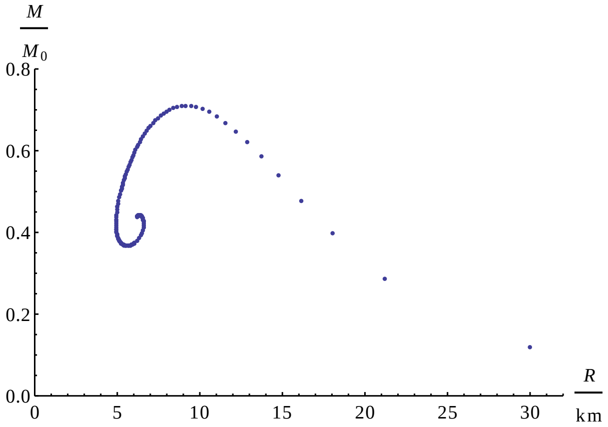

Figure 6.2: Mass-radius relation of free neutron gas star

a maximum as expected. The value of the maximum mass is $0.4M_{\odot}$, the maximum mass star has a radius around 10 km. The stable part of the curve shows that, the mass of the star increases by the increase in the central chemical potential, while the radius decreases. This is a generic behavior, and seen for different equation of states.

6.4 G$_2$-QCD neutron star

In this section we employ an equation of state, derived from lattice simulations of G$_2$-QCD at finite density, to obtain $M(R)$ for the G$_2$-QCD neutron star. First we will see, how to obtain a workable equation of state from the lattice data of the baryon number density and then we use this e.o.s to solve the TOV equation and obtain the mass-radius relation of the G$_2$-QCD neutron star.

6.4.1 Equation of state of G$_2$-QCD neutron matter

Since the only available data at the moment is that of quark baryon number density in terms of the quark chemical potential, we need to apply certain assumptions and approximations in order to obtain the equation of state. Namely, we assume that the neutron density is given by $n(\mu) = \frac{n_q(\mu_q)}{3}$, where $\mu = 3\mu_q$ and denotes the neutron chemical potential, since each G$_2$-QCD neutron is composed of the three quarks. We then approximate the energy of each particle by its rest mass energy and thus the energy density is given by

$$\epsilon = m_n n(\mu) \tag{6.14}$$

which is justified, given that the thermal kinetic energy and binding energy of neutrons are much smaller than the neutron's rest mass. Of course this approximation prevents a quantitatively reliable statement about the energy density, although the error induced by this approximation is probably less than the statistical error on the mass measurement of the G$_2$ neutron on the lattice. Of course, ultimately the direct calculation of the energy density on the lattice is necessary, which requires careful renormalization [81], and thus data for various lattice spacings. Such a calculation

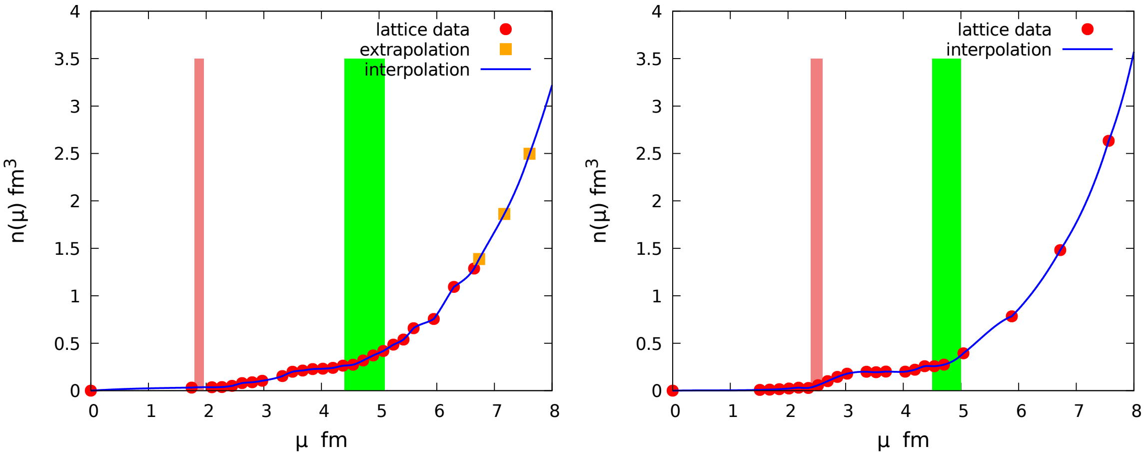

Figure 6.3: The left and right panels show the employed baryon density as a function of baryo-chemical potential, interpolated from the lattice results, and compared to the data points, of [21]. The red band shows the mass of the lightest particle in the spectrum, the diquark Goldstone, while the green band is the mass of the neutron, both values also from [21], both including statistical errors only. The left-hand-side shows the results for the light ensemble, the right-hand side for the heavy ensemble. The orange points in the light ensemble data are extracted from a fit, as explained in the text. Note that the statistical error bars for the lattice data are smaller than the symbol size. The actual μ occurring in the neutron stars is between $\mu_n \approx 4.8$ fm and $\mu \lesssim 8$ fm.

is at the moment prohibitively expensive for G_2-QCD. Therefore in our exploratory study, we rely on the above approximation. We employ the data for $n(\mu)$ from simulations given in [21]. We plot the data for light and heavy ensembles, respectively with Goldstone (diquark) mass of 247 MeV and 326 MeV in Figure 6.3. It is worth mentioning that we consider the mass of the neutron to be independent of the density, which is justified by the following argument. The plot of $n(\mu)$ in Figure 6.3 shows the emergence of plateaus at the values of the chemical potential close to the masses of the baryons in vacuum, which means that these masses are not significantly affected by the density.

Although we need to know, the baryon number density as a function of the chemical potential for all applicable values of the chemical potential μ in TOV equation, the lattice only gives us discrete points in μ. We interpolated these data using splines. Note that the average values of the lattice data are not necessarily strictly increasing because of statistical fluctuations. Where this was a problem for obtaining a thermodynamically consistent interpolation, we use the statistical 1σ error range to counteract it.

For the case of the light ensemble, the lattice data at high, but still relevant, chemical potentials is too sparse for a reliable interpolation. Based on the observations in [21], we use a Fermi-Dirac-type distribution $n(\mu) = n_s/(\exp(a - b\mu) + 1)$, where n_s is the lattice saturation density. For the present case $n_s = 14$, since the quarks are in the 7 dimensional fundamental representation of the color group and also live in 2 dimensional spin space. The parameters a and b are fitted to the last few points of the lattice data, to continue the interpolation to higher densities. The orange points in the data for the light ensemble in the left panel in Figure 6.3 are extracted from the fit, while the red ones are the original lattice data.

The short range nuclear interaction, even though being strong, will be effectively weak, acting in large distances. Thus because of the large inter-particle distances in low densities, the neutron matter behaves similar to a non-interacting Fermi gas. Therefore the final employed baryon number density of neutrons $n(\mu)$ at low densities, must behave similar to the density of a free neutron gas. However, this is not what we see in Figure 6.3. Especially, the density does not go to zero, while $\mu \to m_n$. The reason for this behavior, is the reality of all the representations of the G_2 group. More specifically, quarks and antiquarks can transform to each other and thus the Goldstone bosons of the theory, as the lightest particles of the spectrum, at the same time are diquarks and carry baryon number, thus the Silver-Blaze transition occurs at the chemical potential corresponding to the mass of the diquark, and the density is non-zero below the mass of the neutron, which is in sharp contrast to the case of real QCD, where the baryon density is zero for μ below m_n. To deal with this problem we may impose modifications to the interpolation of the $n(\mu)$ data at low densities, keeping the following points as the main purposes of this investigation in mind:

- What is necessary for an ab-initio calculation to provide a suitable result to describe a neutron star?
- Are there any generic properties of non-Abelian gauge theories that can manifest themselves in the neutron star features?

To address these questions we demand that our e.o.s shows a certain behavior that leads to generic properties of the neutron star structure like the negative slope $M(R)$ for the stable region.[3] More specifically to obey normal matter condition at low densities, thus we modify the equation of state by replacing the interpolation of the lattice data with a function of μ, of the form $c(\mu - m_n)^{\frac{3}{2}}$, resembling behavior of the density of the free neutron gas given in (6.13) for small chemical potentials, and selected the pre-factor such that the equation of state is continuous. We will return to the systematic uncertainties induced by this modification in Section 6.5. The final form of the baryon density that we are going to apply in the calculation of the mass-radius relation in the next section is given by the line indicated as "interpolation" in the figure 6.4

At the end of this section, we give arguments why it is justified to assume that the whole baryon density inside the G_2-QCD neutron star is due to the neutrons. As we know from Chapter 2, there are other color-singlet objects that carry baryon number, like the hybrid state "qggg", where a quark is screened by three gluons. If we consider the mass of the constituent gluon, around 500 Mev (according to real QCD), then the mass of the hybrid would be around 1.8 Gev. As will be shown in the next section, the core chemical potential of the heaviest G_2-QCD neutron star is below this value, thus we safely ignore hybrids in our study. Another source of baryon density could be the diquarks. Diquarks are considerably lighter than the neutrons and thus in principle could contribute in the baryon number density of the G_2-QCD neutron star. However, since they are bosons, any amount of them will collapse due to the lack of the Fermi pressure, until a density is reached, where they can be converted to neutrons in a three-to-two process. Thus, we can assume that the whole baryon density comes from neutrons. We also notice that the possibility of the decay of neutron to diquarks is also ruled out, since the only decaying chanel would be through

---

[3] Excluding the possibility of a compact star made of self-bound matter

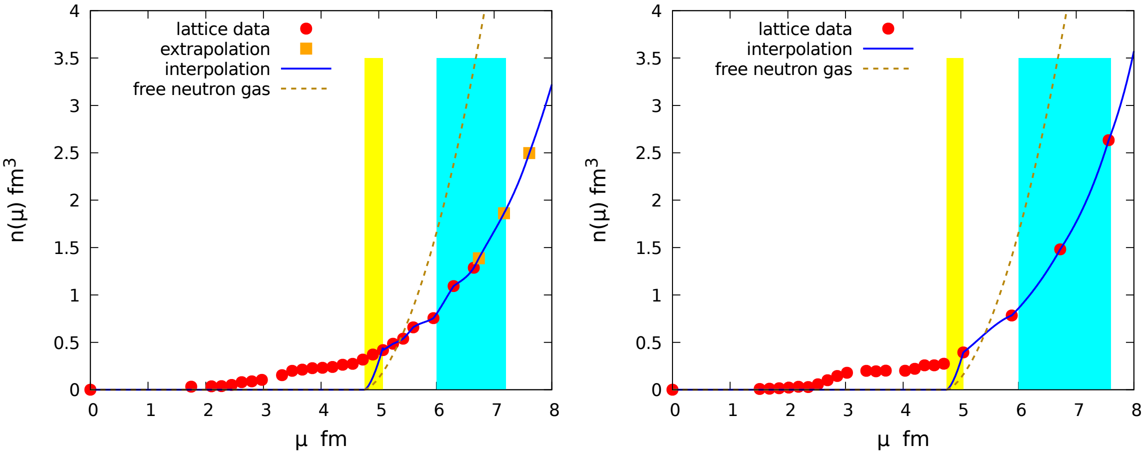

Figure 6.4: Baryon number density vs chemical potential of nucleons. Dark golden: free Fermi gas, blue with data points: G2-QCD. The yellow (left) region corresponds to the outer crust of the neutron star and the cyan (right) region to the inner core of the most massive neutron stars. The left panel is for the light ensemble and the right panel for the heavy ensemble.

the hybrid ”qggg” which is too heavy to let this happen. Of course to make a firm statement we need to calculate the mass of the hybrid on the lattice. The input from the lattice can be improved in various other ways as well. This will be discussed at the end of this chapter.

6.4.2 Mass-radius relation of a G2-QCD neutron star

In this section we employ the result of the modified interpolation shown in Figure 6.4 to calculate the mass-radius relation of the G2-QCD neutron star. In order to apply $n(\mu)$ and obtain $M(R)$, we calculate the pressure using equations (6.10) and (6.14) as follows

$$p = n(\mu)(\mu - m_n), \tag{6.15}$$

where $n(\mu)$ is presented by the blue curve in Figure 6.4. The ratio of this pressure to the pressure of the free neutron gas is plotted in Figure 6.5. It is always larger than unity, confirming the expectation that neutron stars with interacting neutron matter can sustain larger masses, being stabilized by higher pressures. At lower chemical potentials it is nearly constant because of the dilute gas behavior imposed at low density. The result for the mass-radius relation using this equation of state is given in Figure 6.6. Comparing to the free gas, the maximum mass is substantially increased. However, the maximum mass is still much lower than the maximum observed masses of neutron stars [82]. Since this does not change substantially for the different Goldstone masses, and is not strongly affected by the systematic effects studied in Section 4.7, the origin of this is unclear. Nevertheless, we can count a few possible origins. One is the role of the current mass of the quarks, so that the situation close to the chiral limit could be significantly different [4]. Another source of such an effect would be the fact that the lattice data is generated only for one flavor and it may be

---

[4] Here we used quarks with masses 20 Mev and 50 Mev, far from the chiral limit although comparing their results we did not see any difference

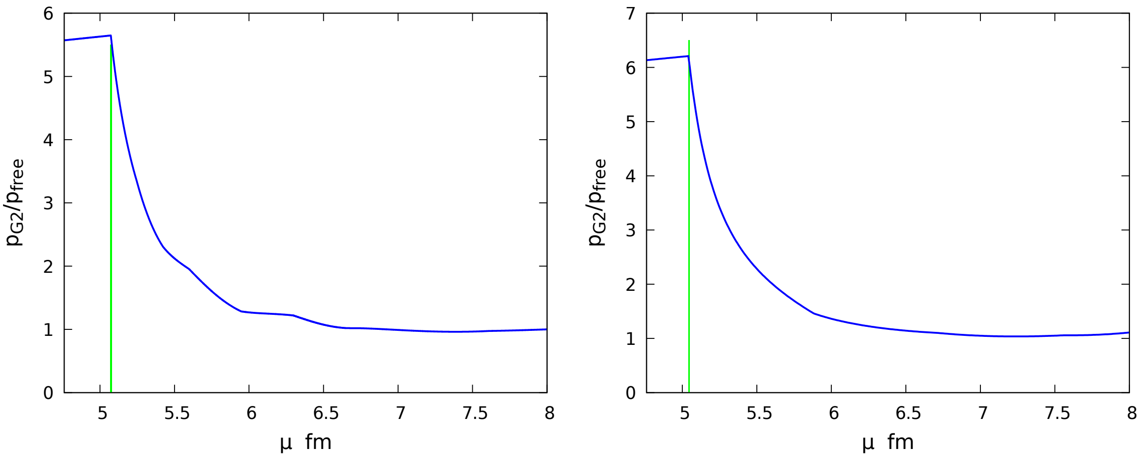

Figure 6.5: The ratio of the pressure of G_2 QCD and the free neutron gas in the present approximation, where the green line shows the transition to the dilute neutron gas region.

the case that including 2 flavors, distinguishing proton and neutron, makes the G_2 nuclear matter more similar to the QCD one. Therefore the resulting $n(\mu)$ and consequently $M(R)$ may come to a closer agreement with observations. After all, G_2-QCD at finite density may be fundamentally different from its QCD counterpart and the theory may not potentially be able to reproduce the the properties of neutron stars seen in nature. This would be an important conclusion about the large scale properties of non-Abelian gauge theories. The lattice artifacts, especially the finite volume effects, can also be a reason for a too small maximum mass. Finally, the assumptions and approximations made to obtain the equation of state might be oversimplifying and overlook essential informations. All of these issues could be checked with improved results for the equation of state from the lattice, and by moving closer in all parameters to full QCD. While too expensive at the present time, this is straightforward. Influences from β-equilibrium or other weak corrections cannot, be checked on the lattice yet, most importantly because of the wide range of the energy scales which are involved in the processes, and would require other approaches. All of these possible sources of influence should be kept in mind in the following. Some of the points mentioned, will be discussed in detail in Section 6.5.

The first observation is that the results of both ensembles are even quantitatively very similar for all the quantities plotted in Figure 6.6. This may indicate that the current mass of the quarks does not play a significant role in these results. Although we need to examine many more ensembles to confirm this claim.

A very important feature of $M(R)$ of a G_2-QCD neutron star, is its sharp maximum compared to the free gas neutron star, that means an (almost) maximum mass G_2-QCD neutron star has a constant radius. This of course implies that a G_2-QCD neutron star is less stable against external perturbations. On the other hand the fact that both maxima of the free and interacting cases, occur for stars with the radius around 10 km, is also striking and may be a consequence of the TOV equation and independent of the equation of state.

Another interesting observation in Figure 6.6 is a so-called crossover that is seen in all the

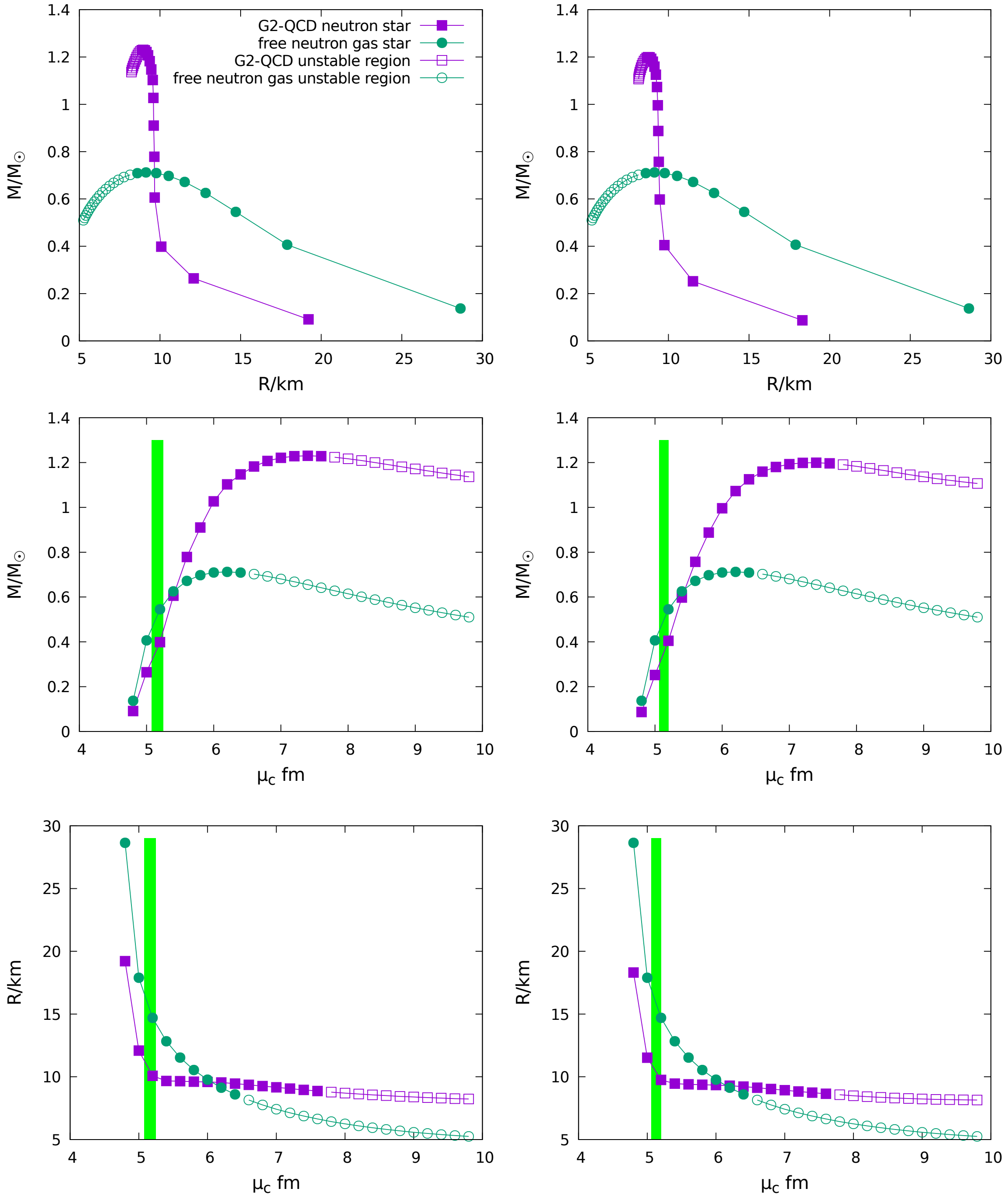

Figure 6.6: The top panels show the mass-radius relation for the G_2 neutron star (left panels: light ensemble, right panels: heavy ensemble) (purple) in comparison to the result for the free Fermi gas (green). The lower panels show the mass (middle) and radius (bottom) as functions of the central chemical potentials. The green bar in the lower panels indicate the transition point to the free gas approximation in chemical potential.

plots[5]. The main effect is that for low chemical potentials the non-interacting case has a larger mass than the interacting one at fixed central chemical potential or fixed radius. The crossover occurs at $R = 10$ km and $M/M_\odot \sim 0.7$ (the maximum of $M(R)$ for the free neutron gas star), after which the mass of the interacting star is always larger than the free one. The corresponding behavior seen in $M(\mu_c)$ is less significant but could hint on the physical meaning of the effect. It shows that the crossover occurs at the same μ_c as a crossover occurs in Figure 6.4, when the density of the free neutron gas crosses the curve of the G_2-QCD density. Namely the star with the larger $n(\mu_c)$ has a smaller mass. Since the star with smaller density in the core region has less mass to withstand in the corresponding region against the collapse and thus it can sustain more mass. This property is seen in the interacting case in higher chemical potentials and thus this case reaches the higher masses compared to the free case.

We also notice another feature in the mass-radius relation in Figure 6.6 that can be traced back to the equation of state and more specifically to the density: At a radius of about 10 km, and a mass of 0.4 solar masses for both ensembles, there is a strong change of slope. Comparing this to the core chemical potentials, the value is quite interesting. It is roughly the value, where the transition from the free gas to the interpolation of the lattice data takes place. Thus, this is where interactions become the dominating effects, and the equation of state appears to enter a region dominated by fermionic hadrons [21]. Therefore, this rapid change of properties impresses itself on the mass-radius relation. This could imply that changes of slope of $M(R)$ could also be related to different physics. This would therefore be a highly interesting signature for observational astronomy of neutron stars. Of course, this would require rather precise radius determinations, which remain a challenge.

The question about the internal structure of neutron stars, with respect to the possible phase transitions inside the star, can also be addressed by investigating the behavior of the accumulated mass as a function of the radius $M(R)$ starting from the center and ending at the surface of the star. This is shown in Figure 6.7 where we also plotted $p(r)/p_c$. The most interesting observation is that the inflection point of the $M(R)$ curve almost coincides with the point of the transition to the dilute neutron gas phase, indicated by the green line. It corresponds to the point of the change of slope in the $M(R)$ curve in Figure 6.6. Namely μ_c of the stars around the point of the sudden rise in $M(R)$ in Figure 6.6 is about the value of the chemical potential of the inflection point, indicated by the green line in Figure 6.7.The plots also show that the star with higher μ_c and thus larger central density, has a smaller shell of essentially non-interacting neutron matter (the outer shell). This is a consequence of the TOV equation, as here more central gravitational pull is present, and therefore the outer crust gets more compressed. In other words, the contribution of the strongly-interacting region to the volume becomes larger when increasing μ_c.

This is also visible when studying the chemical potential profiles in Figure 6.8. The interacting case supports much larger central chemical potentials than the non-interacting case. Also the rate of change is higher for the interacting case than for the free case.

Observing the effect of imposing the equation of state of the dilute gas at the low densities, we might ask how would the results change by varying the point of the transition to the almost non-interacting region to be shown by μ_t. This question and other systematic effects, induced by

---

[5] although not at exactly the same mass in $M(R)$ and $M(\mu_c)$ plots. This small discrepancy is most probably a consequence of the TOV equation.

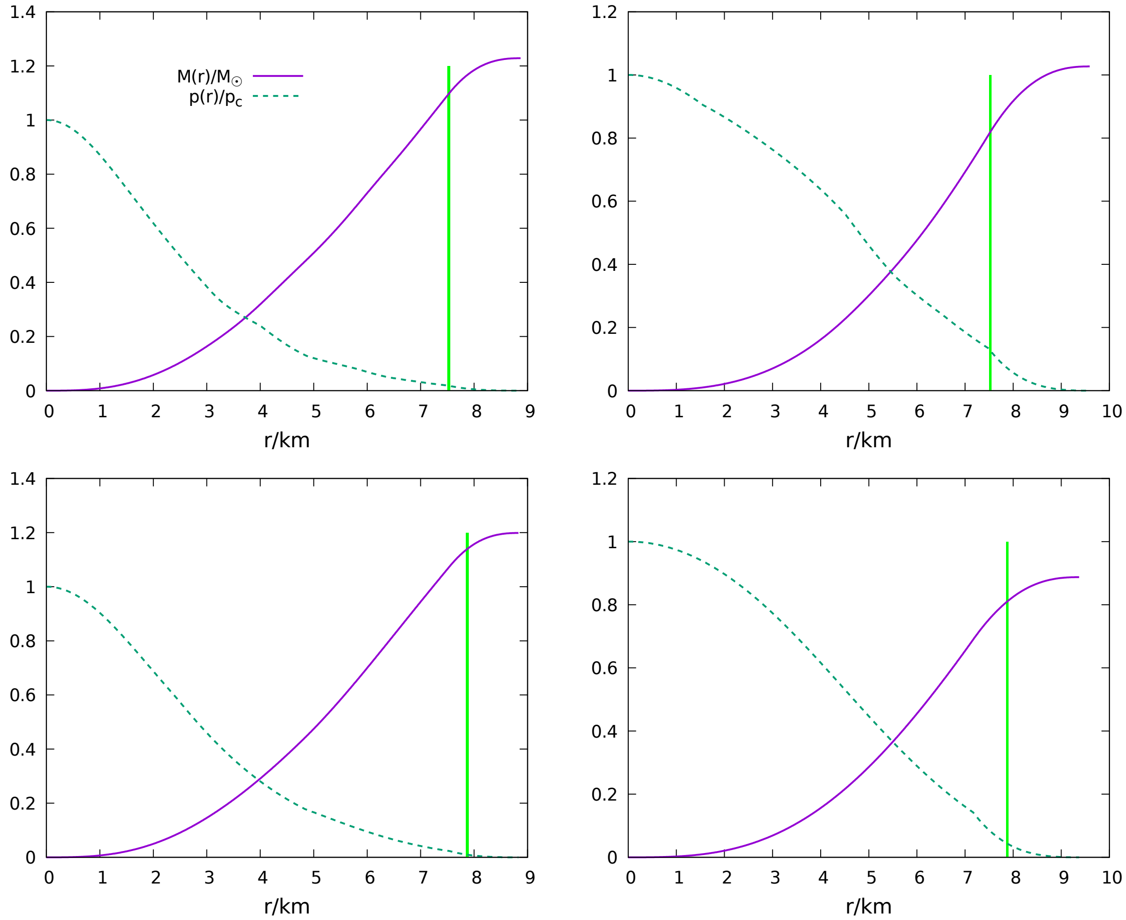

Figure 6.7: Accumulated mass in solar mass units (purple) and the ratio of the pressure to the central pressure (green) as a function of distance from the center of the neutron star for two different central chemical potentials. The top panels are for the light ensemble at $\mu_c = 7.6\ \text{fm}^{-1}$ (left) and $\mu_c = 6\ \text{fm}^{-1}$ (right), and the bottom panel for the heavy ensemble at $\mu_c = 7.2\ \text{fm}^{-1}$ (left) and $\mu_c = 5.8\ \text{fm}^{-1}$ (right), respectively. The green line indicates the transition to the free gas in the chemical potential.

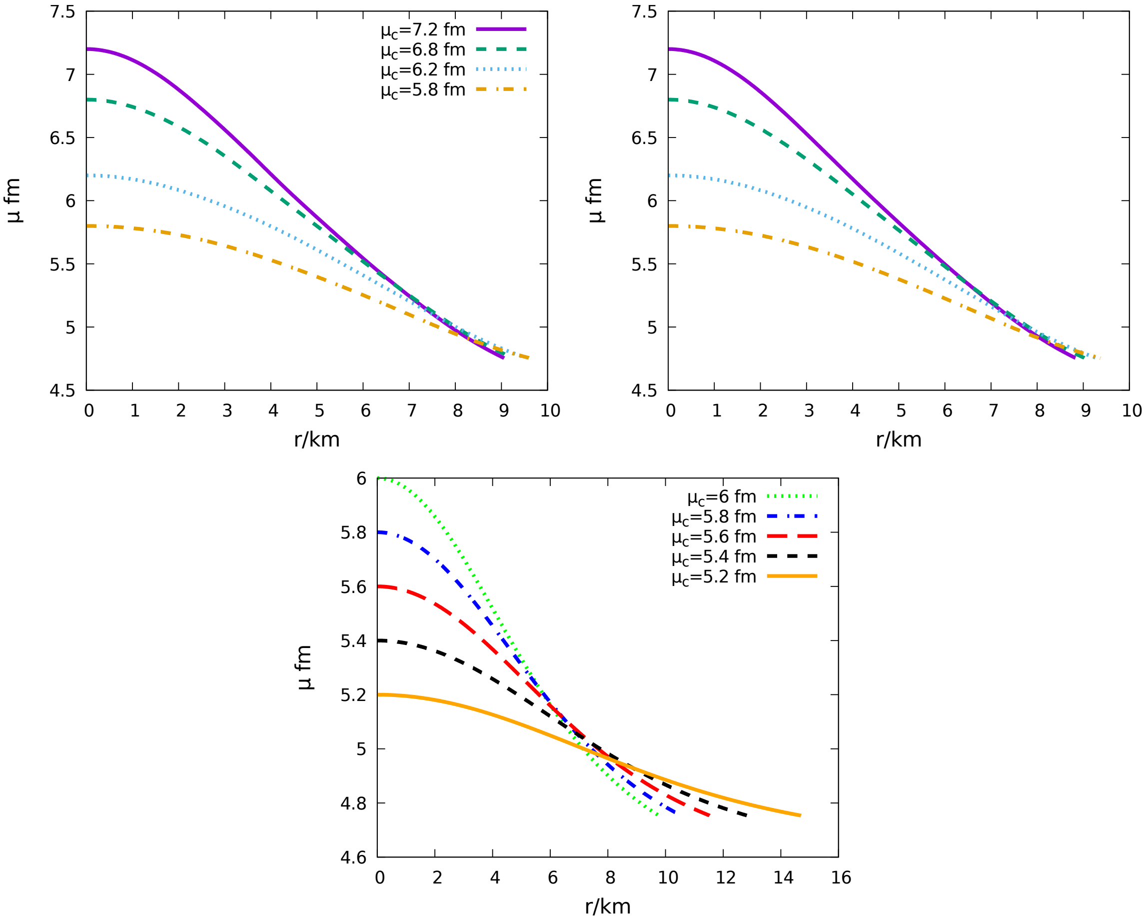

Figure 6.8: The chemical potential as a function of distance from the center for different values of the central chemical potential for G_2-QCD (top left: light ensemble, top right: heavy ensemble) and for the free neutron gas (bottom). Note that the slope is negative throughout, as is required for a star in stable equilibrium.

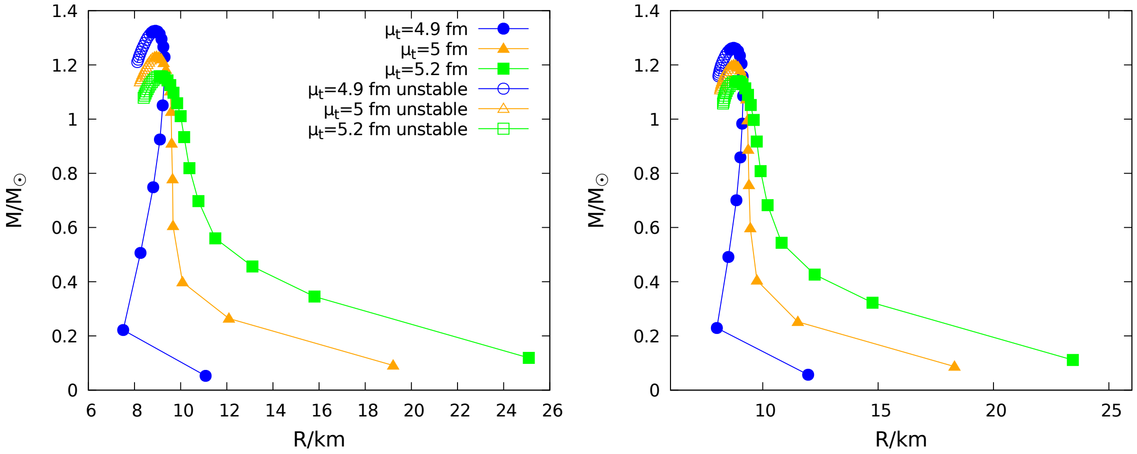

Figure 6.9: Mass-radius curves for three different values of the chemical potential of the transition to the dilute Fermi gas region, $\mu_t = 4.9$ fm^{-1} (blue curve), $\mu_t = 5$ fm^{-1} (orange curve), and $\mu_t = 5.2$ fm^{-1} (green curve) for the light ensemble (left panel) and the heavy ensemble (right panel) (lines connecting numerical points are to guide the eye).

the assumptions and approximations will be addressed in the next section.

6.5 Estimate of systematic effects

In this section, the effects of different approximations, which are made to obtain the equation of state only from the lattice data for quark baryon number density as a function of the quark chemical potential, represented by $n_q(\mu_q)$ are investigated. Of course there are sources of other errors like finite volume or discretization effects, that are not addressed here due to a lack of relevant data.

6.5.1 Effect of the interface point to the free gas

As noted in the main text, in order to reproduce the normal matter behavior at low densities, we replace the result of the interpolation of the lattice data in that region by an ansatz that resembles the density function of a free neutron gas. As already discussed in Section 6.4.1, the motivation for this modification is that, while our target is the density of neutrons, at low densities diquarks also contribute in the density. We investigate the effect of this unwanted contributions in this section by varying the value of μ_t, the result is presented in Figure 6.9. The essential remedy of this problem would be to calculate the density of neutrons and the energy density directly on the lattice. In the absence of such results, we rely on the present approach.

in Figure 6.9, we observe that for lower μ_t we get a larger maximum mass, that is understood as a consequence of the larger contribution of the interacting part. On the other hand the lowest choice, $\mu_t = 4.9$ fm^{-1} includes much of the diquark sector in the density, leading to the change

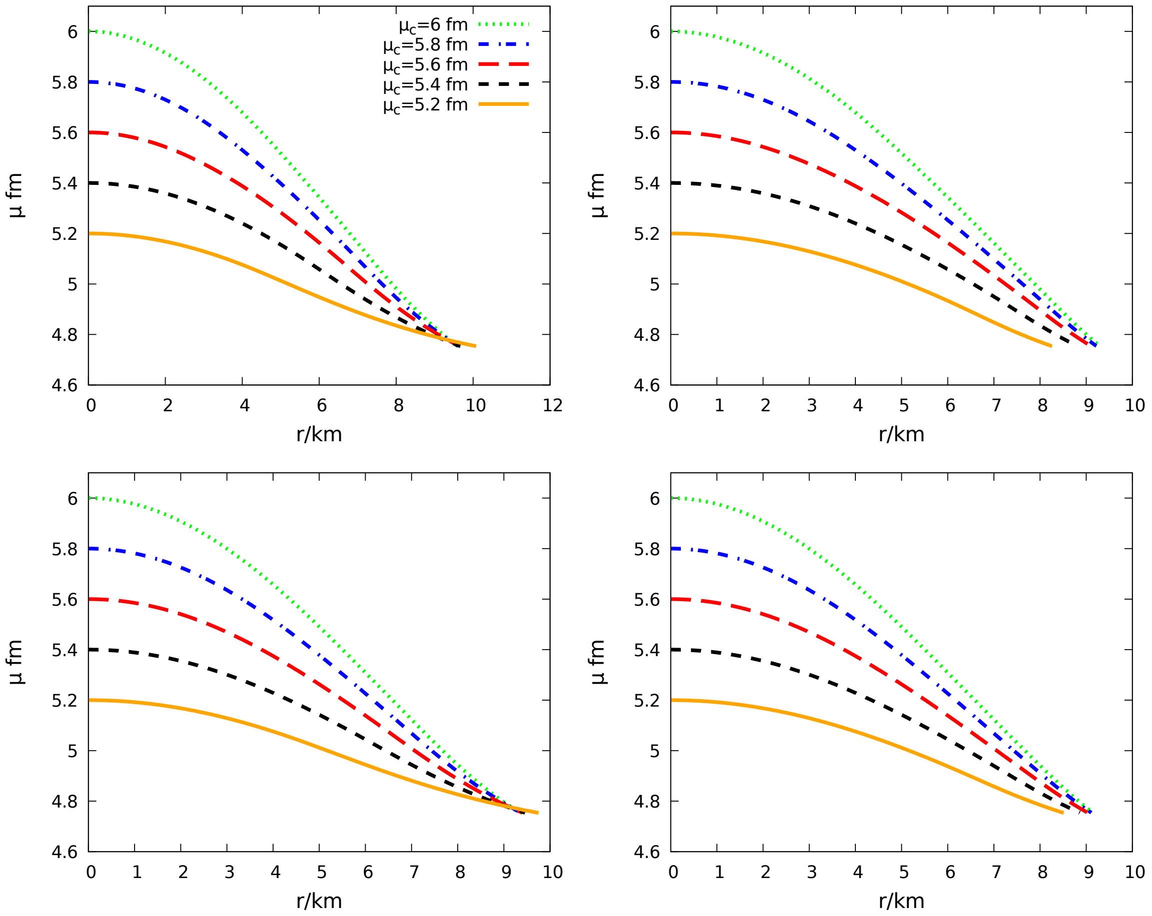

Figure 6.10: $\mu(r)$ inside the star for $\mu_t = 5\ \text{fm}^{-1}$ (left panel) and $\mu_t = 4.9\ \text{fm}^{-1}$ (right panel). The top panels are for the light ensemble and the bottom panels for the heavy ensemble.

of the bending of $M(R)$, thus an unstable sequence of stars emerges[6]. The bosonic property of the diquarks are also in line with the observed instability in the sequence of stars before the maximum. Since the main cause of stability against the gravitational collapse is the Fermi pressure of the neutrons, in the absence of this pressure we expect the collapse of the compact star. We therefore require μ_t to be such that all neutron stars lighter than the most massive ones are stable, while including as much as possible from the interacting region. Thus we choose $\mu_t = 5.07\ \text{fm}^{-1}$ for the light ensemble and $\mu_t = 5.04\ \text{fm}^{-1}$ for the heavy ensemble in the main text.

We can investigate the effect of μ_t by looking at the profile of the chemical potential inside the stars with different central chemical potentials μ_c for the three values of μ_t in Figure 6.10

Figure 6.10 shows that $\mu_t = 4.9\ \text{fm}^{-1}$ corresponds to those configurations, that by shrinking turn to the configurations with smaller mass and thus are more stable against the gravitational collapse, this is another indication of the instability of the low density sequence of $M(R)$ in the plot with $\mu_t = 4.9\ \text{fm}^{-1}$

---

[6] Contrasting to the generic behavior of $M(R)$

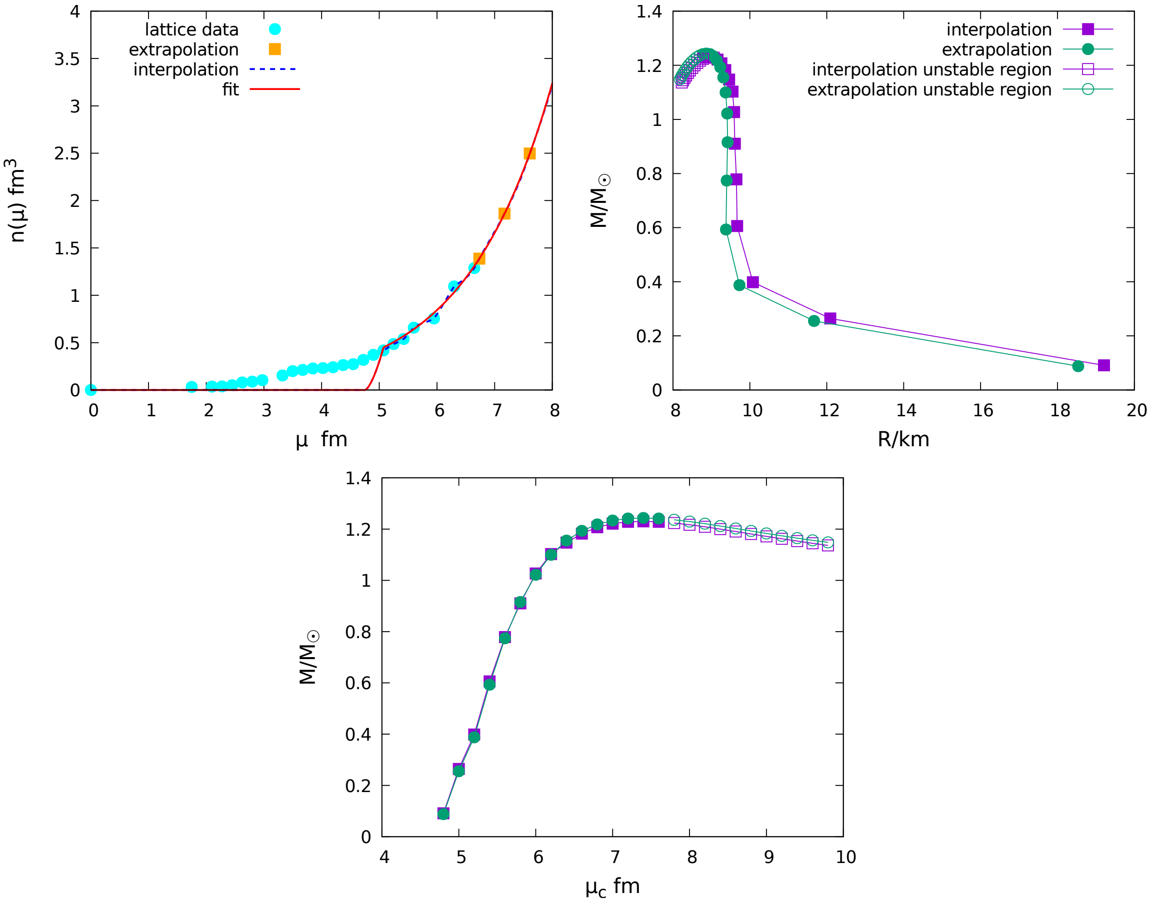

Figure 6.11: The red curve of the top-left panel shows the fit function passing through data points that differs from the interpolation indicated by the dashed blue line. The top-right panel shows the implications for the mass-radius relation. The bottom panel gives the impact on the mass-central-chemical potential relation. All results for the light ensemble. Lines connecting the points are to guide the eye.

6.5.2 Effects of the interpolation

In this context another question is how the interpolation of the lattice data, which are fluctuating and discrete, can affect the final result. To address this question, we replace the interpolation by a fit function, originally used to extract higher density points for the light ensemble. The result for $M(R)$, using this fit function as the input in the equation of state, is compared to the result of the main text in Figure 6.11. This shows that an effective description of the equation of state, using heavy fermions and modified parameters, reproduces the full dynamics rather well. Thus, the replacement of the interpolation by the fit has much less systematic impact than the choice of the transition chemical potential μ_t.

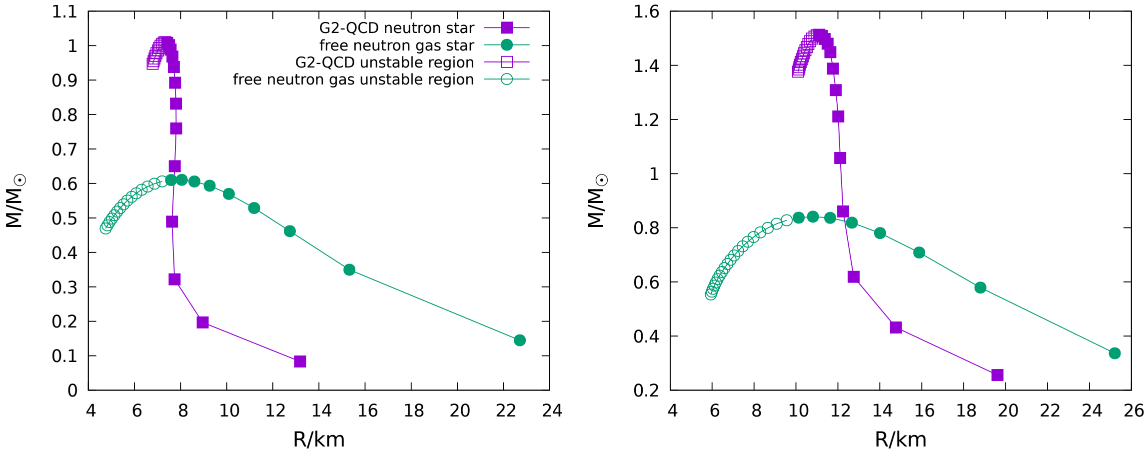

Figure 6.12: Impact on the mass-radius relation of varying the neutron mass by +8% (left panel) and −8% (right panel) for the light ensemble (purple points) and for the free gas (green points). Note that the solar mass remained unchanged.

6.5.3 Effects of the uncertainties of the mass of the neutron and additional contributions to the energy density

As we mentioned before, the scale is fixed by the physical mass of the neutron m_n, in the following way: The mass of the neutron m_l calculated on the lattice with lattice spacing a, in terms of m_n is given by

$$m_l = m_n a. \tag{6.16}$$

In the absence of the experimental data for G$_2$-QCD, and given the fact that the employed G$_2$-QCD data is produced with only one flavor, we set the mass of the G$_2$ neutron m_n equal to the QCD proton in physical units without distinguishing between the neutron and the proton. Thus the measurement of m_l on the lattice gives the lattice spacing a, and the statistical error of this measurement also propagates to a and thus to all dimensionful quantities, like the chemical potential. In order to take this effect of statistics into account, we replace m_n once by $m_n + e$ and once by $m_n - e$, where $e = 8\% m_n$ for the light and $e = 5\% m_n$ for the heavy ensemble. We may also consider the result, as a consequence of varying the equation of state by this amount. In this way if the assumptions on the equation of state also induce errors of this size, the result of varying m_n by 8% and 5% would also include the effect of this assumptions. Thus it could serve as an investigation of both systematic and statistical effects. The results of the mass-radius relation for the light ensemble are shown in Figure 6.12 The maximum mass decreases (increases) for a heavier (lighter) neutron. The latter is strongly influenced by the fact that another lattice data point in the baryon density becomes actually available when lowering the neutron mass by this amount, and thus a different low-energy fitting becomes necessary. Therefore the details of the energy density and hadron masses can have a substantial quantitative influence, but the qualitative features stay robust.

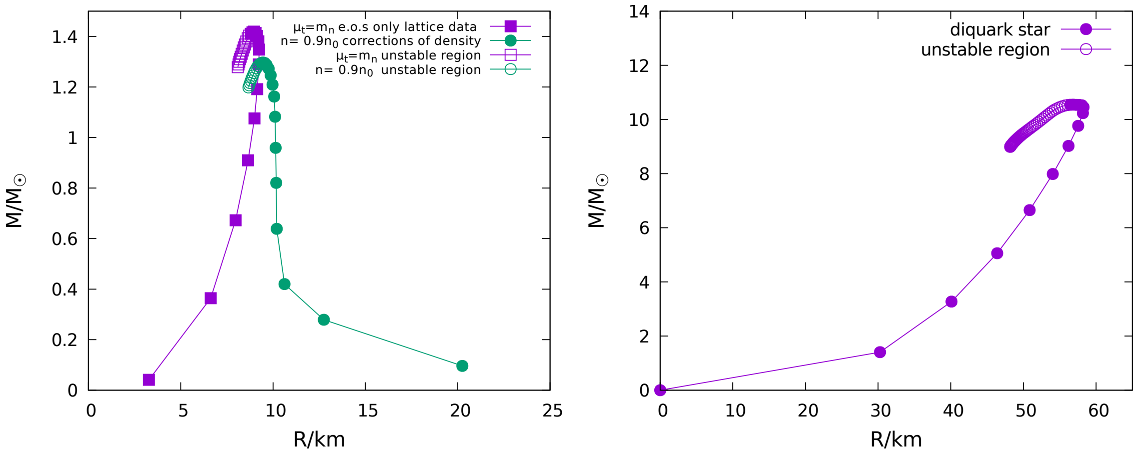

Figure 6.13: Effects of altering the assumptions about the equation of state. The left-hand plot shows the results of assuming that all of the equation of state down to the crust is created from the neutron, allowing for additional interaction contributions, and for the case that the neutrons only contribute part of the baryon density. The right-hand plot shows the result if the full equation of state would be dominated by the diquarks. Note that the normalization of the mass axis is still in units of the ordinary solar mass.

6.5.4 Effects of the assumptions about the equation of state

The most drastic assumption about the equation of state is to consider the neutrons as the only degrees of freedom contributing to the baryon number density and replace the result of the interpolation of the lattice data in low densities with the dilute Fermi gas density. We relax these assumptions in the following ways

- Assuming that other baryons than neutrons, which however do not contribute in the neutron star, also contribute in the the actual baryon density, denoted by n. This is explored by rescaling $n \to xn$, with some number x. The results for $x = 0.9$ in Figure 6.13, left panel, show no qualitative change.
- Using the result of the interpolation of the lattice data down to the neutron mass, without the free neutron gas modification. This is shown in Figure 6.13, left panel. The energy density was still constructed in the same way as before. This changed little for the maximum mass and radius, but creates a 'wrong' bending.
- Assuming the star to be made entirely out of diquarks, and thus using the baryon density down to the silver-blaze point, yields the results shown in Figure 6.13, right panel. We still assumed that the energy density is given by the diquark mass times the baryon density. This scenario can only be realized if the diquarks would form a Fermi surface[7]. It is seen that this gives the same 'wrong' bending.

The main message of this investigation is that the low density behavior is crucial for the determination of the bending of the $M(R)$ plot. It is therefore mandatory to understand on the lattice

---

[7] It may occur under a high density situation, where the quarks are bulk degrees of freedom

what is the composition and the physics in this low-density regime, and especially to determine the energy density independently.

6.6 Summary and outlook

We constructed a neutron star in G_2-QCD, in order to circumvent the infamous sign problem and thus having access to the lattice data at finite density. The only available data for our investigation is the quark baryon number density $n_q(\mu_q)$. The crucial property of the G_2 group, namely the possibility of making a color singlet object out of three quarks, lets us construct a neutron-like state in line with real QCD. Assuming that the whole baryon number density comes from the neutrons and neglecting the kinetic energy compared to the rest mass energy, we made an ansatz for the energy density. We then inserted the corresponding equation of state into the TOV equation to obtain the mass-radius relation of G_2-QCD neutron star. The resulting $M(R)$ curve is sharper around the maximum and the maximum increased by a factor of about 1.8. The results for both ensembles agree on a quantitative level, indicating that the current mass of quarks does not play a role at least for these two available ensembles. The rapid change of slope in the $M(R)$ plot coincides with a transition to the interacting region, namely for $\mu_c > \mu_t$. This is one of the main results of the present study that could relate the astronomical data to the internal structure of the stars, if it could be carried over to SU(3)-QCD. The study of the systematic effects, in the previous section, shows that the behavior of $n(\mu)$ at low densities is crucial for getting the "right" bending of $M(R)$ curve. Therefore it is crucial to know the low density composition of the G_2-QCD neutron star. The effect of the statistical error on the scale setting is important for the value of the maximum but not for the qualitative behavior. Even less important is the interpolation that could be well replaced by a fit to the data at high densities.

In the following we summarize our answers to the first question we posed, about what is necessary for an ab-initio calculation to provide a suitable result to describe a neutron star

- The most important requirement is to obtain the energy density explicitly.
- The number of measured chemical potential values should be quite dense in the region relevant for the outer crust of the neutron star.
- In the absence of data for the energy density, we need to disentangle the contributions from the neutrons and the diquarks in the baryon number density. It is necessary to determine when and how a Fermi surface forms, i. e. at which chemical potential a star starts to withstand the gravitational pressure. This requires to know the relevant degrees of freedom at this point.
- The generic requirements for lattice calculations of larger and finer lattices and better statistics hold, as always.
- In the long run, the calculation of bulk properties to verify the viability of the ideal fluid approximation would be helpful, as would be any insight on possible (color)superconducting phases [83].

Along this line, we also need to answer the following questions

- What is the relevance of bosonic hadrons? What are the various transitions between fermionic and bosonic states? How do they contribute to the number and energy densities?
- Do the properties of the particles change with density?

Note that even if QCD does not have diquarks, similar questions will arise as well. E. g. the question of the fraction of pions or excited nucleons inside a moderately dense regime will be important.

This was a first, exploratory investigation. Also the lattice data have been more exploratory than quantitative [21]. Thus, there are many avenues to improve the results presented here. A major step would be to resolve the above list. However, detailed studies show that this will be a very demanding task, even without the sign problem [84, 48], not to mention QCD itself.

Chapter 7

Conclusion

We conclude this thesis by summarizing the outcomes of our investigations to learn about the behavior of strongly interacting matter at finite density. The long-standing question of the internal structure of neutron stars can only be answered, when we have a satisfying knowledge of the equation of state of QCD at finite density and low temperature, a regime that can not be explored on the lattice.

We tried to address this problem in parallel with three different approaches:

In Chapter 4, we calculated the correlation functions of the gluons and ghosts at finite density $\mathrm{QC_2D}$. The remarkable result of this study was the almost independence of the gauge sector from the matter sector. If this results can be carried over to the finite density QCD, then this brings huge simplifications to functional methods. The latter then could make the first principle determination of the equation of state of the neutron star feasible.

In Chapter 5, we examined the validity of a certain ansatz for the Yang-Mills gluon propagator at finite temperature by fitting to the lattice data. We applied the resulting fit parameter to derive the equation of state of the Yang-Mills theory. If this fit ansatz proves to be reliable also for higher quality data, it would encourage its application and adaptation to other propagators of the fundamental degrees of freedom, so that we can get the full equation of state of QCD. The main advantage of this method would lie in its efficiency, so that instead of going through all the complications and efforts of lattice or functional methods, with an ansatz for the propagators we may be able to get a working equation of state for QCD. However, this would of course not be a first principle result.

The study of the mass radius relation of a $\mathrm{G_2}$-QCD neutron star in Chapter 6, provided us with some insight to large scale effects of a non-Abelian gauge theory. As an exploratory study, it also points out the necessary information that one needs to obtain a working equation of state from a lattice study for a $\mathrm{G_2}$-QCD neutron star. In the absence of a solution for the sign problem, this can be insightful to the case of a real neutron star.

References

[1] F. Halzen and Alan D. Martin. *QUARKS AND LEPTONS: AN INTRODUCTORY COURSE IN MODERN PARTICLE PHYSICS*. 1984.

[2] O. W. Greenberg. Color charge. *Scholarpedia*, 4(11):6933, 2009. revision #91139.

[3] David J. Gross and Frank Wilczek. Ultraviolet Behavior of Nonabelian Gauge Theories. *Phys. Rev. Lett.*, 30:1343–1346, 1973. [,271(1973)].

[4] I. B. Khriplovich. Green's functions in theories with non-abelian gauge group. *Sov. J. Nucl. Phys.*, 10:235–242, 1969. [Yad. Fiz.10,409(1969)].

[5] Gerard 't Hooft. When was asymptotic freedom discovered? or the rehabilitation of quantum field theory. *Nucl. Phys. Proc. Suppl.*, 74:413–425, 1999.

[6] Christof Gattringer and Christian B. Lang. *Quantum chromodynamics on the lattice*. Lect. Notes Phys., 2010.

[7] J. Greensite. An introduction to the confinement problem. *Lect. Notes Phys.*, 821:1, 2011.

[8] M. A. Stephanov. QCD phase diagram: An Overview. *PoS*, LAT2006:024, 2006.

[9] Axel Maas, Jan M. Pawlowski, Lorenz von Smekal, and Daniel Spielmann. The gluon propagator close to criticality. *Phys.Rev.*, D85:034037, 2012.

[10] M. Cheng, S. Ejiri, P. Hegde, F. Karsch, O. Kaczmarek, et al. Equation of State for physical quark masses. *Phys.Rev.*, D81:054504, 2010. Unquenched phase transition.

[11] J. Engels, S. Holtmann, and T. Schulze. Scaling and Goldstone effects in a QCD with two flavors of adjoint quarks. *Nucl. Phys.*, B724:357–379, 2005.

[12] F. Karsch and E. Laermann. Thermodynamics and in medium hadron properties from lattice QCD. 2003. Quenched phase transition.

[13] Christian S. Fischer, Axel Maas, and Jens A. Müller. Chiral and deconfinement transition from correlation functions: SU(2) vs. SU(3). *Eur. Phys. J.*, C68:165–181, 2010.

[14] Ernst-Michael Ilgenfritz and Axel Maas. Topological aspects of G2 Yang-Mills theory. *Phys. Rev.*, D86:114508, 2012.

[15] Julia Danzer, Christof Gattringer, and Axel Maas. Chiral symmetry and spectral properties of the Dirac operator in G2 Yang-Mills Theory. *JHEP*, 01:024, 2009.

[16] Seamus Cotter, Pietro Giudice, Simon Hands, and Jon-Ivar Skullerud. Towards the phase diagram of dense two-color matter. *Phys. Rev.*, D87(3):034507, 2013.

[17] Simon Hands, Seamus Cotter, Pietro Giudice, and Jon-Ivar Skullerud. The Phase Diagram of Two Color QCD. 2012. [J. Phys. Conf. Ser.432,012020(2013)].

[18] Larry McLerran and Robert D. Pisarski. Phases of cold, dense quarks at large N(c). *Nucl. Phys.*, A796:83–100, 2007.

[19] Simon Hands, Istvan Montvay, Susan Morrison, Manfred Oevers, Luigi Scorzato, and Jonivar Skullerud. Numerical study of dense adjoint matter in two color QCD. *Eur. Phys. J.*, C17:285–302, 2000.

[20] J.B. Kogut, Misha A. Stephanov, D. Toublan, J.J.M. Verbaarschot, and A. Zhitnitsky. QCD - like theories at finite baryon density. *Nucl.Phys.*, B582:477–513, 2000.

[21] Björn H. Wellegehausen, Axel Maas, Andreas Wipf, and Lorenz von Smekal. Hadron masses and baryonic scales in G_2-QCD at finite density. *Phys.Rev.*, D89:056007, 2014.

[22] Michael E. Peskin. The Alignment of the Vacuum in Theories of Technicolor. *Nucl. Phys.*, B175:197–233, 1980.

[23] K. Holland, P. Minkowski, M. Pepe, and U. J. Wiese. Exceptional confinement in G(2) gauge theory. *Nucl. Phys.*, B668:207–236, 2003.

[24] Gert Aarts. Introductory lectures on lattice QCD at nonzero baryon number. *J. Phys. Conf. Ser.*, 706(2):022004, 2016. finite density.

[25] H. J. Rothe. Lattice gauge theories: An Introduction. *World Sci. Lect. Notes Phys.*, 43:1–381, 1992. [World Sci. Lect. Notes Phys.82,1(2012)].

[26] C. Parrinello. Exploratory study of the three gluon vertex on the lattice. *Phys. Rev.*, D50:4247–4251, 1994.

[27] Attilio Cucchieri, Axel Maas, and Tereza Mendes. Exploratory study of three-point Green's functions in Landau-gauge Yang-Mills theory. *Phys. Rev.*, D74:014503, 2006.

[28] Axel Maas. Describing gauge bosons at zero and finite temperature. *Phys. Rep.*, 524:203, 2013.

[29] Philippe Boucaud et al. Asymptotic behavior of the ghost propagator in SU3 lattice gauge theory. *Phys. Rev.*, D72:114503, 2005. Ghost point source.

[30] L. Baulieu and D. Zwanziger. Equivalence of Stochastic Quantization and the Faddeev-Popov Ansatz. *Nucl. Phys.*, B193:163, 1981.

[31] Philippe Boucaud et al. Ghost-gluon running coupling, power corrections and the determination of $\Lambda_{\overline{\mathrm{MS}}}$. *Phys. Rev.*, D79:014508, 2009.

[32] B. Blossier, Ph. Boucaud, M. Brinet, F. De Soto, X. Du, V. Morenas, O. Pene, K. Petrov, and J. Rodriguez-Quintero. The Strong running coupling at τ and Z_0 mass scales from lattice QCD. *Phys. Rev. Lett.*, 108:262002, 2012.

[33] Florian Burger, Vittorio Lubicz, Michael Müller-Preussker, Silvano Simula, and Carsten Urbach. Quark mass and chiral condensate from the Wilson twisted mass lattice quark propagator. *Phys. Rev.*, D87(3):034514, 2013. [Phys. Rev.D87,079904(2013)] Quark propagator.

[34] Tamer Boz, Seamus Cotter, Leonard Fister, Dhagash Mehta, and Jon-Ivar Skullerud. Phase transitions and gluodynamics in 2-colour matter at high density. *Eur. Phys. J.*, A49:87, 2013.

[35] Lorenz von Smekal, Kim Maltman, and Andre Sternbeck. The strong coupling and its running to four loops in a minimal MOM scheme. *Phys. Lett.*, B681:336–342, 2009.

[36] Simon Hands, Seyong Kim, and Jon-Ivar Skullerud. Deconfinement in dense 2-color QCD. *Eur. Phys. J.*, C48:193, 2006.

[37] Simon Hands, Seyong Kim, and Jon-Ivar Skullerud. A Quarkyonic Phase in Dense Two Color Matter? *Phys. Rev.*, D81:091502, 2010.

[38] V. V. Braguta, E. M. Ilgenfritz, A. Yu. Kotov, B. Petersson, and S. A. Skinderev. Study of QCD Phase Diagram with Non-Zero Chiral Chemical Potential. *Phys. Rev.*, D93(3):034509, 2016.

[39] V. V. Braguta, E. M. Ilgenfritz, A. Yu. Kotov, A. V. Molochkov, and A. A. Nikolaev. Study of the phase diagram of dense two-color QCD within lattice simulation. *Phys. Rev.*, D94(11):114510, 2016.

[40] Lukas Holicki, Jonas Wilhelm, Dominik Smith, Björn Wellegehausen, and Lorenz von Smekal. Two-colour QCD at finite density with two flavours of staggered quarks. *PoS*, LATTICE2016:052, 2017.

[41] Dominik Nickel, Reinhard Alkofer, and Jochen Wambach. On the unlocking of color and flavor in color- superconducting quark matter. *Phys. Rev.*, D74:114015, 2006.

[42] Dominik Nickel, Jochen Wambach, and Reinhard Alkofer. Color-superconductivity in the strong-coupling regime of Landau gauge QCD. *Phys. Rev.*, D73:114028, 2006.

[43] Florian Marhauser, Dominik Nickel, Michael Buballa, and Jochen Wambach. Color-spin locking in a selfconsistent Dyson-Schwinger approach. *Phys. Rev.*, D75:054022, 2007.

[44] Dominik Nickel, Reinhard Alkofer, and Jochen Wambach. Neutrality of the color-flavor-locked phase in a Dyson- Schwinger approach. *Phys. Rev.*, D77:114010, 2008.

[45] Philipp Scior and Lorenz von Smekal. Baryonic Matter Onset in Two-Color QCD with Heavy Quarks. *Phys. Rev.*, D92(9):094504, 2015.

[46] Nils Strodthoff, Bernd-Jochen Schaefer, and Lorenz von Smekal. Quark-meson-diquark model for two-color QCD. *Phys.Rev.*, D85:074007, 2012.

[47] Ouraman Hajizadeh, Tamer Boz, Axel Maas, and Jon-Ivar Skullerud. Gluon and ghost correlation functions of 2-color QCD at finite density. *EPJ Web Conf.*, 175:07012, 2017.

[48] Björn H. Wellegehausen and Lorenz von Smekal. What we can learn from two-dimensional QCD-like theories at finite density. *PoS*, LATTICE2016:078, 2016.

[49] Axel Maas. Some more details of minimal-Landau-gauge Yang-Mills propagators. *Phys. Rev.*, D91(3):034502, 2015.

[50] Seamus Cotter, Pietro Giudice, Simon Hands, and Jon-Ivar Skullerud. Towards the phase diagram of dense two-color matter. *Phys.Rev.*, D87(3):034507, 2013.

[51] L. von Smekal. Universal Aspects of QCD-like Theories. *Nucl. Phys. Proc. Suppl.*, 228:179–220, 2012.

[52] J. Fröhlich. Phase Transitions, Goldstone Bosons and Topological Superselection Rules. *Acta Phys. Austriaca Suppl.*, 15:133–269, 1976.

[53] Herbert Neuberger. SPINLESS FIELDS ON F(4) LATTICES. *Phys. Lett.*, B199:536–540, 1987.

[54] Axel Maas. unpublished.

[55] Leonard Fister and Axel Maas. Exploratory study of the temperature dependence of magnetic vertices in SU(2) Landau gauge Yang–Mills theory. *Phys.Rev.*, D90:056008, 2014.

[56] Attilio Cucchieri, Axel Maas, and Tereza Mendes. Infrared properties of propagators in Landau-gauge pure Yang-Mills theory at finite temperature. *Phys. Rev.*, D75:076003, 2007.

[57] Attilio Cucchieri, Tereza Mendes, and Andre R. Taurines. Positivity violation for the lattice Landau gluon propagator. *Phys. Rev.*, D71:051902, 2005.

[58] Reinhard Alkofer, W. Detmold, C. S. Fischer, and P. Maris. Analytic properties of the Landau gauge gluon and quark propagators. *Phys. Rev.*, D70:014014, 2004.

[59] Lorenz von Smekal, Andreas Hauck, and Reinhard Alkofer. A solution to coupled Dyson-Schwinger equations for gluons and ghosts in Landau gauge. *Ann. Phys.*, 267:1, 1998.

[60] Attilio Cucchieri, Axel Maas, and Tereza Mendes. Three-point vertices in Landau-gauge Yang-Mills theory. *Phys. Rev.*, D77:094510, 2008.

[61] A. Cucchieri, T. Mendes, and A. Mihara. Numerical study of the ghost-gluon vertex in Landau gauge. *JHEP*, 12:012, 2004.

[62] H. J. Rothe. *Lattice gauge theories: An Introduction.* World Sci. Lect. Notes Phys., 2005.

[63] R. Aouane, F. Burger, E. M. Ilgenfritz, M. MÏler-Preussker, and A. Sternbeck. Landau gauge gluon and ghost propagators from lattice QCD with N_f=2 twisted mass fermions at finite temperature. *Phys. Rev.*, D87(11):114502, 2013.

[64] Patrick O. Bowman, Kurt Langfeld, Derek B. Leinweber, Andre Sternbeck, Lorenz von Smekal, et al. Role of center vortices in chiral symmetry breaking in SU(3) gauge theory. *Phys.Rev.*, D84:034501, 2011.

[65] Waseem Kamleh, Patrick O. Bowman, Derek B. Leinweber, Anthony G. Williams, and Jianbo Zhang. Unquenching effects in the quark and gluon propagator. *Phys. Rev.*, D76:094501, 2007.

[66] Christian S. Fischer. Infrared properties of QCD from Dyson-Schwinger equations. *J. Phys.*, G32:R253–R291, 2006.

[67] D. Binosi and J. Papavassiliou. Pinch Technique: Theory and Applications. *Phys. Rept.*, 479:1–152, 2009.

[68] Richard Williams, Christian S. Fischer, and Walter Heupel. Light mesons in QCD and unquenching effects from the 3PI effective action. *Phys. Rev.*, D93(3):034026, 2016.

[69] Anton K. Cyrol, Mario Mitter, Jan M. Pawlowski, and Nils Strodthoff. Non-perturbative quark, gluon and meson correlators of unquenched QCD. *Phys. Rev.*, D97(5):054006, 2017.

[70] Reinhard Alkofer and Lorenz von Smekal. The infrared behavior of QCD Green's functions: Confinement, dynamical symmetry breaking, and hadrons as relativistic bound states. *Phys. Rept.*, 353:281, 2001.

[71] Jens Braun. Fermion Interactions and Universal Behavior in Strongly Interacting Theories. *J.Phys.G*, G39:033001, 2012.

[72] Martina Blank, A. Krassnigg, and Axel Maas. ρ meson, Bethe-Salpeter equation, and the far infrared. *Phys. Rev.*, D83:034020, 2011.

[73] P. J. Silva, O. Oliveira, P. Bicudo, and N. Cardoso. Gluon screening mass at finite temperature from the Landau gauge gluon propagator in lattice QCD. *Phys. Rev.*, D89(7):074503, 2014.

[74] A. Cucchieri and T. Mendes. SU(2) Landau Gluon Propagator Around Criticality. *Acta Phys. Polon. Supp.*, 7(3):559, 2014.

[75] Paulo J. Silva, Orlando Oliveira, David Dudal, and Martin Roelfs. Lattice Landau gauge gluon propagator at finite temperature: non-zero Matsubara frequencies and spectral densities. *Acta Phys. Polon. Supp.*, 10:995, 2017.

[76] Anton K. Cyrol, Mario Mitter, Jan M. Pawlowski, and Nils Strodthoff. Nonperturbative finite-temperature Yang-Mills theory. *Phys. Rev.*, D97(5):054015, 2018.

[77] R. Aouane et al. Landau gauge gluon and ghost propagators at finite temperature from quenched lattice QCD. *Phys.Rev.*, D85:034501, 2012.

[78] Axel Maas and Bjorn H. Wellegehausen. G_2 gauge theories. *PoS*, LATTICE2012:080, 2012.

[79] Leonard Fister and Jan M. Pawlowski. Yang-Mills correlation functions at finite temperature. 2011.

[80] S. Tan. Energetics of a strongly correlated Fermi gas. *Annals of Physics*, 323:2952–2970, December 2008.

[81] Masakiyo Kitazawa, Takumi Iritani, Masayuki Asakawa, Tetsuo Hatsuda, and Hiroshi Suzuki. Equation of State for SU(3) Gauge Theory via the Energy-Momentum Tensor under Gradient Flow. *Phys. Rev.*, D94(11):114512, 2016. Renormalization equation state.

[82] Andrew W. Steiner, James M. Lattimer, and Edward F. Brown. The Equation of State from Observed Masses and Radii of Neutron Stars. *Astrophys. J.*, 722:33–54, 2010.

[83] Michael Buballa. NJL model analysis of quark matter at large density. *Phys.Rept.*, 407:205–376, 2005.

[84] Björn Hendrik Wellegehausen and Lorenz von Smekal. Lattice simulations of G_2-QCD at finite density. *PoS*, LATTICE2014:177, 2015.

Acknowledgements

I am grateful to my Phd advisor Axel Maas, because of his persisting support and encouragement throughout this work and because of giving me the opportunity to work in different exciting areas of the field.

I would like to thank Jan Pawlowski, who initiated the second project, presented in this thesis. I had inspiring discussions with him during my stay in Heidelberg, which Chapter 5 is partially based on.

I am thankful to Jon-Ivar Skullerud and Tamer Boz who provided us with the configurations, that have been applied in Chapter 4.

I thank all the members of the D.K. especially Christof Gattringer, Christian Lang and Reinhard Alkofer that I learned from their publications and lectures.

I would like to thank my colleauges at the Univesity of Graz, Hans-Peter Schadler, Romain Contant and especially Thomas Kloiber who helped me out of some technical difficulties and also kindly read through this thesis.

I would like to thank all the secretaries of the Physics institute, especially Fanny Maetz and Claudia Spidla.

Finally, I dedicate this thesis to my parents, Gholamhossein Hajizadeh and Afzal Makki, who were my first teachers and friends.